Influence of Geometrical irregularities on the in-plane behaviour of a masonry wall façade in macro-element based and analytical mechanism based analyses

ARCADIS | Design & Consultancy for natural and built assets

TUDelft

Influence of Geometrical irregularities on the in-plane behaviour of a masonry wall façade in macro-element based and analytical mechanism based analyses

by

Anass el Kouri

to obtain the degree of Master of Science

at the Delft University of Technology

Thesis committee:	Prof.dr.ir. J.G. Rots
	Dr. F. Messali
	Ir. S. Pasterkamp
	Martijn Bettonvil
	Gerard van Engelen

An electronic version of this thesis is available at http://repository.tudelft.nl.

TUDelft

Summary

Since 1963, the extraction of gas is going on in Groningen. This has caused (human) induced earthquakes in recent decades. The first induced earthquake took place in 1991 and in recent years induced seismicity has considerably increased in this region. These incidents are a significant danger for the built environment, because the building stock is mainly composed of unreinforced masonry structures, vulnerable for seismic activity due to the use of slender walls, weak wall-floor connections and cavity walls.

The seismic assessment of unreinforced masonry structures in Groningen is still ongoing. The assessment is vital to determine whether a building must be strengthened or not. Different assessment approaches have been followed in recent years. First, the Non Linear Time-History analyses (NLTHA) were initially the only approach used for the seismic assessment. They are still overall the most accurate type of assessment, but they are also the most time-consuming one. Nowadays, NLPO analyses are more frequently used. This assessment procedure presents some limitations of application and may be less accurate for complex structures but it requires less computational time. The NLPO analyses can be performed by means of different tools, such as analyses based on the finite element method (FEM), equivalent frame (EF) or macro-element based analyses and, eventually, also analytical mechanism based analyses. The SLaMA method belongs to this last category: this method is an analytical approach already tested and validated in New Zealand for RC structures.

This research aims to answer the following research question:

•   How is the in-plane behaviour of single-storey URM wall facades affected in simplified calculation methods compared to FEM when geometrical irregularities are present?

The walls have been modelled in 2D with three different methods: FEM, EF and SLaMA. Material properties and modelling assumptions were maintained as consistent as possible within the three different methods. For researching the influence of the geometrical irregularities on the accuracy of EF and SLaMA when compared to FEM, the variation of geometrical irregularities, each quantified by an index value, have been studied. The influence of these indices on the accuracy of the calculation methods has been researched with a sensitivity analysis.

The objective has been pursued by looking into single-floor URM façades, and the conclusions of this research can be applied to this typology of walls in Groningen made of solid clay brick masonry (pre 1945). The study focuses specifically on the base shear capacity of the walls.

The differences observed when comparing the in-plane behaviour of a wall analysed with 3MURI and DIANA are not significantly affected by the presence of geometrical irregularities. The ratio between the base shear capacity computed with the two approaches and the predicted failure mechanisms remains consistent for all geometrical irregularities defined in this report.

Similarly, the differences observed when comparing the in-plane behaviour of a wall analysed with SLaMA and DIANA are not largely affected by the presence of geometrical irregularities, since the base shear computed according to SLaMA is consistently lower than that obtained with DIANA. However, the base shear capacity obtained with SLaMA showed large variations between 0.34 and 0.75 with respect to DIANA when implementing geometrical irregularities. The largest variation is obtained when more than a single pier is considered, due to the inability of SLaMA to define the re-distribution of the vertical axial forces in the piers, nor correct boundary conditions at the top of the piers since the constraining action of the spandrel appear underestimate. This affected also the prediction of the failure modes, which differed for the two methods. However, in most of cases flexural failure mode was obtained, and the study should be extended to consider also geometries and loading conditions that cause also the shear failure of the walls.

Acknowledgements

Contents

List of figures

List of tables

1 Introduction

1.1 Context

Since 1963, the extraction of gas is going on in Groningen. This has caused (human) induced earthquakes in recent decades. The first induced earthquake took place in 1991 and in recent years induced seismicity has considerably increased in this region. These incidents are a significant danger for the built environment, because the buildings are mainly unreinforced masonry structures. These structures are vulnerable for seismic activity because of their slender walls, weak wall-floor connections and use of cavity walls.

The seismic assessment of unreinforced masonry structures in Groningen is still ongoing. The assessment is vital in determining the seismic strengthening for a building. Different assessment approaches have been done in recent years. First, the NLTHA was the main approach for the seismic assessment. This is still the most accurate assessment, but also the most time-consuming one. Nowadays, the NLPO analysis is more frequently used. This assessment may be less accurate for complex structures but has less computational time. Recently, a new seismic assessment method has been developed, namely the SLaMA method. This method is an analytical approach for the seismic assessment of a full structure. It has already been tested in New Zealand and validated for RC structures with NLPO.

In this research, the main subject is the in-plane behaviour of unreinforced masonry when geometrical irregularities are present. For example: asymmetry, opening percentages, pier geometry and spandrel geometry. Different calculation methods exist for the in-plane behaviour of an URM wall. However, it is still unclear how these methods perform when the irregularities increase.

1.2 Aim of research

The aim of the research is to analyse whether the calculation methods for the in-plane behaviour now are error-proof when geometrical irregularities in the façade of an URM wall are present.

1.3 Research questions

The research question sounds:

- *How do geometrical irregularities affect the assessment of the in-plane behaviour of single-storey URM wall facades performed with a mechanism based and a frame based analysis when compared to FEM?*

The sub questions hereby are:

- What are the results of an analysis in SLaMA of a 2D URM wall façade, in terms of force and displacement?
- What are the results of an analysis in FEM of a 2D URM wall façade, in terms of force and displacement?
- What are the results of an analysis in EFM of a 2D URM wall façade, in terms of force and displacement?
- Are the results of analyses performed to different calculation methods (FEM, EFM, SLaMA) consistent with each other when increasing geometrical irregularities?
- What is the difference in results between the different methods?
- How conservative are the simplified methods?

1.4 Research method

First the calculation methods should be understood, so as a first step the seismic capacity of a masonry wall free of openings or geometrical irregularities will be calculated for all three methods. This will be compared with each other and should have in first instance the same result for all three methods. After this first comparison has been done, irregularities in the geometry of the models will be applied and the same procedure follows as the first example. After each comparison, the model will

be modified and become more complex. The more comparisons that are done in which different aspect will be varied, the better the conclusion will be.

2 Literature study

In this section the important literature concerning this research has been described. Analytical methods have been considered and further explained. First the SLaMA method has been summarised. Then the equivalent frame method is described. In the end, the problem of geometrical irregularities is clarified. It should be noted that (parts of) this literature study has been done in cooperation with Nidal Ennali with the consent of our committee members.

2.1 SLaMA Method

SLaMA method is an analytical approach to make a seismic assessment of buildings. This method is firstly initiated in New Zealand, where they applied this method for several building. The SLaMA method is normally applied to give a first estimation of the global capacity of a building subjected to a seismic load. Mostly this first estimation determines what kind of assessment is necessary to follow the SLaMA assessment. The assessment method that follows from this first estimation could be the NLPO or NLTHA. Both these methods are considered as reliable and validated methods for unreinforced masonry buildings (URM buildings).

Total overview SLaMA method

This part consists of a short summary of the SLaMA as described in **NZSEE C8** (NZSEE, 2017) and the **NPR9998** (NEN, 2018) specified to unreinforced masonry.

Step 1: Assess the structural configuration and load paths to identify key structural elements, potential structural weaknesses (SWs) and severe structural weaknesses (SSWs). (NZSEE, 2017)

Unreinforced masonry buildings consist of boundary walls, walls and diaphragm. Diaphragm can be a ceiling, floor or foundation. Depending on the material this diaphragm could differ in stiffness.

The wall elements within an URM building could be divided in wall element with penetration and wall element without penetrations. For the assessment also the orientation of the wall is important. Walls can be oriented parallel to the plane of loading or perpendicular.

These elements within an URM building need to be analysed by consulting the plans/blueprint and details. When analysing special notice must be given in the structural configuration, load paths, potential structural weaknesses and severe structural weakness. Analysing these structural elements is part of the first step of the SLaMA method.

Step 2: Assess the capacity of the diaphragm/ wall connection to determine if the diaphragm If capable to transfer lateral load to the walls. (NZSEE, 2017)

In the second step is it necessary to analyse the detail drawings of the connections between the diaphragm and walls. The capacity of the connection between the diaphragm and the wall is dependent on the decisive failure mode.

Step 3: Determine the out-of-plane response and the out-of-plane capacity using the NLKA-method.

The next phase of the SLaMA method is the determination of the out of plane response of a wall element loaded with a face load. Both the NZSEE (NZSEE, 2017) and the NPR9998 (NEN, 2018) use the same method for determining these out of plane responses. This method is based on a NLKA-approach, a nonlinear kinematic analysis. This method will lead to a conservative value for the resistance of this wall. The method is in general applicable to masonry walls oriented in a normal manner. Walls that are oriented in a complex geometry needs to be analysed with a different method.

Step 4: Determine the in-plane response and the in-plane resistance to the possible failure modes.

Before analysing behaviour of the wall loaded in plane, two different wall types need to be described. First-of-all, there are walls with penetrations. These walls consist of the pier elements and spandrel elements. The pier elements are the wall parts between the penetrations. And the spandrels are the wall part above this penetration. The other wall type is the wall without any penetration.

The in-plane capacity of the URM walls or piers could be determined based on the governing failure mechanism.

The following failure mechanisms are considered when analysing the in-plane capacity of the URM walls or pier elements. The derivation of the formulas will be given in the next section of this chapter.

- Diagonal tensile
- In-plane rocking / Toe crushing
- Bed-joint sliding
- Slip plane sliding
- URM spandrel failure

Step 5: Determine probable inelastic behaviour of elements by comparing probable member capacities and evaluating the hierarchy of strength.

In this step of the SLaMA method it is necessary to compare the strengths of the different components in a URM -wall. The inelastic behaviour of every component needs to be analysed. And finally, the hierarchy of strength could be determined. The following components must be considered in this step:

- Wall loaded out of plane
- Wall without penetrations loaded in-plane
- Spandrels
- Piers
- Foundation
- Diaphragm

Step 6: Assess the sub-system inelastic mechanisms by extending local to global behaviour. (NZSEE, 2017)

The global capacity is the strength and deformation capacity of a total building. In the assessment of the global capacity only the primary structure is considered. The primary structure consists of the diaphragm and the walls loaded in-plane. In case of the cantilever wall system, the walls loaded out of plane should also be considered in this assessment.

The diaphragms distribute the lateral force to the wall loaded in plane. This diaphragm could be flexible or rigid. The flexible diaphragm can be modelled in a 3D analysis or 2D analysis. The rigid diaphragm could result in an eccentricity due to the different rigidities of the walls. This results in torsion, and thereby an extra lateral force due to shear stresses.

Step 7: Form a view of potential governing mechanism and calculate probable base shear and global displacement capacity. (NZSEE, 2017)

The global displacement capacity and the probable base shear could be calculated based on the stiffness of the diaphragm and the shear/deformation capacity of the governing structural element

(spandrel, piers, foundation, etc.). The governing structural element is the element which has the lowest capacity due to the occurrence of a plausible failure mechanism.

Step 8: Determine equivalent SDOF system, seismic demand and %NBS. (NZSEE, 2017)

In this step the structure needs to be schematised as a SDOF system. The steps to determine the effective mass and the effective height are described in more detail in the next section. Based on the SDOF model, the %NBS could be determined. Also, the procedure to determine the seismic demand is described in the NZSEE C8 ((NZSEE, 2017).

In plane behaviour masonry

This study focuses mainly on the in-plane behaviour of masonry. Therefore, it is interesting to study the derivation of the shear capacities for each failure mechanism.

Rocking failure

Rocking failure is a mechanism that occurs due to tilting of the pier. The failure mechanism is a stable mechanism which means that it doesn't result in an immediate collapse of the piers. Rocking of the pier will take place until the toe crushes due to compression stresses. The shear capacity is derived based on the assumption that the compressive stress at the base of a pier, that undergoes rocking, has a parabolic distribution. Subsequently this parabolic distribution is assumed to be rectangular with a correction factor of 0.85. There will be a difference in the assumed compression energy and actual compressive energy. Another assumption in this derivation is that the bed joint tensile strength is neglected. The figure below shows the assumed mechanical model which has been used by Calvi and Magenes (GUIDO MAGENES, 1997) to derive this shear capacity. This formula is adopted by both the NPR9998 and the NZSEE-C8.
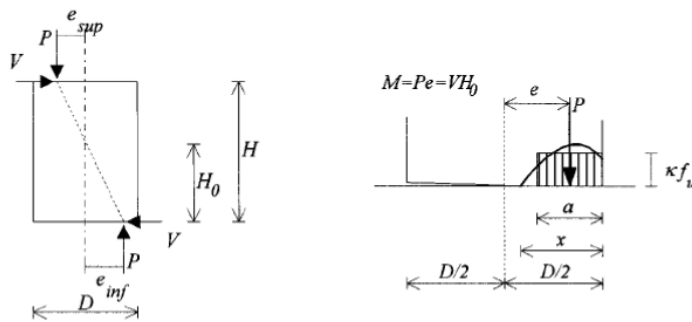
Figure 1: Assumed mechanical model rocking failure (GUIDO MAGENES, 1997)

$P = \ Normal\ force\ in\ N$

$f_u = Compressive\ strength\ in\ N/m^2$

$t = \ thickness\ of\ the\ pier\ in\ m$

$L = \ Length\ of\ the\ pier\ in\ m$

$\sigma_y = average\ compressive\ stress\ at\ the\ top\ of\ the\ pier$

$f_{ma;m} = average\ compressive\ strength\ of\ the\ masonry$

$h_0 = Effective\ heigth\ of\ the\ pier\ depended\ on\ the\ boundary\ conditions\ of\ the\ piers.$

$$e_{slama} = \frac{L}{2} - a = \frac{L}{2} - \frac{P}{0.85 \cdot f_u \cdot t}$$

$$V_r = P \cdot \frac{L}{2 \cdot h_0} \cdot (1 - 1.15 \cdot \frac{\sigma_y}{f_{ma;m}})$$

Beside the rocking failure mechanism there is also shear failure. There are two different form of shear failure, namely diagonal cracking and sliding. The shear failure considering diagonal cracking is a complex failure mechanism to describe in one formula. Calvi and Magenes (GUIDO MAGENES, 1997) derived in his paper an expression for this type of failure mechanism, which has been adopted by the NPR9998 and the NZSEE C8.

There starting point for this derivation is the following Mohr-Coulomb criterion:

$$\tau_u = c + \mu \cdot \sigma_v$$

$\tau_u = ultimate \ shear \ failure$

$c = cohesion$

$\mu = friction \ coeficient$

$\sigma_v = the \ average \ axial \ stress \ due \ to \ the \ axial \ force \ on \ the \ pier$

$P = axial \ force \ at \ the \ top \ of \ the \ pier$

In this case diagonal cracking is associated failure of mortar bed and head joint. Diagonal cracking could also be caused by cracking trough the bricks if the mortar is stronger than the bricks.

The shear capacity of a pier failing due to diagonal cracking is determined based on the assumption that the shear stress distribution in uniform which results in the following formula.

$$V_d = \tau_u \cdot D \cdot t = (c + \mu \cdot \sigma_v) \cdot D \cdot t = D \cdot t \cdot \left(c + \mu \cdot \frac{P}{D \cdot t}\right)$$

The expression above describes the shear capacity under the assumptions that there is no cracking developing due to flexure. This assumption could result in the overestimation of the shear capacity. The effect is included by calculating the uncracked length at both ends of the pier. The tensile bed joint strength is neglected in derivation for the uncracked length. Furthermore, the compressive stress distribution is assumed to be linear or constant. With these main assumptions the following the formulae has been derived. This formula is in the same manner adopted by the NPR 9998 and the NZSEE C8.

$$D' = 3 \cdot \left(\frac{1}{2} - \frac{V}{P} \cdot \frac{H_0}{D}\right) \cdot D$$

$$V_d = D \cdot t \cdot \frac{1.5 \cdot c + \mu \cdot p}{1 + 3 \cdot \frac{c \cdot \alpha_v}{p}}$$

$D' = uncracked \ section \ length$

$p = compressive \ stress \ at \ the \ top \ of \ the \ pier$

$$\alpha_v = shear \ ratio = \frac{H_0}{D}$$

The other approach to determine the diagonal cracking due to the exceeding of the conventional tensile strength of the masonry by the principal stresses in the pier. This failure mechanism is one of the most undesirable failure mechanisms, because it results in a rapid strength degradation (brittle failure mode). Calvi and Magenes (GUIDO MAGENES, 1997) formulated a formula describing the shear capacity in the case that this failure mode is decisive. The formula is based on tests whereby a horizontal load is applied on an unreinforced masonry pier under double clamped condition (MIHA TOMAZEVIC, 1997).

$$V_d = \frac{f_{tu} \cdot D \cdot t}{b} \cdot \sqrt{1 + \frac{p}{f_{tu}}}$$

$f_{tu} = conventional\ tensile\ strength$

$D = length\ of\ the\ pier$

$p = compressive\ stress\ due\ to\ the\ axial\ force$

$b = parameter\ depended\ on\ the\ aspect\ ratio$

It must be noted that the NPR9998 states that for most regular Dutch masonry this failure mode could be neglected. In the 2D and 3D assessment phase, this failure mode will be considered and from there it could be determined if this statement is valid.

The NPR9998 (NEN, 2018) considers shear capacity in the case of the sliding failure mode with the first formula. Another failure mode that must be considered is the case that the combination of compression stresses and shear stresses result in splitting of the bricks while the friction is large enough to avoid sliding. The NPR9998 formulates this limit state in the following manner.

$V_r \leq 0.1 \cdot f_b \cdot D' \cdot t_p$

$f_b = compressive\ strength\ of\ the\ brick$

$D' = uncracked\ section\ length\ , lenght\ of\ the\ compression\ zone$

$t_p = thickness\ of\ the\ pier$

Displacement capacity

The drift capacity of the rocking failure mode could be determined by the following empirical formula which formulated in the paper of Messali (F. Messali, 2017). This formula is derived based on the data obtained from laboratory tests of clay and calcium silicate urm walls. The test have been made by the TUDelft and the EUROCENTRE commissioned by the NAM(Nederlandse aardolie maatschappij). This research on the drift limit shows that the displacement capacity of URM pier is mainly depended on the axial load ratio and the aspect ratio. Other properties of the urm pier like, boundary condition, wall height, thickness and Head-and bed-joint typologies have not a sifnificant influence on the displacement capacity (F. Messali, 2017).

$$\theta_{R,NC,f} = 0.0135 \cdot (1 - 2.6 \cdot \frac{\sigma_y}{f_{ma;m}}) \cdot (\frac{h_{ref}}{hp}) \cdot \sqrt{\frac{h_p}{l_p}}$$

$h_p = heigth\ of\ the\ pier$

$l_p = Length\ of\ the\ pier$

$\sigma_y = axial\ stress\ at\ the\ top\ of\ the\ pier$

$f_{ma;m} = mean\ compressive\ strength$

Bed joint sliding or diagonal stair stepped sliding are stable failure modes. Which means that when the initial cracking starts the pier would not result in an immediate collapse. Because of this ductile failure mode, the pier will have a considerable displacement capacity even when initial cracks start to develop. Based on several researches' om the displacement capacity of a pier undergoing sliding, the following force-drift diagram has been recommended to use for piers undergoing sliding failure. The force-drift diaphragm is adopted by both the NPR9998 (NEN, 2018) and the NZSEE C8 (NZSEE, 2017).
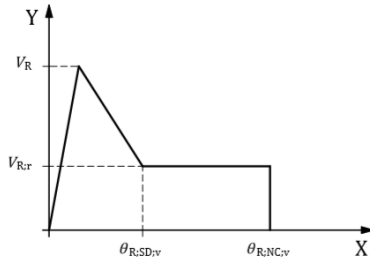
Figure 2: Force-drift diagram according to the NPR9998

The maximum shear capacity could be calculated with the sliding formula of Calvi and Magenes (GUIDO MAGENES, 1997). To determine the residual shear capacity, the cohesion of the masonry could be neglected.

$$V_R = D \cdot t \cdot \frac{1.5 \cdot c + \mu \cdot p}{1 + 3 \cdot \frac{c \cdot \alpha_v}{p}}$$

$V_{R,r} = D \cdot t \cdot \mu \cdot p$

The following drift limits are suggested by the NZSEE C8 and the NPR9998.

$\theta_{R;SD;v} = 0.003$

$\theta_{R;ND;v} = 0.0075$

Spandrel shear capacity

For the spandrel two different failure types could be distinguished, namely shear failure and flexural failure. This part will describe only the capacity formulas of rectangular spandrels without the effect of the lintels. That are the only formulas applicable to the case studies that will be analyzed in the next chapter.

Shear failure

Shear capacity of the rectangular spandrels is formulated based on the assumption that the spandrel consists of elastic homogeneous material with a parabolic shear stress distribution along the height of the spandrel. The shear capacity could be found by the integrating the shear stress distribution along the height of the spandrel. This results in the following formulation for head-and bed joint sliding occurring in a spandrel (Beyer, 2011):

$$V_{cr,s} = \frac{2}{3} \cdot \tau_{max} \cdot h_{sp} \cdot t_{sp}$$

$$\tau_{max} = c + \mu \cdot p_{sp}$$

$$V_{cr,s} = \frac{2}{3} \cdot (c + \mu \cdot p_{sp}) \cdot h_{sp} \cdot t_{sp}$$

$\tau_{max} = maximum\ shear\ stress\ along\ the\ height\ of\ the\ spandrel\ in\ N/mm^2$

$\mu = friction\ of\ the\ masonry$

$p_{sp} = axial\ stress\ at\ the\ spandrels$

$c = cohesion\ of\ the\ masonry\ in\ N/mm^2$

Shear failure of the spandrels can occur in two manners. One way is that the shear cracks develop through bed and head joint. The other shear failure type is that the cracks develop through the bricks instead of the bed and head joints. The last failure type occurs for masonry that consists of strong mortar and the weak bricks. The shear capacity corresponding to the last failure type could be determined based on the following formula NZSEE C8 and NPR9998:

$$V_s = f_{dt} \cdot \beta_{sp} \cdot \sqrt{1 + \frac{p_{sp}}{f_{dt}}} \cdot h_{sp} \cdot t_{sp}$$

$$f_{dt} = 0.5 \cdot c + f_a \cdot \mu$$

$$\begin{cases} \dfrac{l_{sp}}{h_{sp}} > 1.5, & \beta_{sp} = 0.67 \\ \dfrac{l_{sp}}{h_{sp}} < 1.0, & \beta_{sp} = 1.0 \end{cases}$$

$l_{sp} = Length\ of\ the\ spandrel$

$h_{sp} = heigth\ of\ the\ spandrel$

$f_{dt} = Diagonal\ tensile\ strength\ of\ masonry\ in\ N/mm^2$

The residual shear capacity when shear failure occurs can be neglected if the lintels are not considered. The NPR9998 and the NZSEE, show the effect of the lintels of the residual shear capacity.

Flexural failure

The shear capacity in the case that flexure failure behavior is governing, is depended on the tensile strength of the head joints, and interlocking of the bed joints. The tensile strength of the head joint could be approximated by the following expression (Beyer, 2011):

$$f_{hj} = \frac{c}{2 \cdot \mu}$$

$c = cohesion\ in\ N/mm^2$

$\mu = friction\ coefficient$

The equivalent tensile strength resulting from the interlocking of the bed joints has been formulated under the assumption that the shear stress along the bed joint is uniform distributed. The stress perpendicular at the bed joints and the cohesion of the bed joint contribute to the equivalent tensile strength of the spandrel. The equivalent tensile strength is the sum of the tensile strength of head joint and the interlocking of the bed joint.

$$f_t = f_{hj} + f_{bj}$$

$$f_t = 1.3 \cdot (c + 0.5 \cdot \mu \cdot \sigma_v) + \frac{c}{2 \cdot \mu}$$

Based on the assumption that the stress is linear distributed along the height of the spandrel, the bending moment and the shear capacity could be calculated with the following simple formulas.

$$M_{fl} = (f_t + p_{sp}) \cdot \frac{h_{sp}^2 \cdot b_{sp}}{6}$$

$$V_{fl} = (f_t + p_{sp}) \cdot \frac{h_{sp}^2 \cdot b_{sp}}{3 \cdot l_{sp}}$$

The residual flexure shear capacity is determined based on the developed diagonal compressive strut. Therefore, the compressive strength in horizontal direction would be the normative in the determination of the residual shear capacity. The tensile strength of the head joint and the cohesion of the bed joint will tend to go to zero after the peak capacity is reached. Therefore, these properties could be neglected in the derivation of the residual shear capacity. After cracking the compression zone height will decrease until h_c. The compressive strength in the horizontal direction f_{hm} is 50% of the compressive strength of masonry (Beyer, 2011).

$$h_c = \frac{P_{sp}}{0.85 \cdot f_{hm} \cdot b_{sp}}$$

Based on this compression zone, the residual shear capacity could be determined with the following expression NPR9998.

$$V_{fl,r} = \frac{p_{sp} \cdot h_{sp}^2 \cdot b_{sp}}{l_{sp}} \cdot (1 - \frac{p_{sp}}{0.85 \cdot f_{hm}})$$

$f_{hm} = Compressive\ strength\ in\ the\ horizontal\ direction$

$p_{sp} = Axial\ stresses\ due\ to\ restraint\ elongation\ of\ the\ sprandrel\ or\ due\ to\ prestressing$

$l_{sp} = Length\ of\ the\ spandrel$

$h_{sp} = heigth\ of\ the\ spandrel$

$b_{sp} = thickness\ of\ the\ spandrel$

Axial stresses on the spandrel would be generated due to the restraint of the elongation when the spandrel is deformed. The stresses need to be considered when calculating the residual shear

capacity due to flexural failure. These stresses could be calculated with the following formula which is stated in the NPR9998.

$$p_{sp} = (1 + \beta_{sp}) \cdot f_{dt} \cdot \frac{l_{sp}}{\sqrt{l_{sp}^2 + h_{sp}^2}}$$

$f_{dt} = Diagonal\ tension\ strength\ of\ the\ masonry$

Important point to note is that all the formulas concerning the spandrel shear capacity are excluding the effect of the lintels. Because the effect of the lintels will be out of the scope of this study.

The following force drift diagram for the spandrel is recommended by both the NSCEE C8 and NPR9998. This diagram is based on a lot of research concerning the displacement capacity of spandrels.
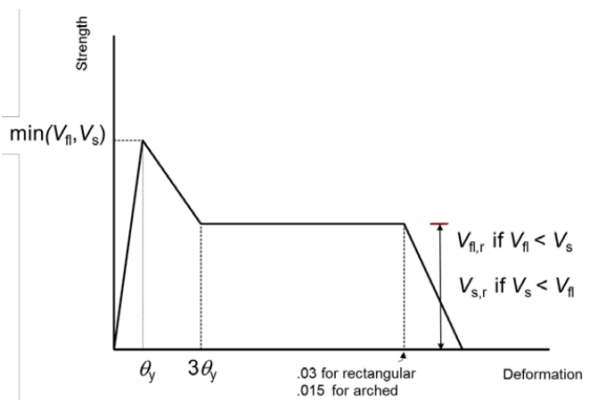
Figure 3: NZSEE C8

2.2   Equivalent frame method

The equivalent frame method (EFM) is a method which can model an URM structure with an equivalent framework. By doing so, the number of degrees of freedom can be narrowed in comparison to FEM. This reduces the computational time significantly. The EFM divides a wall as an idealised frame where deformable elements are connected with rigid nodes. Deformable elements are elements in which the nonlinear response of the wall is concentrated and rigid nodes are elements of the wall not subjected to damage. The deformable elements can be divided in piers and spandrels. Piers are the primary vertical resistant elements, which carry the vertical and lateral loads. Spandrels are secondary elements which couple the response of adjacent piers concerning lateral loads. The spandrels also have a significant influence on the boundary conditions of the piers which has a large influence on the wall lateral capacity. Figure 1 shows an example of the idealisation of the method.
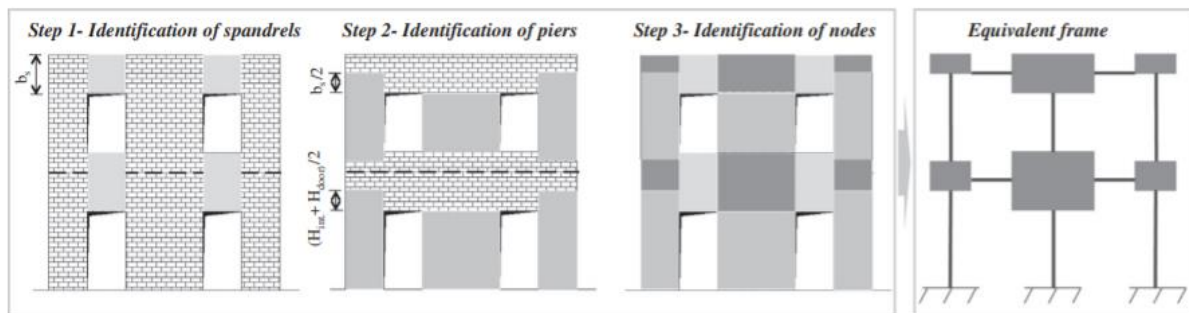
Figure 4: Equivalent Frame idealisation (Lagomarsino, Penna, Galasco, & Cattari, 2013)

Defining the geometry of the main structural elements is the first step of the equivalent frame idealisation. Spandrel geometry is defined based on the vertical alignment and the superimposition of the openings. In case of full alignment, the length and height are equal to the vertical distance between openings and the width of the openings. Pier geometry is defined by the height of the adjacent openings. If these are perfectly aligned, the height of the pier is equal to the adjacent openings. If not, the height of the pier is equal to the average of the inter-storey height and the height of the adjacent opening. Step 3 is the identification of the rigid nodes. This can easily be defined from the defined geometries of the piers and spandrels.

Once the masonry wall is idealised by an equivalent frame model, the prediction of its behaviour depends on the response of the individual structural elements. The response of the individual elements depend on their properties. The properties of these elements are based on the governing failure mechanisms (Knox, 2012).

Different assessment tools make use of the EFM. One frequently used software is the program 3MURI. However, the EFM gives larger errors for larger irregularities in the façade's geometry (Siano, et al., 2017).

2.2.1 Material model: 3MURI Macro-element Model

The structural elements of a masonry wall are divided in piers and spandrels according to the equivalent frame method described in chapter 2.2. These elements are represented in 3MURI 12.2.1 by use of macro-elements as presented in the figure below. This means that the masonry is represented as a composite material with anisotropic properties spread over the element.
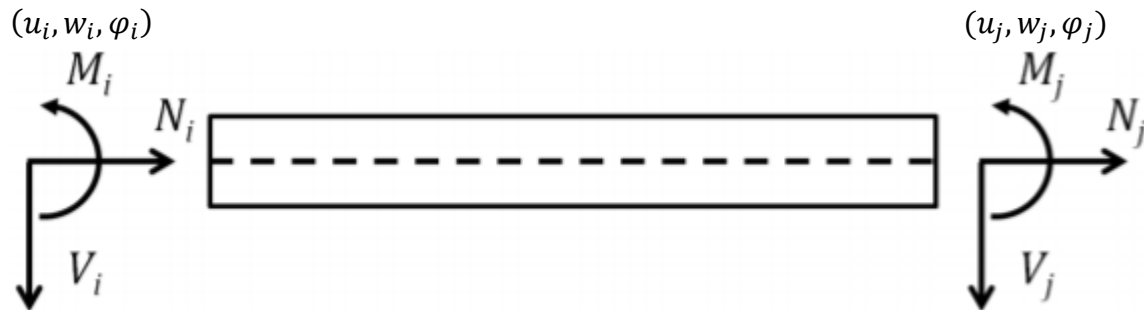
Figure 5: Macro-element in 3MURI (3MURI, 2019)

Loads are only applied on the nodes as can be seen in the figure above. The element force-displacement curve exhibits bilinear behaviour. The element deforms initially with the initial stiffness of the material until the shear capacity is reached. Then the stiffness is reduced to zero and the shear force stays constant until the drift limit is reached. The drift limit is predefined in 3MURI. The degrees of freedom can be determined with the stiffness matrix below as described by (Lagomarsino, Penna, Galasco, & Cattari, 2013):

$$
\begin{Bmatrix} V_i \\ N_i \\ M_i \\ V_j \\ N_j \\ M_j \end{Bmatrix} =
\begin{bmatrix}
\frac{12EJ\eta}{h^3(1+\psi)} & 0 & -\frac{6EJ\eta}{h^2(1+\psi)} & -\frac{12EJ\eta}{h^3(1+\psi)} & 0 & -\frac{6EJ\eta}{h^2(1+\psi)} \\
0 & \frac{EA}{h} & 0 & 0 & -\frac{EA}{h} & 0 \\
-\frac{6EJ\eta}{h^2(1+\psi)} & 0 & \frac{EJ\eta(4+\psi)}{h(1+\psi)} & \frac{6EJ\eta}{h^2(1+\psi)} & 0 & \frac{EJ\eta(2-\psi)}{h(1+\psi)} \\
-\frac{12EJ\eta}{h^3(1+\psi)} & 0 & \frac{6EJ\eta}{h^2(1+\psi)} & \frac{12EJ\eta}{h^3(1+\psi)} & 0 & \frac{6EJ\eta}{h^2(1+\psi)} \\
0 & -\frac{EA}{h} & 0 & 0 & \frac{EA}{h} & 0 \\
-\frac{6EJ\eta}{h^2(1+\psi)} & 0 & \frac{EJ\eta(2-\psi)}{h(1+\psi)} & \frac{6EJ\eta}{h^2(1+\psi)} & 0 & \frac{EJ\eta(4+\psi)}{h(1+\psi)}
\end{bmatrix}
\begin{Bmatrix} u_i \\ w_i \\ \phi_i \\ u_j \\ w_j \\ \phi_j \end{Bmatrix}
$$

Figure 6: Stiffness Matrix macro-element

Where:

$$\psi = 1.2 \frac{Eb^2}{Gh^2}$$

The failure of the macro-elements in 3MURI can be described by three failure mechanisms: rocking, diagonal shear and shear sliding failure. The applied equations in 3MURI for assessment of the shear capacity are similar to the applied equation used in the SLaMA method in chapter… What should be noted is, that in 3MURI there is an option where the user has to choose which of the shear failure mechanism is prone to occur, diagonal shear failure based on the equation of Turnsek & Cacovic or sliding shear failure based on the Mohr-Coulomb criterion.

2.3   Finite element method

2.3.1   Engineering Masonry Model

The Engineering Masonry Model is a recently developed material model for masonry in DIANA. This model has been developed by DIANA FEA and the Technical University of Delft. The figures and equations in this chapter are taken from (Schreppers, Garofano, Messali, & Rots, 2017). The model is mainly used for modelling failure of masonry walls (2D plane stress elements) or masonry structures (3D curved shell elements). Important characteristics of the Engineering Masonry Model are:

- The material model is a total-strain based continuum model
- Tensile, shear and compression failure modes
- Four in-plane crack directions possible: x, y and two diagonal directions with predefined angle.
- Orthotropic
- X-direction aligned with the bed-joints and y-direction aligned with the head-joints
- If the diagonal cracks are not occurring the model act as an orthotropic material with a Poisson's ratio of zero. (No coupling between the stiffness of the normal components and the in-plane shear component)

Furthermore, the Engineering Masonry model regards the following failure mechanisms:

- Tensile cracking of the bed- and head-joint
  - Secant nonlinear unloading and reloading
- Compressive crushing normal to the bed- and head-joint
  - Nonlinear non-secant unloading and reloading
- Cracking normal to the diagonal cracks
  - When the crack is opening, the tensile and shear stress is reduced. When the crack is closing, the model takes a linear stiffness equal to the initial stiffness.
  - The behaviour of the diagonal crack can be unrealistic for slender walls. Then the diagonal cracking can be deactivated.
- Frictional shear sliding
  - Shear stresses calculated with Coulomb friction.
- Out-of-plane shear-failure
  - Out-of-plane shear stiffness components are considered being linear elastic unless the option of out-of-plane shear failure is selected. In that case Coulomb friction is used.

The stresses in an element are defined by the strains in x- and y-direction and the maximum strain value $\alpha_{tensile}$ reached during the loading history. The corresponding stress at $\alpha_{tensile}$ is expressed as $\sigma_{rf,tensile}$. By means of the maximum value of the strain the secant unloading behaviour is determined. The tensile stress-strain curve is described by determining the ultimate strain with the tensile strength f_t , the crack energy G_{ft} and the crack bandwidth of the element h. The ultimate tensile strain occurs when the crack is fully open and the no stress-transfer is possible. This is determined with following formula:

$$\varepsilon_{ult} = \frac{2G_{ft}}{hf_t}$$

The following figure describes the tensile behaviour of the Engineering Masonry Model:
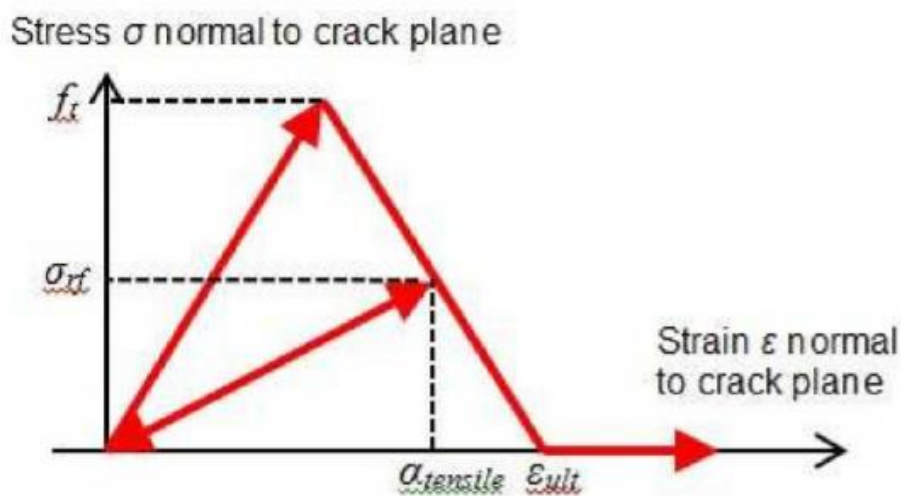
Figure 7: Cracking behaviour Engineering Masonry Model (Schreppers, Garofano, Messali, & Rots, 2017)

Crushing behaviour

The compressive stresses of an element in the x- and y-direction are defined by the strain and the minimum strain value α_{comp} reached during the loading history. The corresponding stress is expressed as $\sigma_{rf,compressive}$. The compressive stress-strain curve is described by determining the ultimate strain with the compressive strength f_c, the crack energy G_c and factor n. The factor n is used to determine the strain ε_{peak} at compressive strength with the following formula:

$$n = \frac{E\varepsilon_{peak}}{f_c}$$

The stress-strain curve is made up of a parabolic curve until the compressive strength and a linear softening curve until 10% of the compressive strength is reached. The ultimate strain ε_{ult} is equal to the strain corresponding to a zero stress level. This is determined with the following formula:

$$\varepsilon_{ult} = \varepsilon_{peak} + \max\left[0, \frac{2G_c}{hf_c} - \frac{f_c}{A^2E} - \frac{A+1}{A}\left(\varepsilon_{peak} - \frac{f_c}{E}\right)\right]$$

Where h is the crack bandwidth and A is defined as:

$$A = \left(\frac{E\varepsilon_{peak}}{f_c}\right)^{\frac{1}{3}}$$

The figure below shows the crushing behaviour of the Engineering Masonry Model
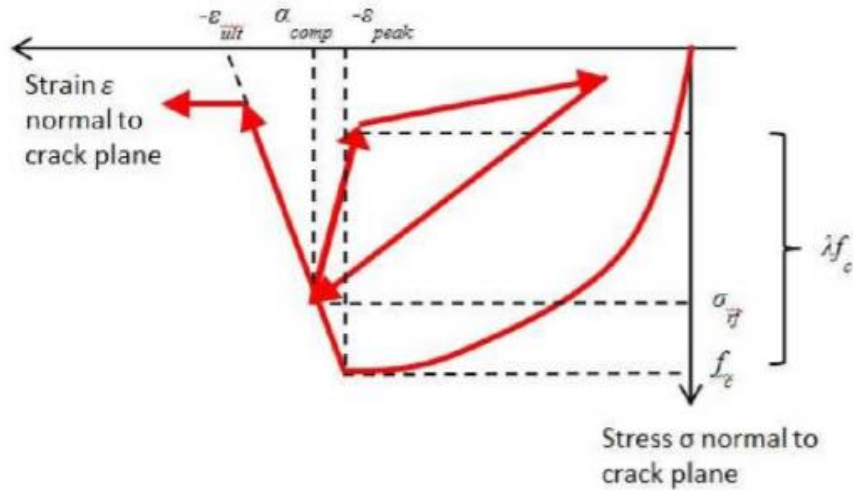
Figure 8: Compressive behaviour of Engineering Masonry Model (Schreppers, Garofano, Messali, & Rots, 2017)

λ in the figure represents the unloading factor. The factor can obtain values between 1 and 0. Where $\lambda = 1$ corresponds to secant unloading to the origin with stiffness $\frac{\sigma_{rf,compressive}}{\alpha_{comp}}$ and $\lambda = 0$ corresponds to unloading to zero stress with the initial stiffness and secant stiffness. For $\lambda = 0$ unloading with the initial stiffness is applied until the compressive stress is equal to $\lambda\sigma_{rf,compressive}$. Then the secant stiffness is applied until the origin. For reloading the curve goes with a straight line to the last loading extreme point. The secant stiffness is defined as:

$$E_{sec} = \frac{\lambda\sigma_{rf,compressive}}{\alpha_{comp} - \frac{\lambda\sigma_{rf,compressive}}{E}}$$

Shear behaviour

The in-plane shear stress τ is defined by the shear strain γ and the stress σ_{yy} normal to the bed-joint. The shear stress $|\tau|$ can not exceed the maximum stress τ_{max} which is formulated according to the Coulomb friction criterion as:

$$\tau_{max} = \max\left[0, c - \sigma_{yy}\tan(\varphi)\,\right]$$

Where c is the cohesion of friction and φ the friction angle of the masonry. The shear stress-strain curve is shown in the figure below:
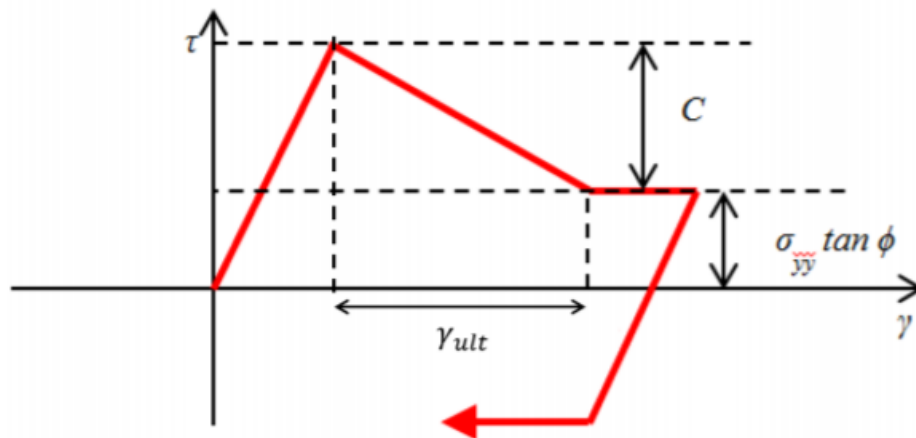
Figure 9: Shear behaviour of Engineering Masonry Model (Schreppers, Garofano, Messali, & Rots, 2017)

The figure shows a linear relation between the shear strain and stress until $\tau_{\max}$ is reached. Then the cohesion decreases until the cohesion reaches zero at a total shear strain of γ_{ult}, which is defined as:

$$\gamma_{ult} = \frac{2G_{fs}}{h * c} - \frac{c}{G}$$

Where h is the crack bandwidth, G_{fs} is the shear energy and G is the shear modulus. Lastly, when an integration point is cracked ($\alpha_{tension} > \frac{f_t}{E}$), the cohesion is reduced to zero.

Head-joint failure options

The Engineering masonry model has 4 options for how the failure of the head-joint is considered in the DIANA model. The user needs to choose one of these 4 head-joint failure options. The 4 failure options are:

1. Head-joint failure not considered: In this option the model does not consider diagonal cracks. Only cracking and crushing normal to the bed-joint and Mohr-Coulomb criterion are evaluated.
2. Direct input head-joint tensile strength: In this failure option the cracking and crushing normal to the head-joint is also considered. The tensile strength in both directions and the compressive strength in one direction which is used in both directions has to be explicitly defined by the user. Once again, diagonal cracks are not considered.
3. Diagonal stair-case cracks: The failure of the head-joint is assumed to happen as part of a diagonal stair-case crack. In this failure option, besides cracking and crushing normal to the bed-joint and shear failure, the cracking and shear-release of the diagonal stair-case cracks is also considered. The user has to define the angle with the bed-joint of the staircase crack, the bed-joint tensile strength and the frictional shear-stress in the bed-joint.
4. Tensile strength head-joint defined by friction: Similar to point 2, but now the tensile strength is calculated from the friction shear-stress in the bed-joint. A minimum tensile strength of the head-joint can also be explicitly defined. The effect of a high overburden load can be taken into account in this option.

2.3.2 Total Strain Crack Model

The total strain crack model is a constitutive model based on total strain and is developed according to the Modified Compression Field Theory (Vecchio & Collins, 1986). The Total Strain Crack Model offers three different constitutive models based on the crack orientation; fixed, rotating and combined. The difference lies in the different evaluations of the stress-strain relationships of the three variants. For the fixed crack orientation, the stress-strain relation is evaluated in a fixed coordinate system. For the rotating crack orientation, it is evaluated in the principal directions of the strain vector. For the combined crack orientation, a limit value for the total strain directs whether the crack orientation changes from rotating to fixed. For this research the focus is only on the Rotating Strain Crack Model.

The Total Strain Crack Model requires several material input parameters. These are the linear elastic material properties, the parameters for the tensile behaviour and the parameters for the compressive behaviour. The tensile behaviour can be modelled using different approaches. The following functions are based on fracture energy:

- Linear softening curve
- Exponential softening curve
- Nonlinear softening curve by Hordijk
- Nonlinear tension softening according to CEB-FIP Model Code 1990
- Nonlinear softening according to fib Model Code for Concrete structures 2010
- Nonlinear softening according to JSCE

Other tensile curves are:

- Constant tensile behaviour
- Linear behaviour based on ultimate strain
- Multilinear behaviour
- Brittle behaviour
- Tensile failure model for fiber reinforced concrete (CEB-FIP)
- User-supplied

The compressive behaviour can be modelled with a number of predefined curves. The predefined curves are:

- Constant curve
- Brittle curve
- Thorenfeld curve
- Linear hardening curve
- Multilinear curve
- Saturation hardening curve
- Parabolic curve
- Eurocode 2 1992-1-2 and Eurocode 4 1994-1-2
- Maekawa cracked concrete curves
- CEB-FIP Model Code 1990
- Fib Model Code for concrete structures 2010
- Hognestad parabola
- Eurocode 2 EN1992-1-1

All the above curves have secant unloading behaviour, except the Maekawa cracked concrete curves. These contain nonlinear unloading behaviour.

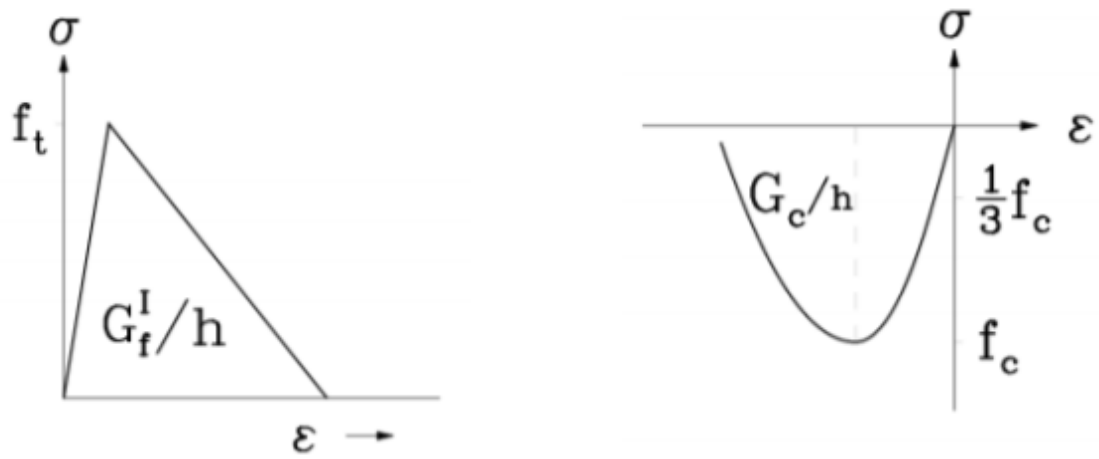For this research the following tensile and compression curves have been chosen:

Figure 10: Linear tensile softening curve (left) and parabolic compression curve (right) (DIANA FEA)

3 Case study

In this chapter a description is given of the wall façades that have been used in this research. The walls have been modelled in 2D with three different methods. Namely, the Finite-element method, the SLaMA method and the EF method. For this study it was important that the material properties and modelling assumptions had to be as consistent as possible within the three different methods. Furthermore, for researching the influence of the geometrical irregularities on the accuracy of EF and SLaMA, several geometrical irregularities have been grouped. These geometrical irregularities were then quantified by indices. The influence of these indices on the accuracy of the calculation methods will be researched in the next chapter with a sensitivity analysis.

3.1 Case study description

3.1.1 Material Properties

For all models, one specific material has been implemented, namely Clay-Brick masonry from prior to 1945. The material properties of this specific masonry type has been given below and are based on the NPR-9998:2018:

Table 1: Material properties masonry

Material properties			Unit
E_x	2500	$* 10^6$	N/m2
E_y	5000	$* 10^6$	N/m2
G_{xy}	2000	$* 10^6$	N/m2
ρ	1900		kg/m3
$f_{ma;b;per}$	0.067	$* 10^6$	N/m2
$f_{ma;t;par}$	0.2	$* 10^6$	N/m2
$G_{ft;per}$	7		N/m
$f_{ma;m}$	5.67	$* 10^6$	N/m2
$G_{f;c}$	6667		N/m
μ	0.75		-
c	0.2	$* 10^6$	N/m2
$G_{f;v;par}$	67		N/m

3.1.2 Irregularity indices

The following geometrical irregularities were identified:

1. Opening percentage irregularity: irregularity based on the size of the openings.
2. Slender pier irregularity: irregularity based on the slenderness of the piers.
3. Centre of mass irregularity: irregularity based on the location of the openings.

Note that in (Parisi & Augenti, 2012) four basic irregularities were defined. These irregularities are not present in any of the models made. This to avoid disturbances in the sensitivity analysis.

For the assessment of the influence of irregularities on the accuracy of the simplified calculation methods for the in-plane behaviour of the wall, for each geometrical irregularity a global irregularity index has been defined. This index specifies whether a wall is regular (i = 0) for its specific geometrical irregularity or irregular (0 < i ≤ 1).

Starting with the opening irregularity, the global irregularity index is defined by:

$$i_o = \frac{L_o}{L} = \sum_{k=1}^{n} \frac{L_k}{L}$$

Where L_o is the total opening length in a wall or in other words, the summation of all opening lengths(L_k) in a wall façade.

Secondly, the slender pier irregularity is defined as follows:

$$i_s = \frac{n_s}{n_p}$$

Where n_s is the number of slender piers in a wall and n_p is the total number of piers in a wall. Before one can assess the number of slender piers, a definition of a slender pier is needed. From (NPR 9998-2018) a slender pier is defined as a pier with a slenderness ratio (height/length ratio) higher than 2. This definition is also used for the determination of n_s.

For the centre of mass irregularity the following definition applies:

$$i_c = \frac{x_c}{0.25L}$$

Where x_c is the x-coordinate of the centroidal axis in the wall. With this definition one can easily obtain a quantification for the location of the openings.

The figure below illustrates the irregularity index of the centre of mass:
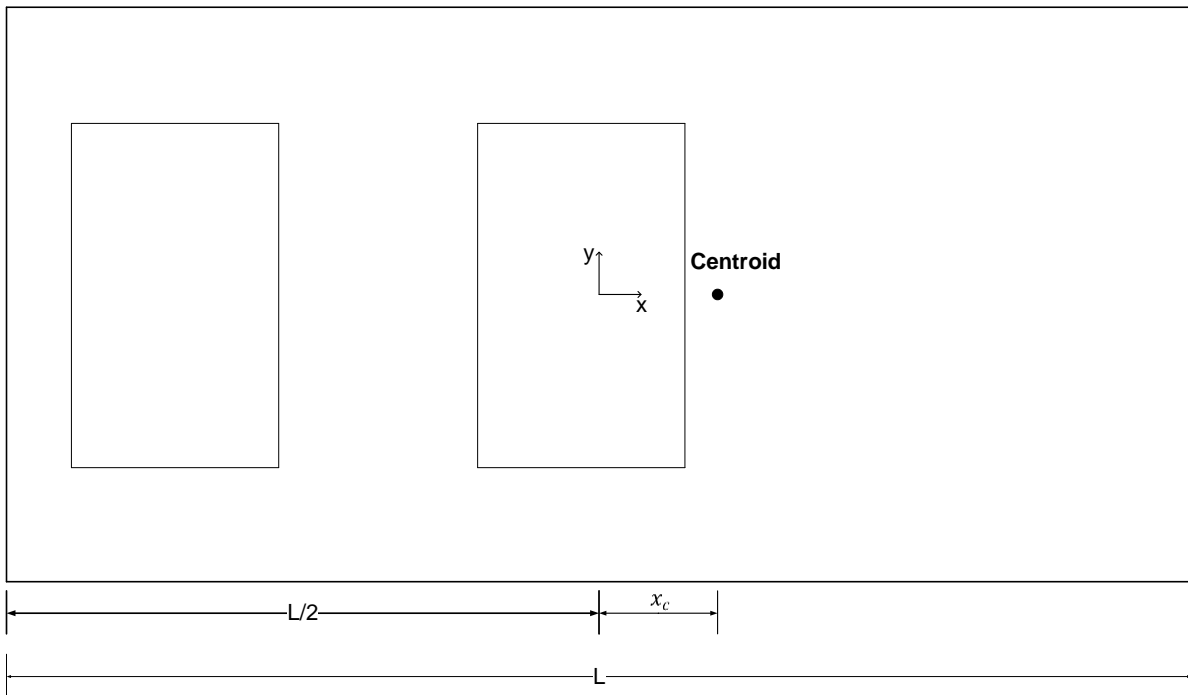
Figure 11: Irregular wall with centre of mass irregularity

3.1.3 Geometry & Loads

In this chapter the wall geometries are illustrated. The walls are sorted in four groups:

1. Regular wall
2. Opening percentage irregularity
3. Slender pier irregularity
4. Centre of mass irregularity

Furthermore, the applied axial force and the weak transversal load direction is illustrated in each figure. For all wall façades a thickness of 208 mm is applied.

3.1.3.1 Regular wall
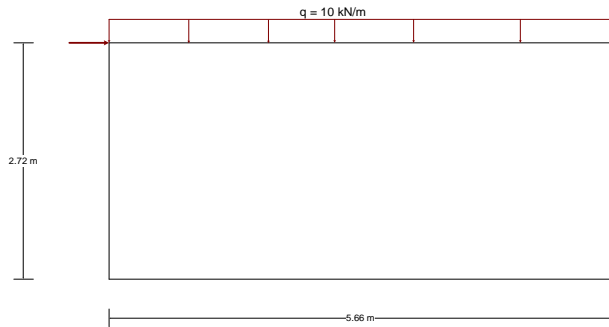
Figure 12: Wall 1: Regular wall with no irregularities

3.1.3.2 Opening percentage irregularity
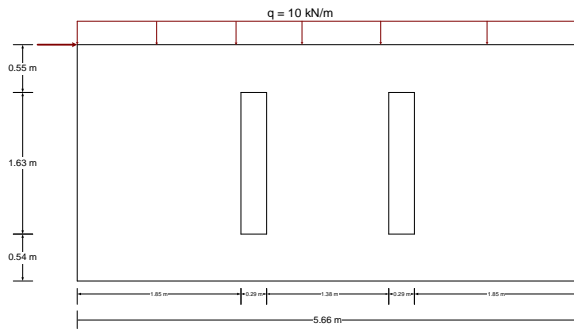
Figure 13: Wall 2: Irregular wall with $i_o = 0.1$
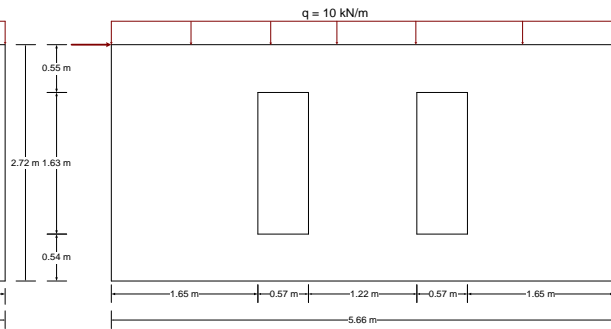
Figure 14: Wall 3: Irregular wall with $i_o = 0.2$
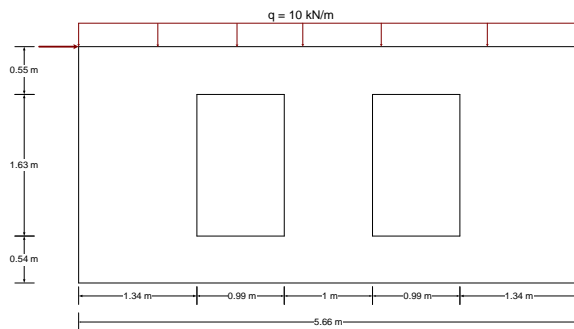
Figure 15: Wall 4: Irregular wall with $i_o = 0.35$
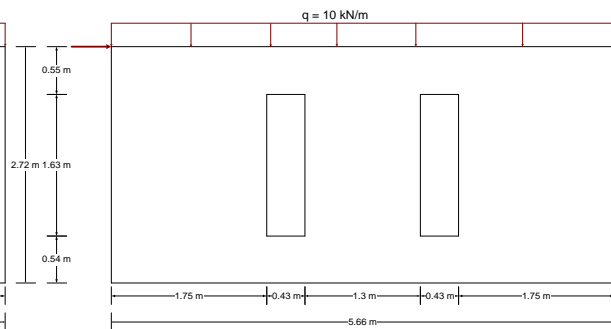
Figure 16: Wall 5: Irregular wall with $i_o = 0.15$

3.1.3.3   Slender pier irregularity

For these geometries $i_o = 0.35$ and is kept constant while i_s will vary:
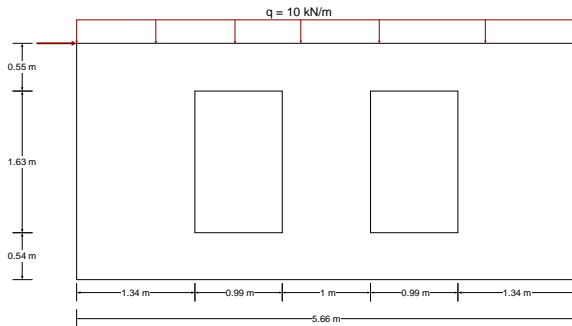
Figure 17: Wall 4: Irregular wall with $i_s = 0$
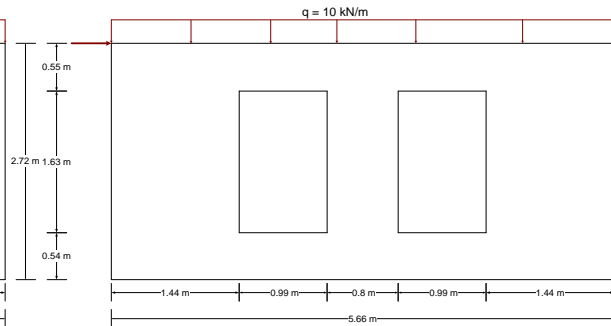
Figure 18: Wall 7: Irregular wall with $i_s = 0.333$
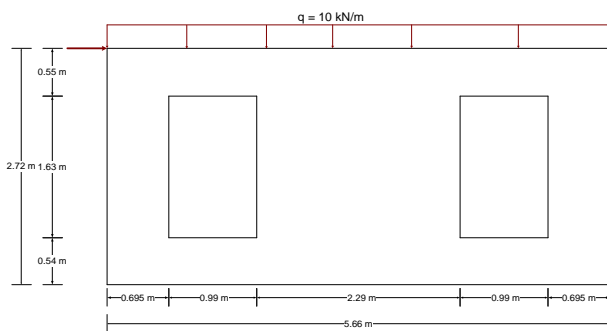
Figure 19: Wall 8: Irregular wall with $i_s = 0.667$
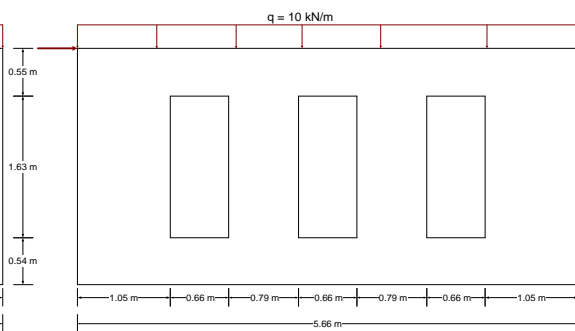
Figure 20: Wall 6: Irregular wall with $i_s = 1$

3.1.3.4 Centre of mass irregularity

For the following walls these indices are applied, $i_s = 0.333$ and $i_o = 0.35$:
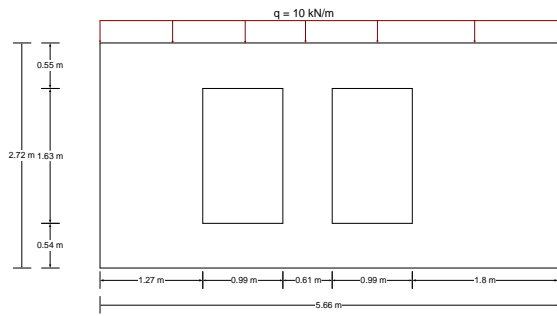
Figure 21: Wall 9: Irregular wall with $i_c = 0.1$
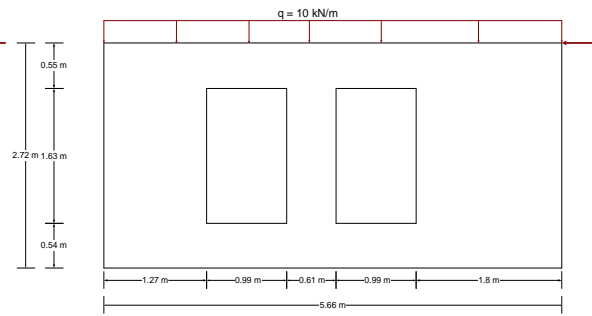
Figure 22: Wall 10: Irregular wall with $i_c = 0.2$
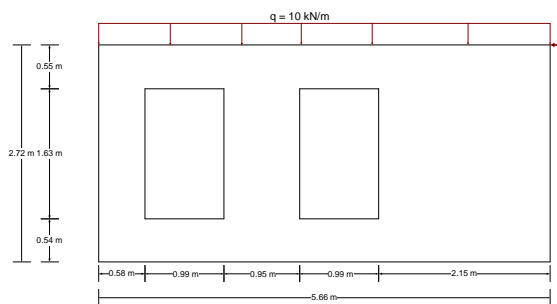
Figure 23: Wall 11: Irregular wall with $i_c = 0.3$
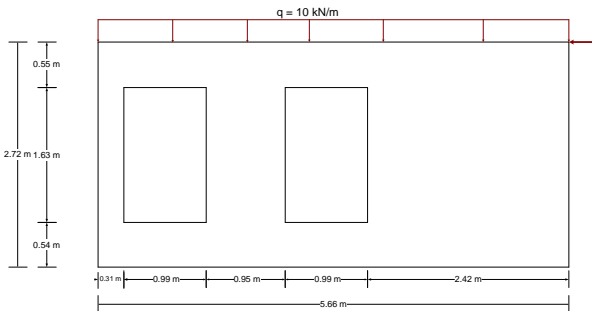
Figure 24: Wall 12: Irregular wall with $i_c = 0.4$

3.2 2D FEA

For the Finite element analysis DIANA 5.3 is used to perform the NLPO analysis. All material properties used in the DIANA models are based on the NPR 9998-2018 as noted in the previous chapter. Furthermore, some assumptions had to be made in the FEM analysis to produce an equivalent model as in the other methods. These assumptions and also the material model will be presented in this chapter.

3.2.1 Material model

The material model that has been applied in DIANA is the engineering masonry model. Within this material model, the user has the choice to select the specific failure type occurring. For this research it has been chosen to only produce results for the 'Tensile strength head-joint defined by bed-joint frictional shear stress' failure type. This is one of the failure types that was recommended in (Schreppers, Garofano, Messali, & Rots, 2017). The total-strain crack material model could also be used for this research due to unidirectional loading in all walls, but this material model and the application of the other three failure types is out of the scope of this research.

3.2.2 Model assumptions

For the DIANA model several assumptions have been made, and these were:

- Quadratic mesh order is applied for the elements.
- A mesh size of 0.1 m is used.
- Q8MEM plane stress elements used for the masonry wall.
- L7BEN beam elements used for the floors.
- Only flexible floors have been taken into consideration.
- A prescribed deformation load is applied at the top corner of the wall façade.

3.2.3 Analysis parameters

For the models a structural nonlinear analysis is done in DIANA. Below an overview of the analysis parameters is given:

Analysis settings	Applied in model
Nonlinear effects	Physical, Geometrical
Arc-length control	Not applicable
Load step size	0.05-0.08 mm
Max. number of iterations	100
Numerical method	Secant (Quasi-Newton)
Convergence norm	Energy

3.2.4 Modelling with lintels

Lintels can have an influence on the in-plane behaviour of a masonry wall. To research this, two models were made of wall 2 and 8 where lintels were included above the opening. The lintels were 20 mm high and were extended from both sides of the opening with 10 mm. Furthermore, the lintels had an Young's modulus of 20000 MPa and a tensile strength of 10 MPa. In chapter 4 the results are given of these models and in chapter 5 the results are further discussed.

3.3   2D SLaMA

In this chapter the general assumptions made in the SLaMA assessment will be explained. The SLaMA method has been explained in chapter 2.1.

3.3.1   Effective height method

For unreinforced masonry walls with different openings and weak pier-strong spandrel mechanisms it is advised in (Moon F. L., 2004) that the effective height of a rocking pier is equal to the height over which a diagonal strut is expected to develop.

3.3.2   Axial force

The axial force on the piers is calculated analytically, by adding up the self-weight of the pier with the axial forces working on top of the pier. There is no load redistribution during the rocking or failure of the pier. This is a large difference with DIANA, which constantly makes sure during the analysis there is an equilibrium of forces.

3.3.3 Boundary conditions

In the SLaMA method two different boundary conditions are possible at the ends of a pier, namely double clamped boundary conditions or cantilevered boundary conditions (free at the top of the pier). The user needs to assume one of the two options. In this research, this assumption is based on the following approach below:

Assume the piers to behave under double clamped condition.

↓

Determine the shear capacities of the piers based on this assumption.

↓

Assume these piers to behaves similar to a slender column. And calculate the moments at the position of the spandrel.

↓

Calculate based on these moments the required shear capacity of the spandrels to make equilibrium with the moments.

↓

Calculate the shear capacity based on the formulas described in the NPR9998:2018 Appendix G.

↓

If the shear capacity is higher than the required shear capacity than the pier behaves under double clamped conditions.

If the shear capacity is lower than the required shear force than the pier behaves cantilevered.
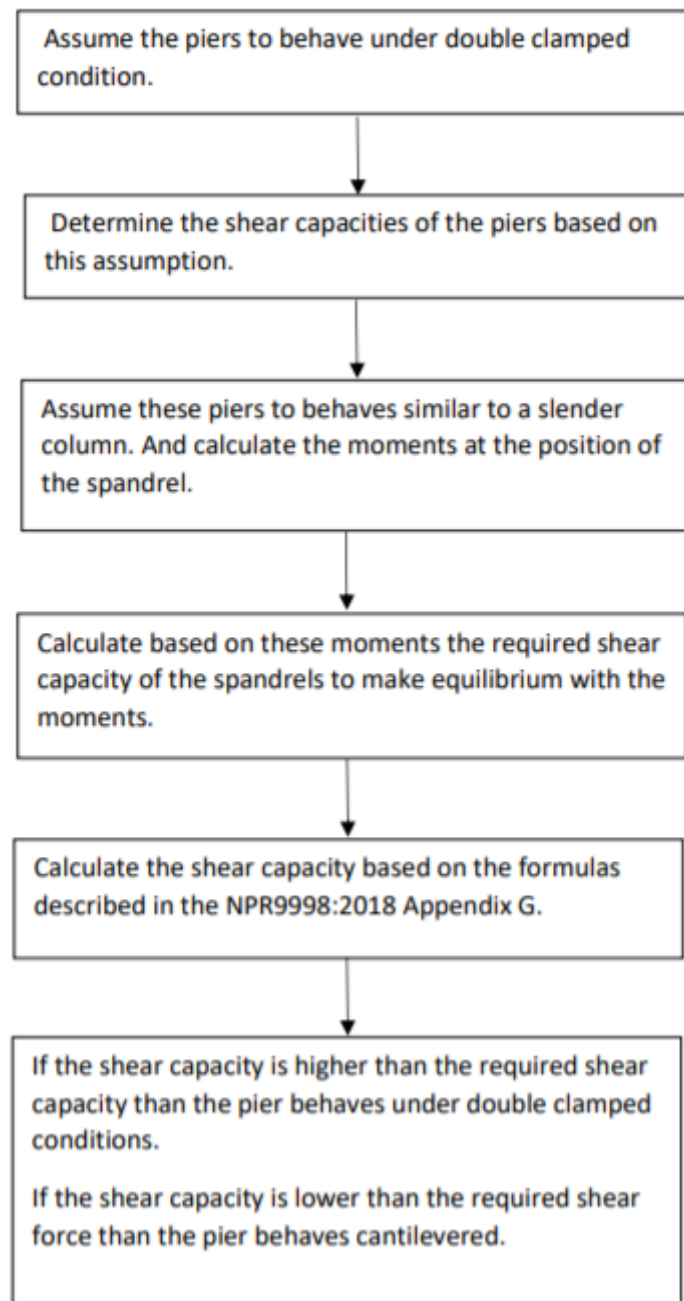
Figure 25: Boundary conditions assessment (Nidal Ennali)

3.3.4 Formulation of the boundary conditions in SLaMA

The results of the SLaMA are based on the assessment approach of the boundary condition described in the previous chapter. This approach was still not accurate enough, because the boundary conditions could be either cantilever or double clamped. In reality, conditions in between are more accurate, because the connections between piers and spandrels are neither infinitely rigid nor hinged. For this reason two new formulations have been developed.

The first formulation is rather straightforward and is an addition to the assessment approach of chapter 3.3.3. The last step of this approach is altered and instead a different step is done. It still holds that if the shear capacity is higher than the required shear capacity, then the pier will behave double clamped. For cantilever boundary condition, the required shear capacity needs to be equal to zero due to hinged connection between pier and spandrel. If the required shear capacity is between the shear capacity and zero, linear interpolation is done to calculate the intermediate results.

The second formulation is more complicated and requires linear elastic frame analysis. For this research, Matrixframe is used to do these analyses. The goal is to verify how much the more simplified first formulation differs from this advanced approach, because this formulation is more time consuming. The first step is to model the piers and spandrels as frames in Matrixframe. Then the linear analysis is run and the internal forces are computed. Based on the internal forces of the framework, a ratio of capacity over the demand is calculated for each pier and spandrel at their connections. Then the ratio of capacity over demand of the piers are respectively compared with their connected spandrels. If the capacity over demand of the spandrel is higher than the capacity over demand of the pier, this would mean that the pier will crack before the spandrel during lateral loading which is a sign of weak pier-strong spandrel behaviour. Here double clamped conditions are assumed. If the capacity over demand of the spandrel is lower than the capacity over demand of the pier, linear interpolation is performed to assess the boundary conditions between cantilever and double clamped. This is done by stating that a capacity over demand of the spandrel equal to zero is in correspondence with cantilever boundary conditions and for the ratios between cantilever and double clamped conditions, the boundary conditions are calculated by use of linear interpolation.

3.3.5 Shear capacity

The calculation of the shear capacities of the piers are based on the formulas of NPR9998-2018. The critical shear capacity of a pier corresponds to the failure mechanism with the lowest value for the shear capacity. Subsequently, the critical shear capacities of all the piers in a wall are summated and form the global shear capacity of a wall.

3.3.6 Displacement capacity

The displacement capacity of a wall is based on the individual drift capacities of the piers. These drift capacities are put together in such a way, that if the first pier fails the global shear capacity will have a drop equal to the critical shear capacity of the failed pier. It should be taken into consideration that the drop in shear capacity has to be lower than 50%, otherwise global failure of the wall is assumed.

3.4 2D EFM

For the equivalent-frame method, the program 3MURI 12.2.1 is used to model the 2D walls. This program is still being used for the seismic assessment of the URM building at Arcadis.

For the shear failure criterion, Mohr-Coulomb has been chosen. This is the only assumption that has been made in the model. For the rest, the walls have been modelled as the other two methods and no additional assumptions have been made in the modelling of the façades.

3.4.1 Turnsek & Cakovic

3MURI gives the user an option where the user has to choose which of the shear failure mechanism is prone to occur, diagonal shear failure based on the equation of Turnsek & Cakovic or sliding shear failure based on the Mohr-Coulomb criterion. In this research the Mohr-Coulomb criterion is used, because this is also according to the NPR9998 the most occurring failure mechanism for this type of masonry (Clay-Brick pre-1945). However, in the next chapter Walls 2 and 8 have been modelled with shear described by Turnsek & Cakovic and have been compared with the Mohr-Coulomb criterion. The results are further discussed in the discussion.

4 Results

In this chapter the results of the three calculation methods for all models are presented.

4.1 FEA results

This chapter shows the DIANA results for all the models. For each model the principal strain contour plot is shown. From these results the observed failure mechanism is deducted. Lastly, the pushover curve is presented.

4.1.1 Wall 1: Regular wall

In the figure below the principal strain plot of wall 1 is shown:
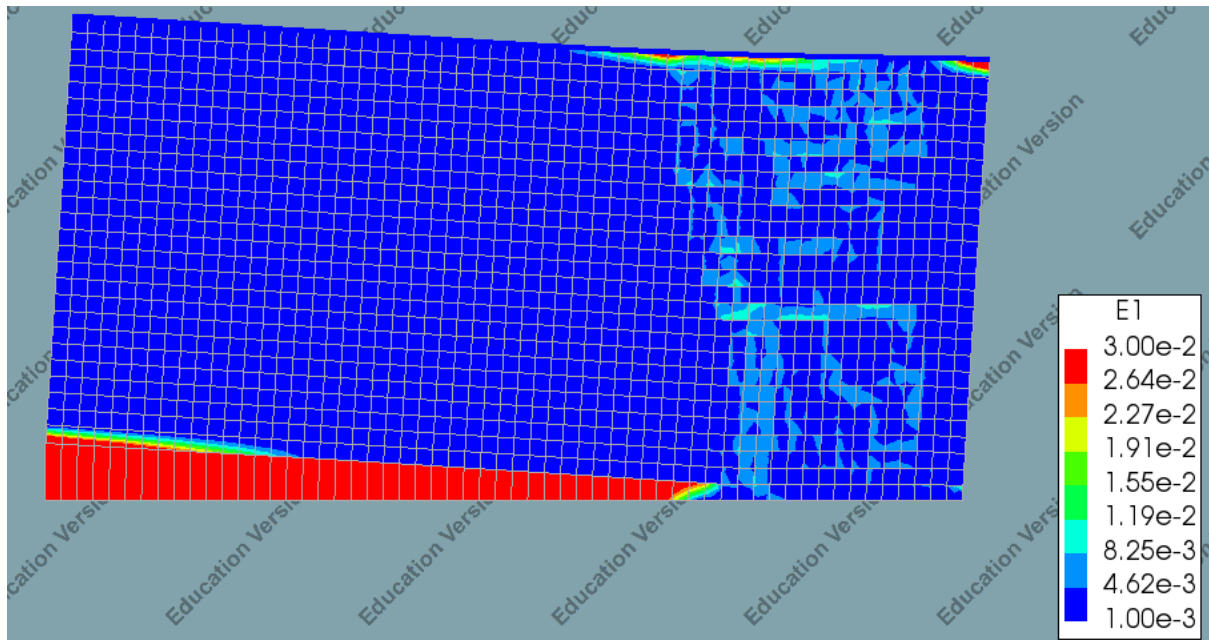
Figure 26: Principal strain contour plot Wall 1

The observed failure mechanism is shear failure of the wall. This can be deducted from the diagonal cracks developing when looking at the principal strain plot.

The pushover curve corresponding to Wall 1 is presented below:
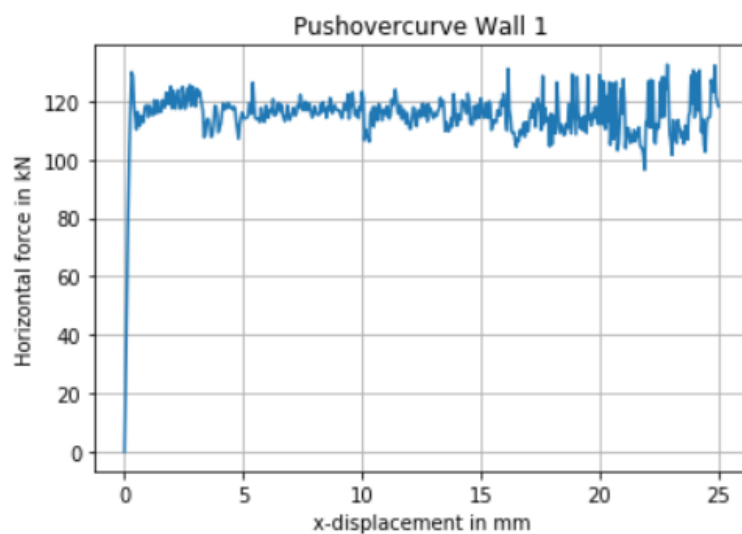
Figure 27: Pushover curve DIANA Wall 1

4.1.2   Wall 2-5: Opening irregularity

In the figure below the principal strain plots of walls 2-5 is shown:
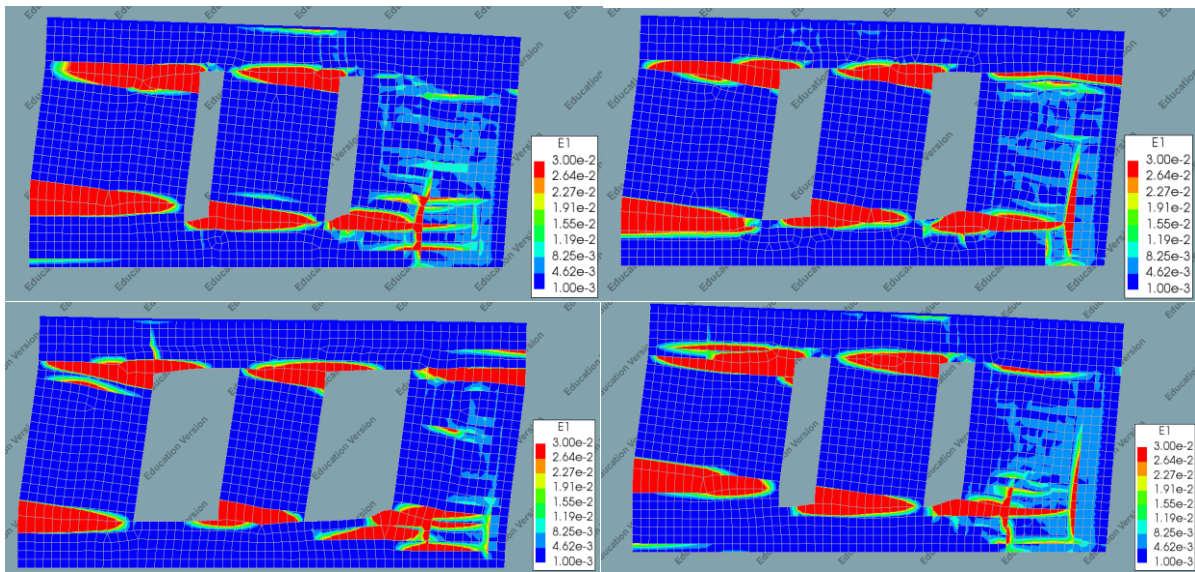
Figure 28: Principal strain plot Wall 2 (upper-left), Wall 3 (upper-right), Wall 4 (lower-left) and Wall 5 (lower-right)

The observed failure mechanism for the first two piers for all four walls is rocking. This can be deducted from the cracks developing in the upper right and lower left corner of each pier when looking at the principal strain plot. For the last pier, it is slightly more difficult to ascertain a particular failure mechanism. Only for wall 3 and 4 one can see rocking patterns with slight shear failure patterns, but for wall 2 and 5 a combination of shear and rocking failure is present.

The pushover curve corresponding to Wall 2 until 5 is presented below:
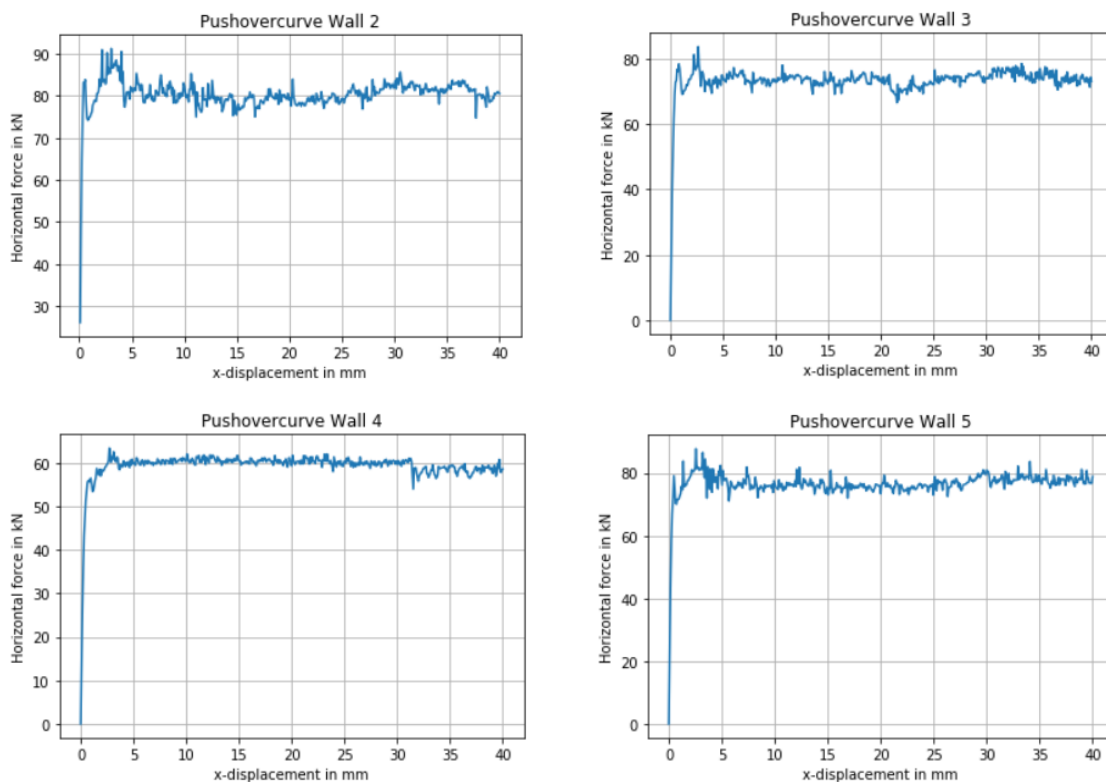
Figure 29: Pushover curve Wall 2 (upper-left), Wall 3 (upper-right), Wall 4 (lower-left) and Wall 5 (lower-right)

4.1.3 Wall 6-8: Slender pier irregularity

In the figure below the principal strain plot of wall 6 until 8 is shown:
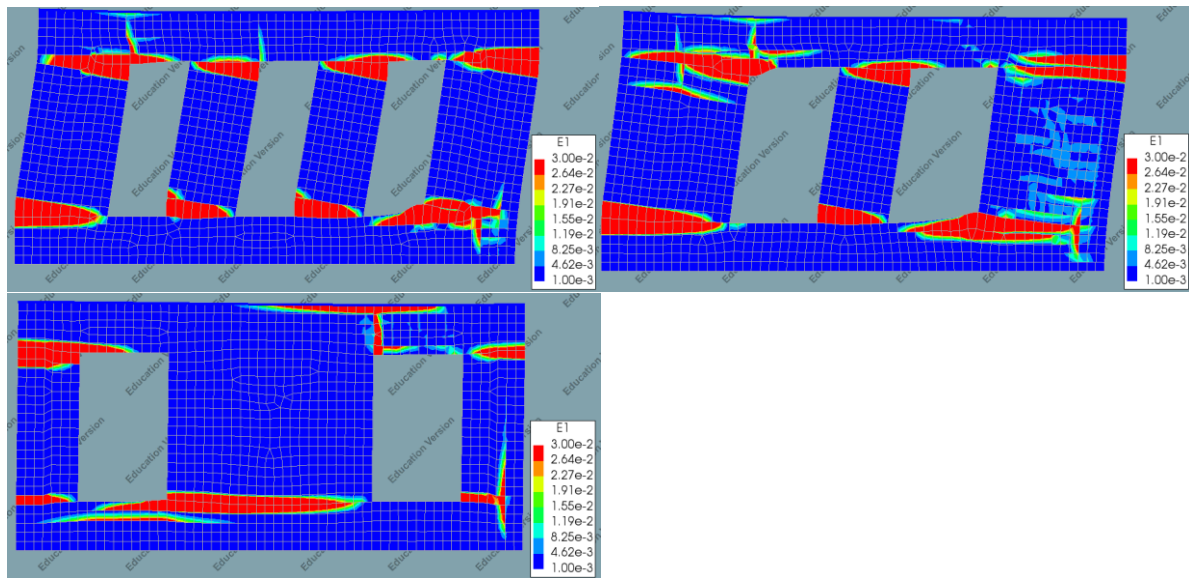
Figure 30: Principal strain plot Wall 6 (upper-left), Wall 7 (upper-right) and Wall 8 (lower-left).

The observed failure mechanism is shear failure of the wall. This can be deducted from the diagonal cracks developing when looking at the principal strain plot.

The pushover curve corresponding to Wall 6 until 8 is presented below:
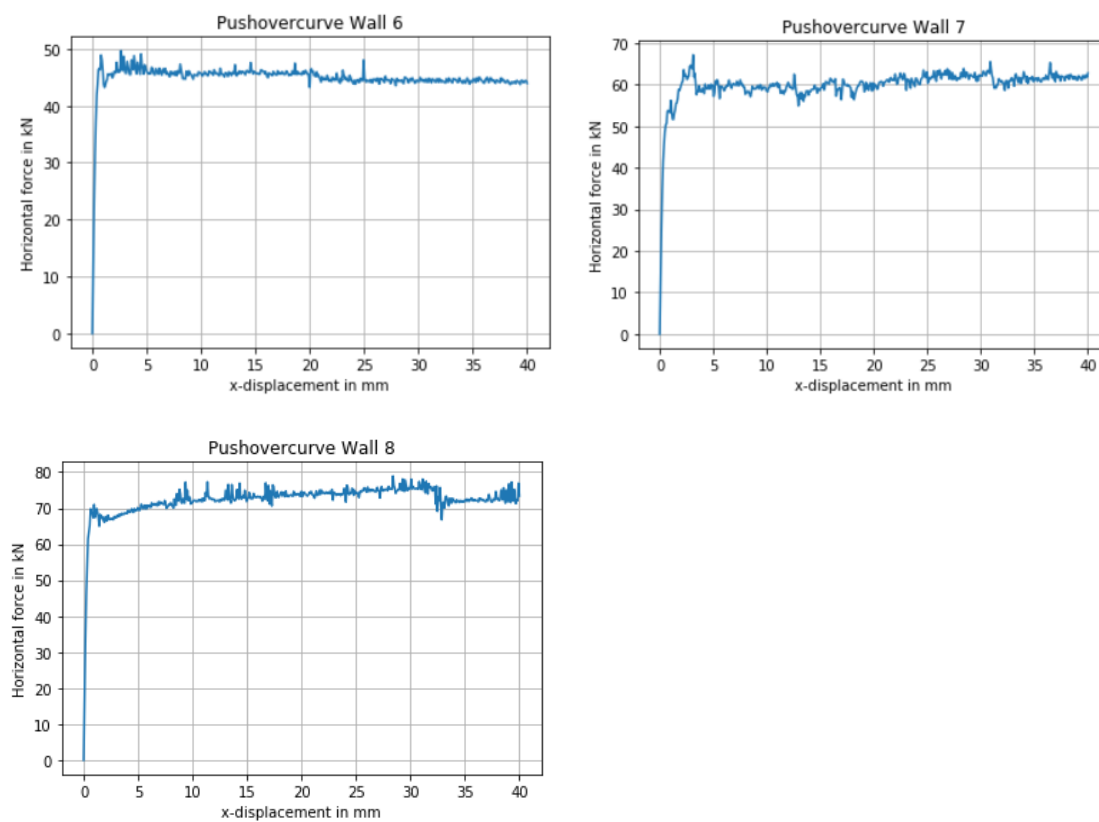
Figure 31: Pushover curve Wall 6 (upper-left), Wall 7 (upper-right) and Wall 8 (lower-left).

4.1.4 Wall 9-12: Centre of mass irregularity

In the figure below the principal strain plot of wall 1 is shown:
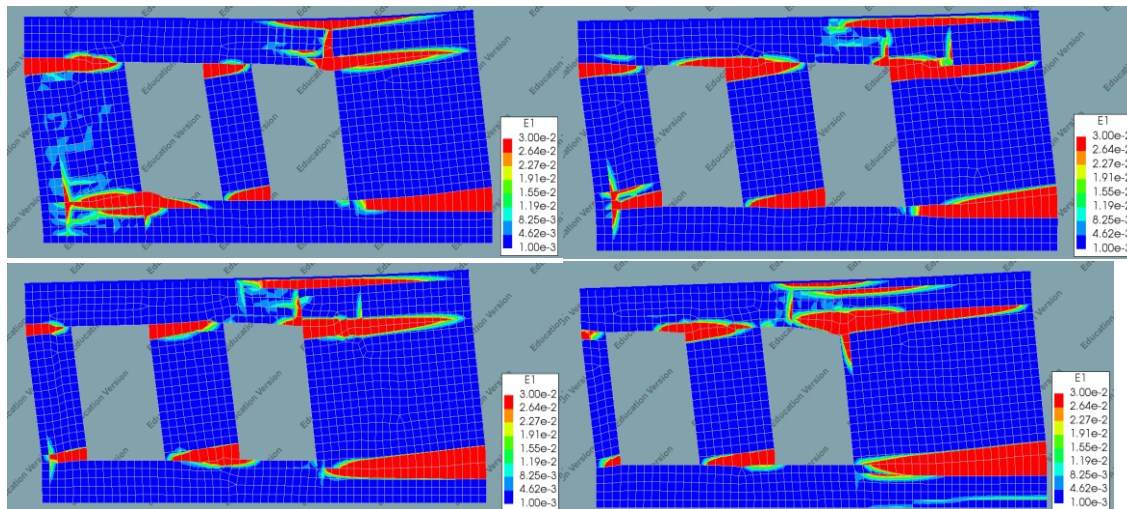
Figure 32: Principal strain plot Wall 9 (upper-left), Wall 10 (upper-right), Wall 11 (lower-left) and Wall 12 (lower-right)

The observed failure mechanism is shear failure of the wall. This can be deducted from the diagonal cracks developing when looking at the principal strain plot.

The pushover curve corresponding to Wall 9 until 12 is presented below:
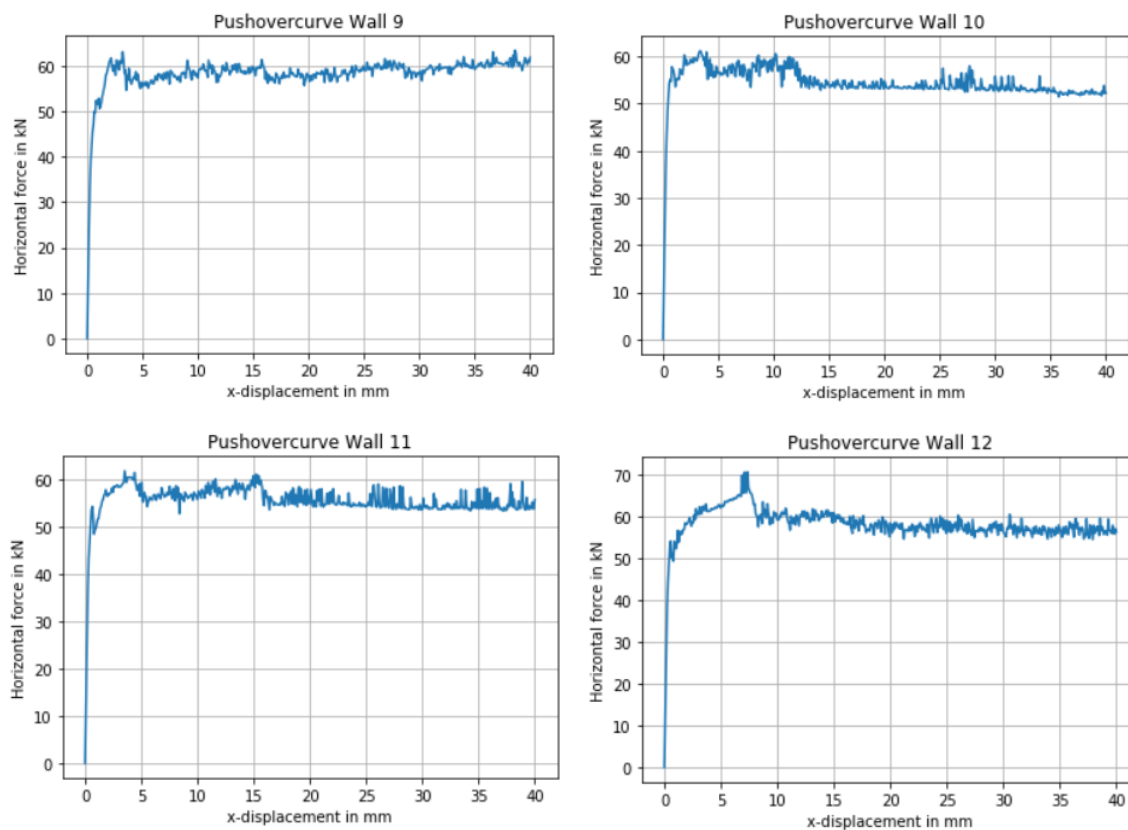
Figure 33: Pushover curve Wall 9 (upper-left), Wall 10 (upper-right), Wall 11 (lower-left) and Wall 12 (lower-right)

4.1.5 Rotating Strain Crack Model

Below the results are given for Rotating Strain Crack Model and Engineering Masonry for wall 2 and 8.
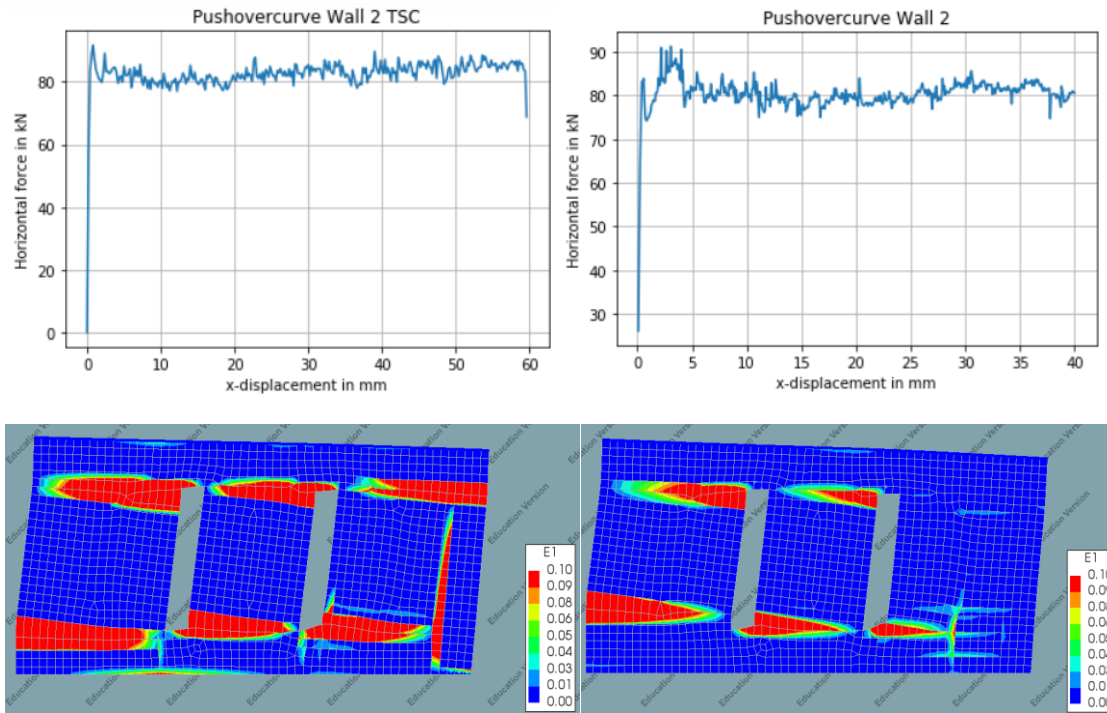
Figure 34: Results Wall 2 Total Strain Crack Model (left) & Engineering Masonry Model (right)
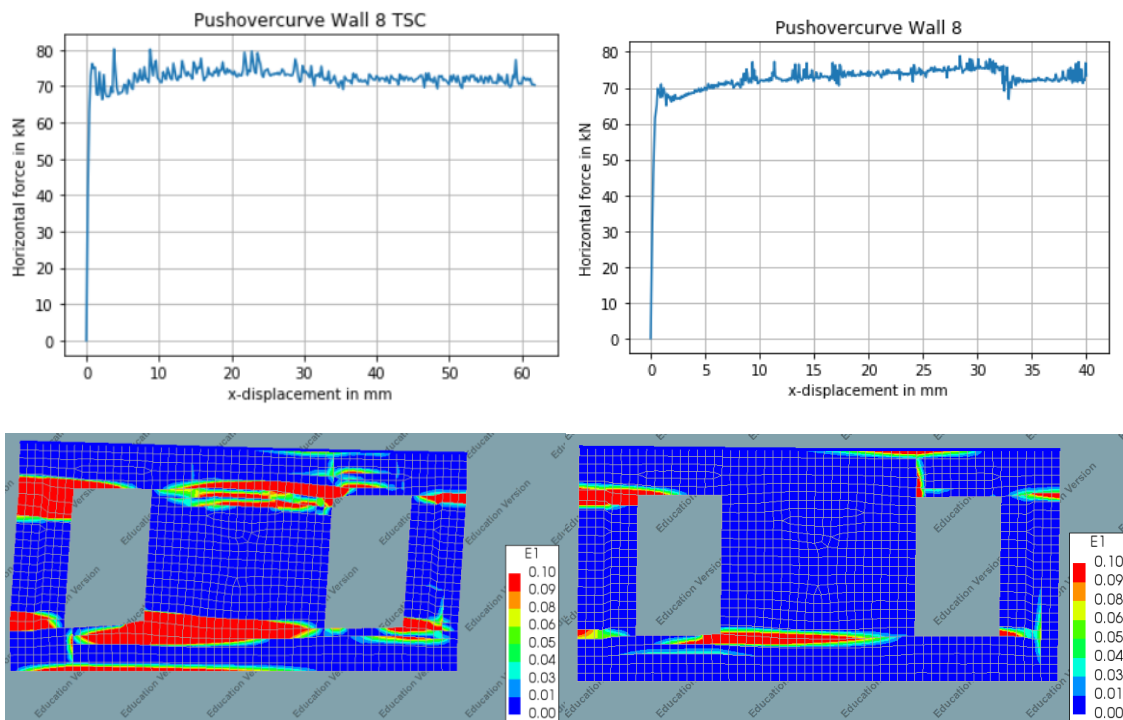
Figure 35: Results Wall 8 Total Strain Crack Model (left) & Engineering Masonry Model (right)

4.1.6 Models with lintels

To understand the influence of lintels on the in-plane behaviour of the wall façade, wall 2 and wall 8 have been modelled with lintels. The lintels stretch from both sides of the opening out with 10 cm and have a height of 20 cm. Below the results are presented of these models:
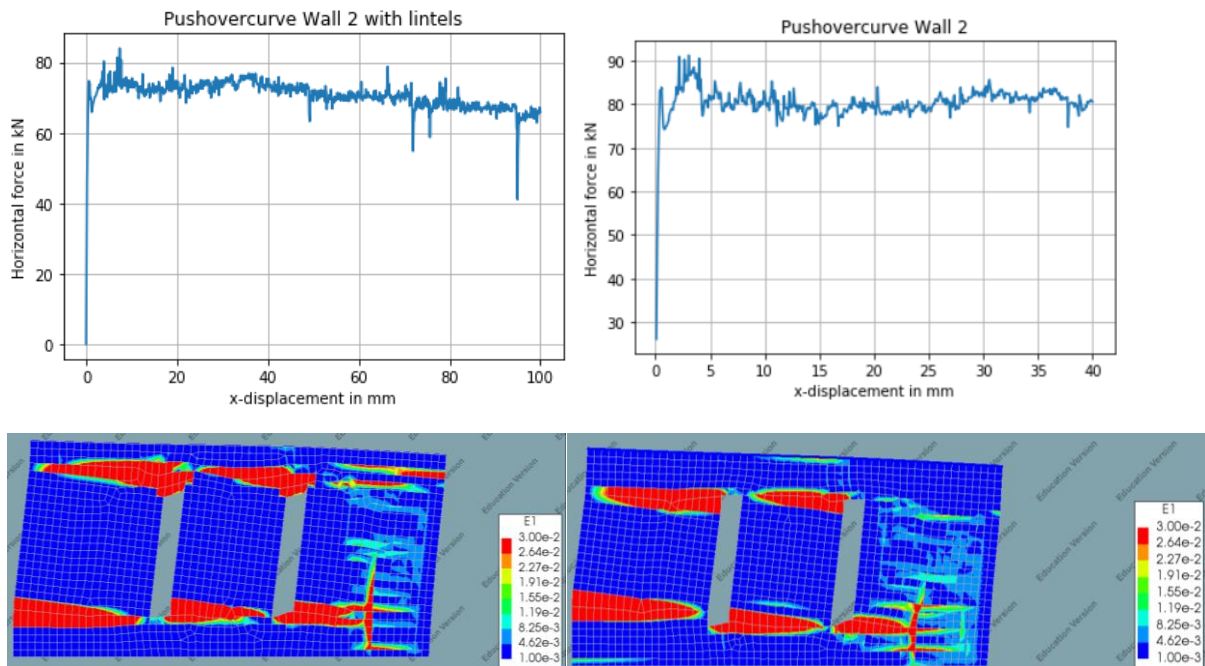
Figure 36: Results Wall 2 with lintels (left) & without lintels(right)
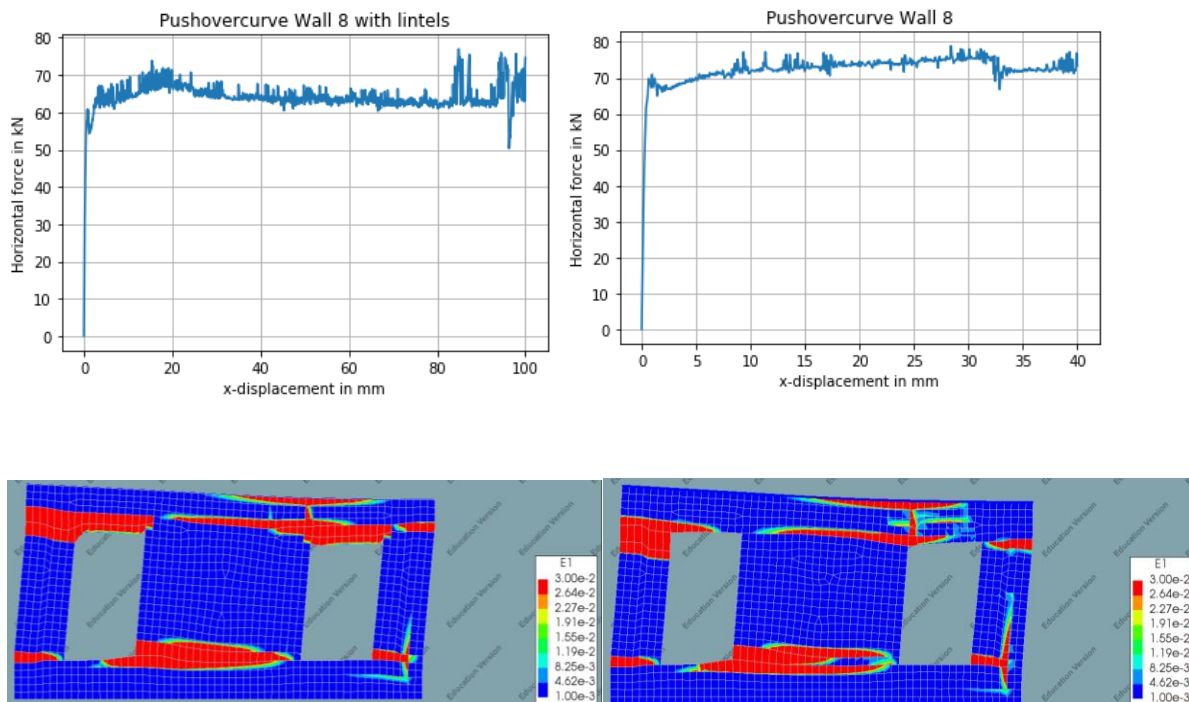
Figure 37: Results Wall 8 with lintels(left) & without lintels(right)

Summary

In this section the results were given of the models in DIANA. In the below figures the results are once again given, but categorized for each variation.
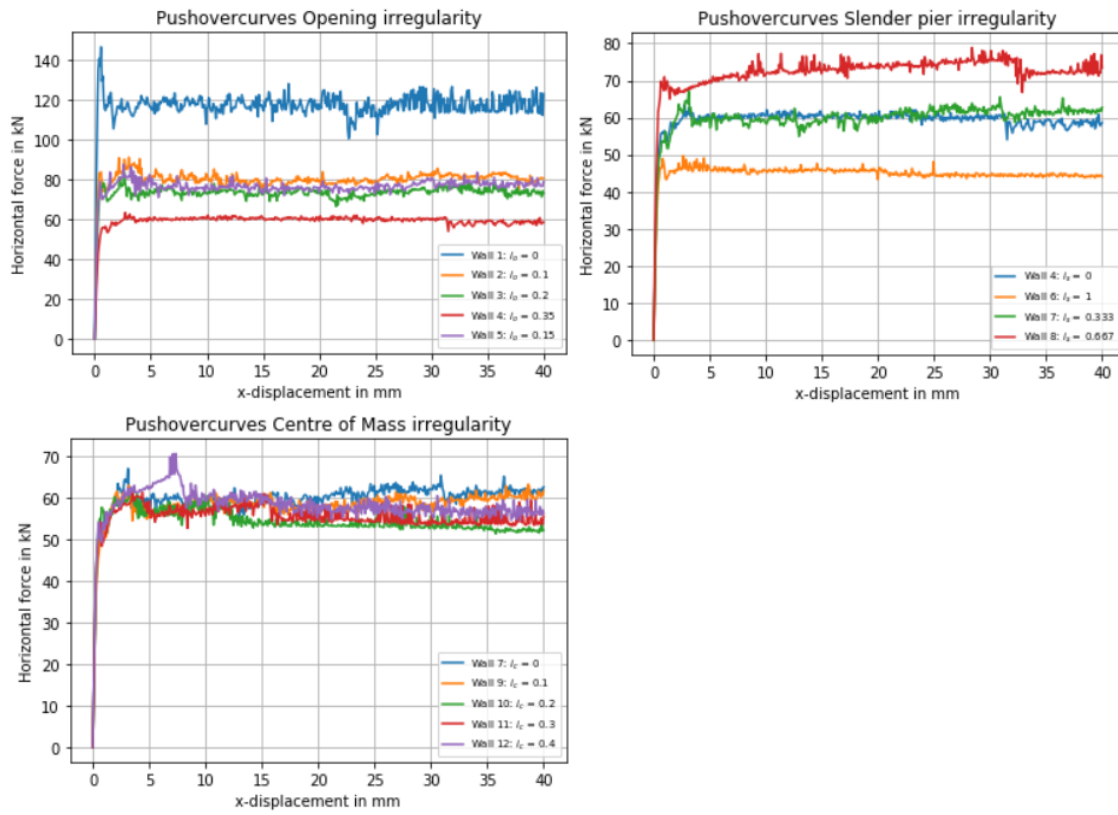
Figure 38: Pushovercurves DIANA for each variation.

4.2 2D EFM results

In this chapter the results from 3MURI are presented. For each model the failure mechanisms and the pushover curves are illustrated. First the legend is shown below for the different failure mechanisms possible:

Figure 39: Legend Failure mechanisms

4.2.1 Wall 1: Regular wall

Below the failure mechanism and pushover curve is presented for Wall 1:
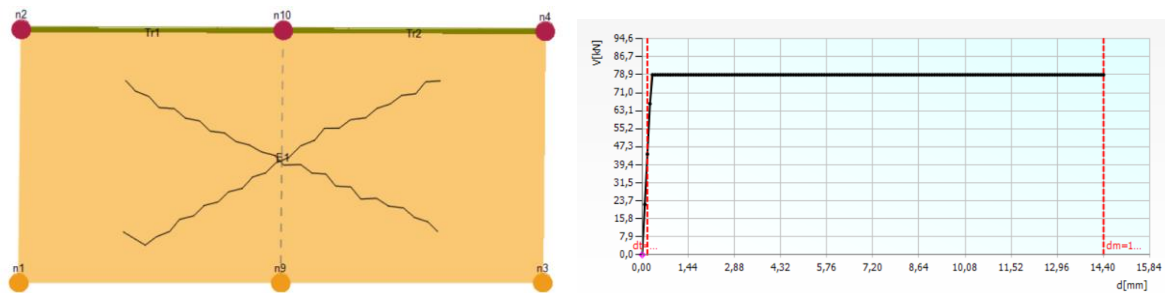
Figure 40: Failure mechanism & Pushover curve Wall 1

4.2.2 Wall 2-5: Opening irregularity

Below the failure mechanisms are presented for Walls 2-5:
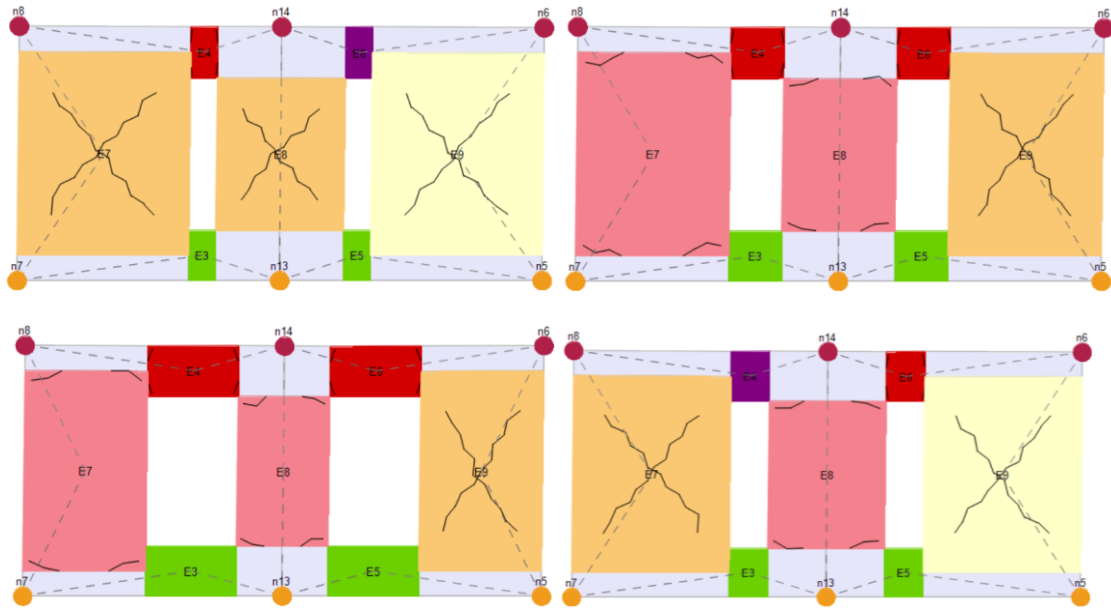
Figure 41: Failure patterns 3MURI Wall 2 (upper-left), Wall 3 (upper-right), Wall 4 (lower-left) and Wall 5 (lower-right)

And below the pushover curves corresponding to Walls 2-5 are given:

Figure 42: Pushover curve 3MURI Wall 2 (upper-left), Wall 3 (upper-right), Wall 4 (lower-left) and Wall 5 (lower-right)

4.2.3 Wall 6-8: Slender pier irregularity

Below the failure mechanisms are presented for Walls 6-8:
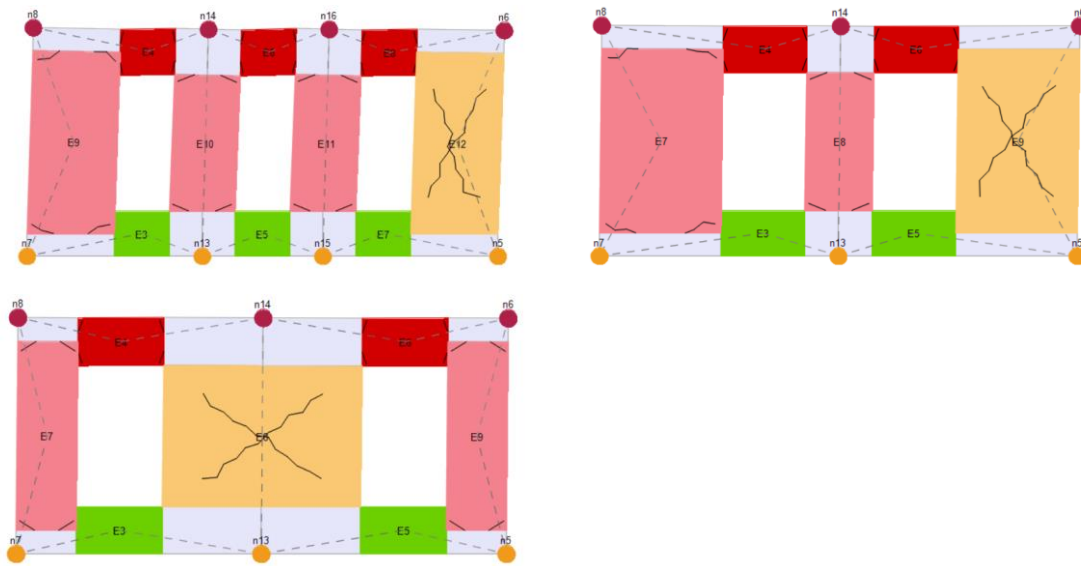
Figure 43: Failure patterns 3MURI Wall 6 (upper-left), Wall 7 (upper-right), Wall 8 (lower-left)

And below the pushover curves corresponding to Walls 6-8 are given:

Figure 44: Pushover curve 3MURI Wall 6 (upper-left), Wall 7 (upper-right), Wall 8 (lower-left)

4.2.4 Wall 9-12: Centre of mass irregularity

Below the failure mechanisms are presented for Walls 9-12:
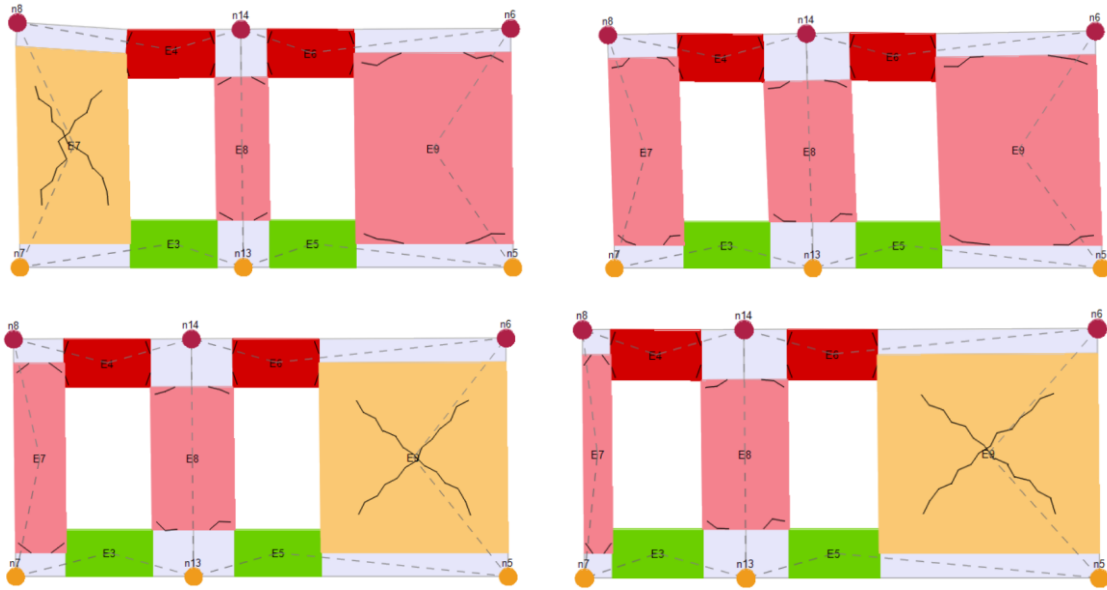
Figure 45: Failure patterns 3MURI Wall 9 (upper-left), Wall 10 (upper-right), Wall 11 (lower-left) and Wall 12 (lower-right)

And below the pushover curves corresponding to Walls 9-12 are given:
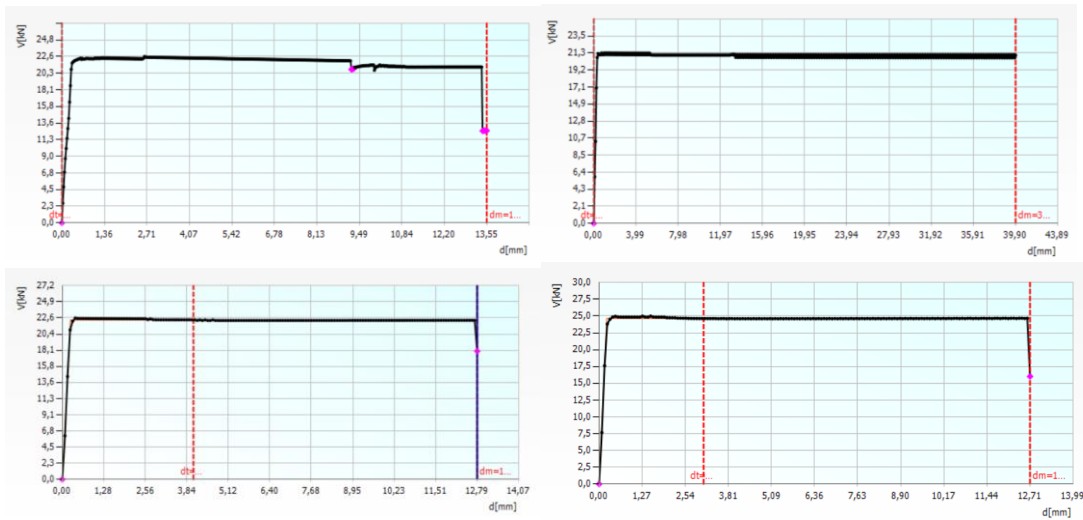
Figure 46: Pushover curve 3MURI Wall 9 (upper-left), Wall 10 (upper-right), Wall 11 (lower-left) and Wall 12 (lower-right)

In this section the results were given of the models in 3MURI. In the below figures the results are once again given, but categorized for each variation.
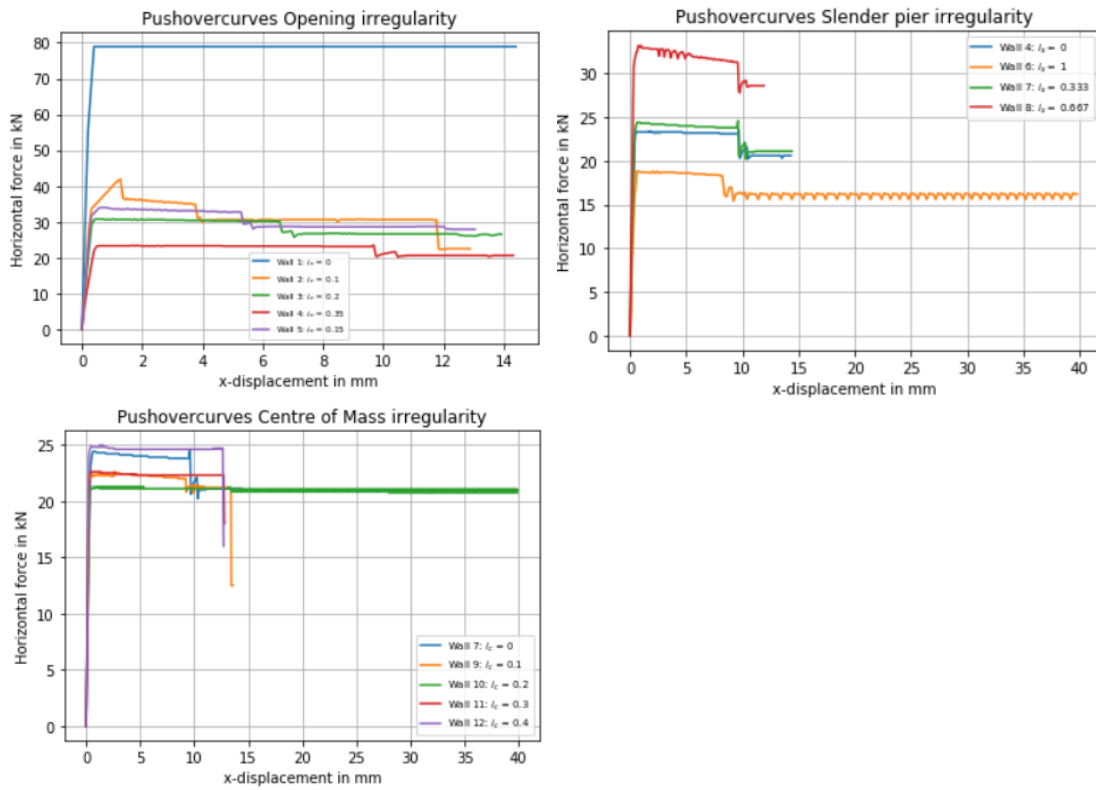
Figure 47: Pushovercurves 3MURI for each variation

4.2.5 Turnsek & Cakovic

Below the results are given for the Turnsek & Cakovic formula implemented in 3MURI for the left figures and the right figures show results of the Mohr-Coulob criterion:
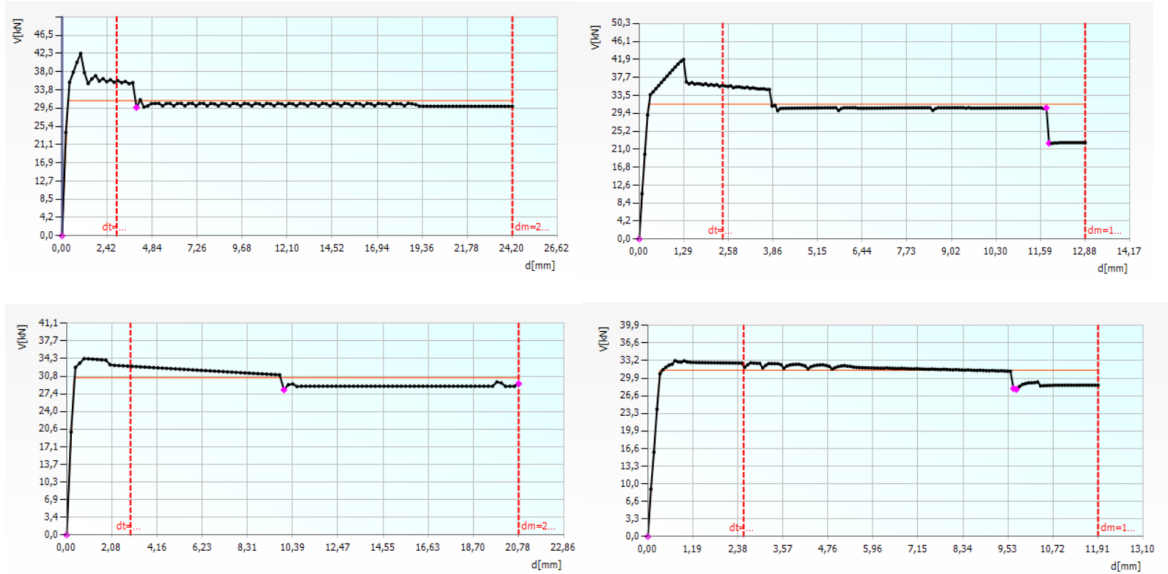
Figure 48: Results 3MURI Wall 2 (above) & Wall 8 (below).

4.2.6 NPR9998:2018 model parameters

Below the results are presented for two wall configurations in 3MURI with NPR9998:2018 model parameters implemented:
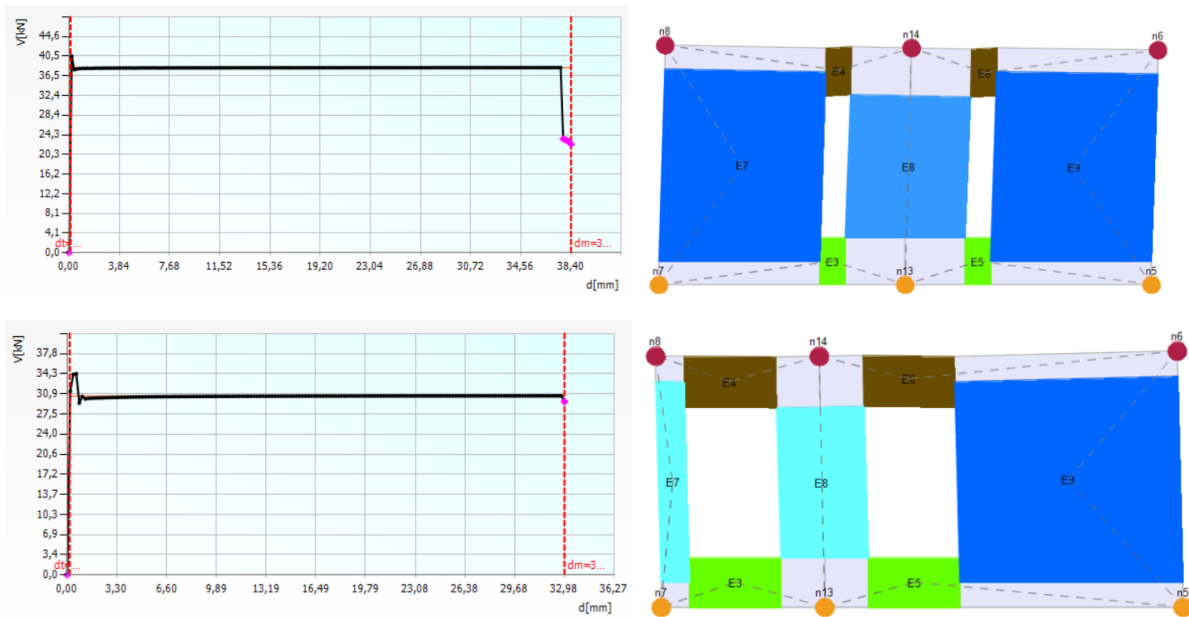
Figure 49: Results 3MURI Wall 2 (above) and Wall 12 (below).

4.3   SLaMA results

In this chapter the results of the SLaMA are presented. The results consist of the pushover curves and the observed failure mechanisms of each model.

4.3.1   Standard boundary condition formulation

In this chapter the results are based on the boundary conditions assessment of chapter 3.3.3.

4.3.1.1   Wall 1: Regular wall

In the table below the results are given of the individual pier:

	Shear capacity	Drift capacity	Failure mechanism
Pier 1	112.4 kN	20.4 mm	Shear
(Residual capacity)	87.2 kN		

Table 2: Results Wall 1

Below the pushover curve corresponding to wall 1 is presented:
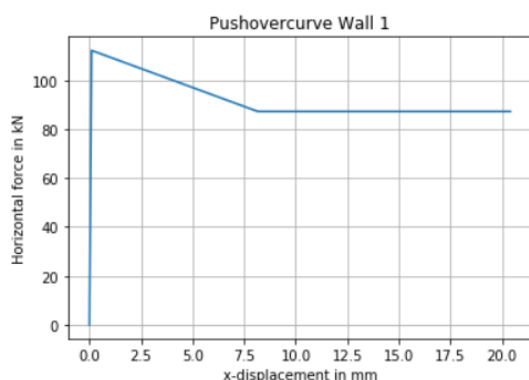
Figure 50: Pushover Curve SLaMA Wall 1

4.3.1.2   Wall 2-5: Opening irregularity

In the table below the results are given of the individual piers:

	Pier no.	Boundary conditions	Shear capacity (kN)	Drift capacity (mm)	Failure mechanism
Wall 2	Pier 1	Cantilever	14.2	32.7	Rocking
	Pier 2	Cantilever	9.4	24.5	Rocking
	Pier 3	Cantilever	14.2	32.6	Rocking
Wall 3	Pier 1	Cantilever	11.3	32.7	Rocking
	Pier 2	Cantilever	7.3	24.5	Rocking
	Pier 3	Cantilever	11.3	32.6	Rocking
Wall 4	Pier 1	Cantilever	7.5	32.7	Rocking
	Pier 2	Cantilever	4.9	24.5	Rocking
	Pier 3	Cantilever	7.5	32.6	Rocking
Wall 5	Pier 1	Cantilever	12.7	32.7	Rocking
	Pier 2	Cantilever	8.3	24.5	Rocking
	Pier 3	Cantilever	12.8	32.6	Rocking

Table 3: Results Walls 2-5

Below the pushover curve corresponding to wall 2 until 5 is presented:

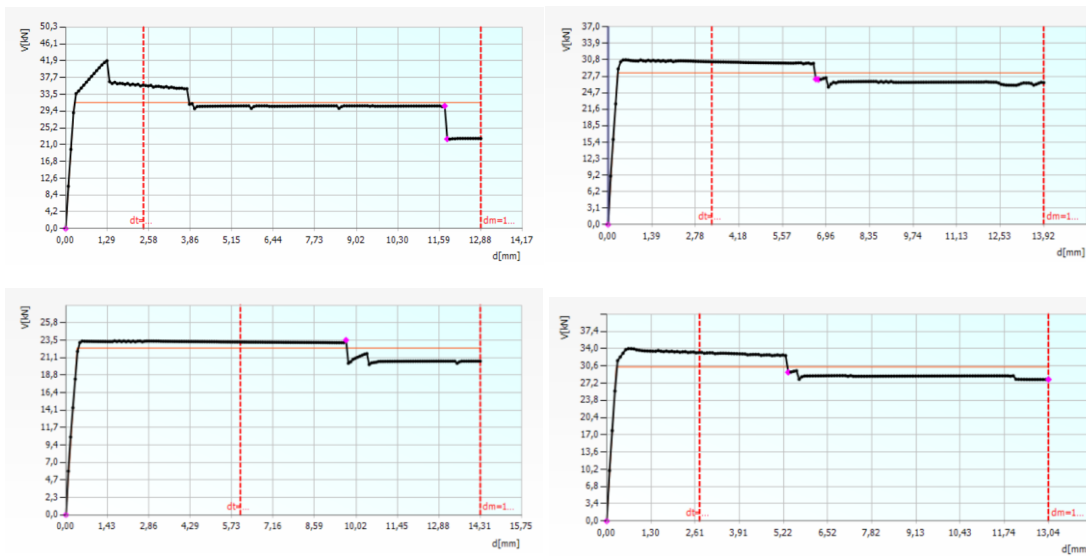*Figure 51: Pushover curve SLaMA Wall 2 (upper-left), Wall 3 (upper-right), Wall 4 (lower-left) and Wall 5 (lower-right)*

4.3.1.3   Wall 6-8: Slender pier irregularity

In the table below the results are given of the individual piers:

	Pier no.	Boundary conditions	Shear capacity (kN)	Drift capacity (mm)	Failure mechanism
Wall 6	Pier 1	Cantilever	4.6	32.7	Rocking
	Pier 2	Cantilever	3.1	24.5	Rocking
	Pier 3	Cantilever	3.1	24.5	Rocking
	Pier 4	Cantilever	4.6	32.6	Rocking
Wall 7	Pier 1	Cantilever	8.6	32.7	Rocking
	Pier 2	Cantilever	3.2	24.5	Rocking
	Pier 3	Cantilever	8.6	32.6	Rocking
Wall 8	Pier 1	Double-clamped	4	32.7	Rocking
	Pier 2	Cantilever	25.8	26.4	Shear
	Pier 3	Double-clamped	4	32.6	Rocking

Table 4: Results Walls 6-8

Below the pushover curve corresponding to wall 6 until 8 is presented:
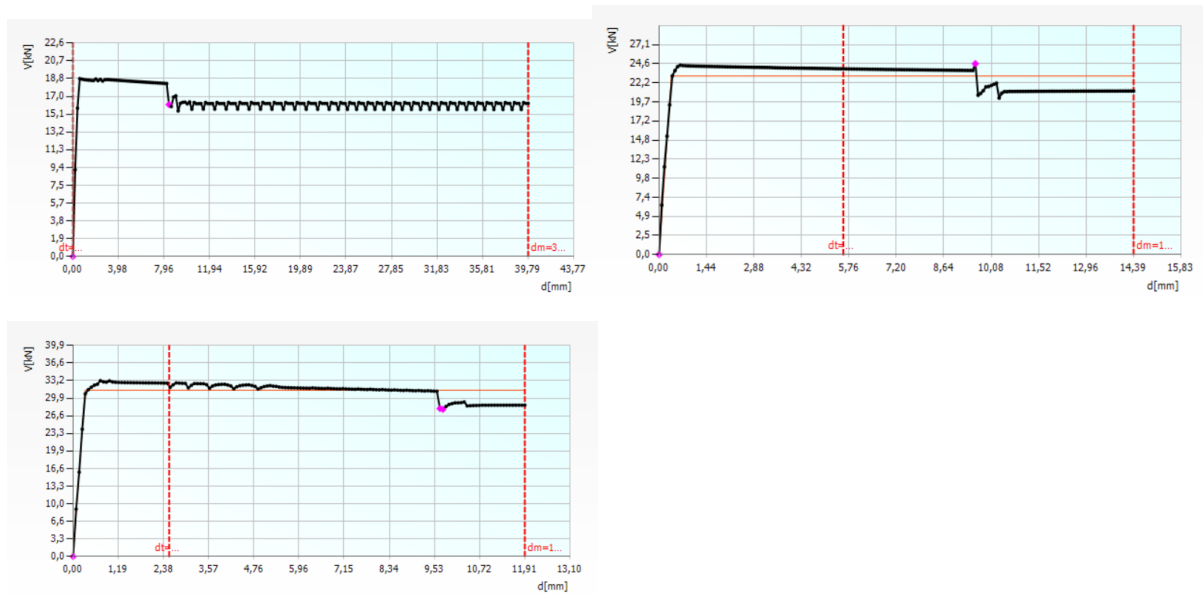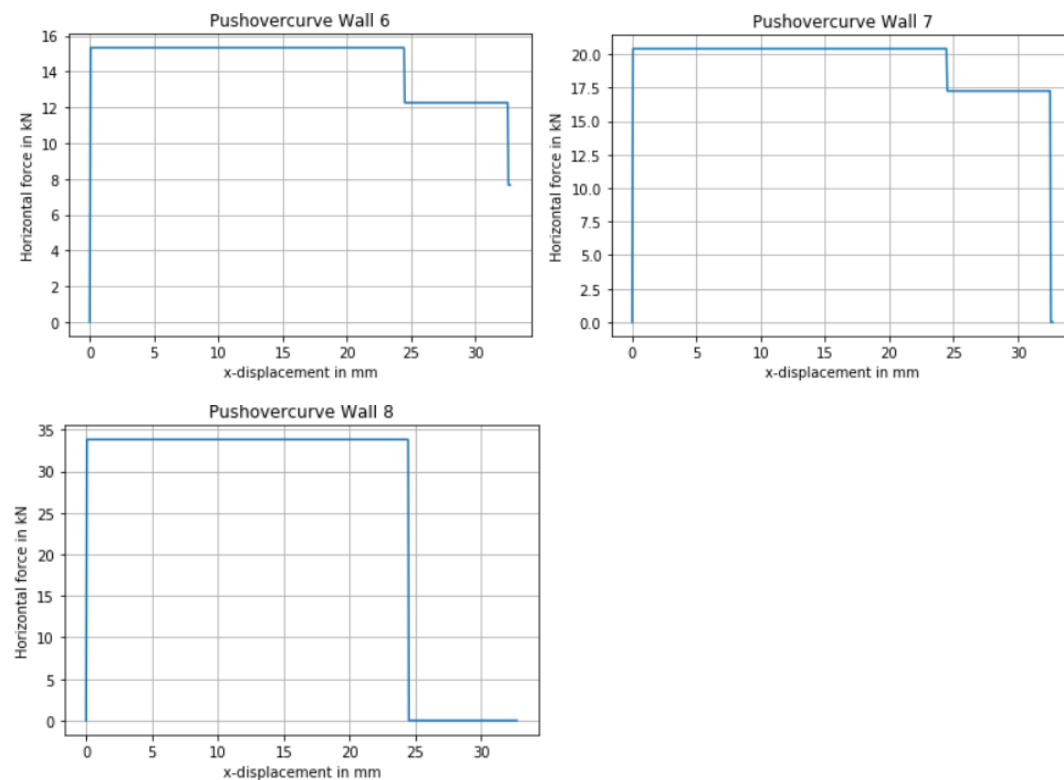

Figure 52: Pushover curve SLaMA Wall 6 (upper-left), Wall 7 (upper-right) and Wall 8 (lower-left).

4.3.1.4   Wall 9-12: Centre of mass irregularity

In the table below the results are given of the individual piers:

	Pier no.	Boundary conditions	Shear capacity (kN)	Drift capacity (mm)	Failure mechanism
Wall 9	Pier 1	Cantilever	6.7	32.7	Rocking
	Pier 2	Double-clamped	3.7	24.5	Rocking
	Pier 3	Cantilever	13.5	32.6	Rocking
Wall 10	Pier 1	Cantilever	2.7	40.8	Rocking
	Pier 2	Cantilever	5	39.7	Rocking
	Pier 3	Cantilever	14.4	33.6	Rocking
Wall 11	Pier 1	Double-clamped	2.8	32.7	Rocking
	Pier 2	Cantilever	4.4	24.5	Rocking
	Pier 3	Cantilever	19.3	31.2	Rocking
Wall 12	Pier 1	Double-clamped	0.8	32.7	Rocking
	Pier 2	Cantilever	4.4	24.5	Rocking
	Pier 3	Cantilever	24.4	29.4	Rocking

Table 5: Results Walls 9-12

Below the pushover curve corresponding to wall 9 until 12 is presented:
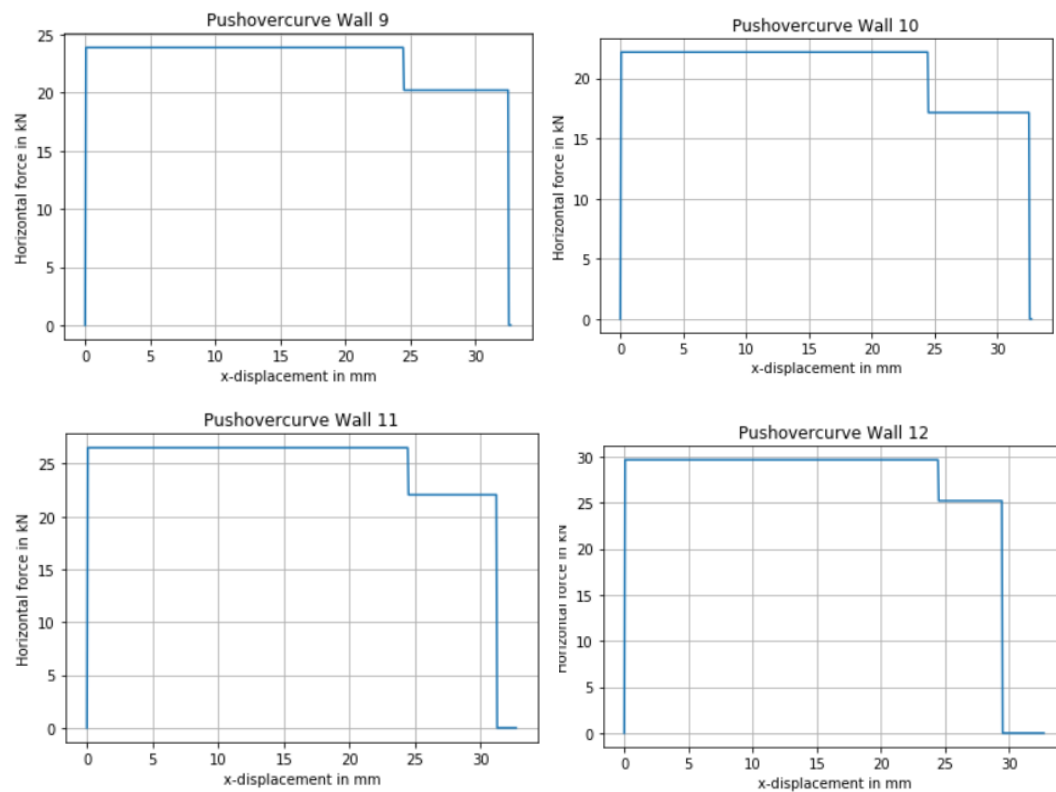
Figure 53: Pushover curve SLaMA Wall 9 (upper-left), Wall 10 (upper-right), Wall 11 (lower-left) and Wall 12 (lower-right)

In this section the results were given of the SLaMA based on the standard boundary condition formulation. In the below figures the results are once again given, but categorized for each variation.

Figure 54: Pushovercurves SLaMA standard boundary conditions formulation for each variation.

4.3.2 Linear interpolation of the boundary conditions

In this chapter

4.3.2.1 Wall 1: Regular wall

	Shear capacity	Drift capacity	Failure mechanism
Pier 1	112.4 kN	20.4 mm	Shear
(Residual capacity)	87.2 kN		

Table 6: Results Wall 1

Figure 55: Pushover Curve SLaMA Wall 1

4.3.2.2 Wall 2-5: Opening irregularity

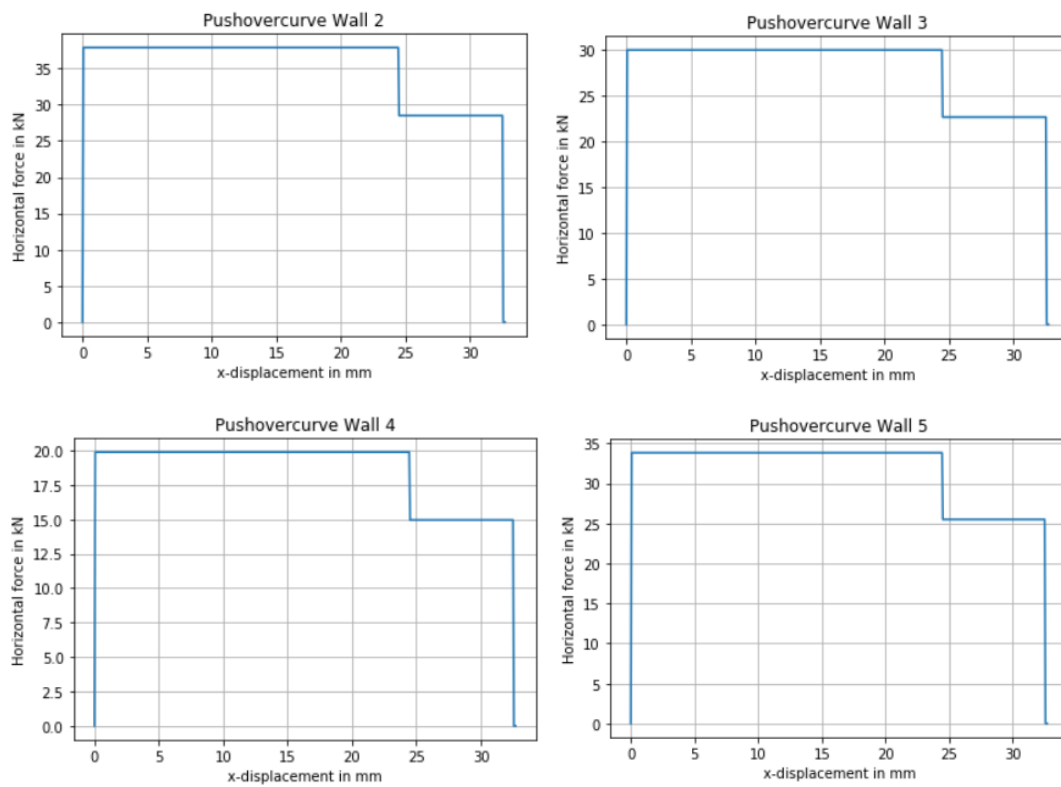|	*Pier no.*	*Boundary conditions*	*Shear capacity (kN)*	*Drift capacity (mm)*	*Failure mechanism*
Wall 2	Pier 1	0.96	14.7	32.7	Rocking
	Pier 2	0.93	10.1	24.5	Rocking
	Pier 3	0.96	14.8	32.6	Rocking
Wall 3	Pier 1	0.91	12.4	32.7	Rocking
	Pier 2	0.82	9.0	24.5	Rocking
	Pier 3	0.91	12.4	32.6	Rocking
Wall 4	Pier 1	0.86	8.7	32.7	Rocking
	Pier 2	0.72	6.9	24.5	Rocking
	Pier 3	0.86	8.7	32.6	Rocking
Wall 5	Pier 1	0.94	13.5	32.7	Rocking
	Pier 2	0.88	9.5	24.5	Rocking
	Pier 3	0.94	13.6	32.6	Rocking

Table 7: Results Walls 2-5

Figure 56: Pushover curve SLaMA Wall 2 (upper-left), Wall 3 (upper-right), Wall 4 (lower-left) and Wall 5 (lower-right)

4.3.2.3 Wall 6-8: Slender pier irregularity

	Pier no.	Boundary conditions	Shear capacity (kN)	Drift capacity (mm)	Failure mechanism
Wall 6	Pier 1	0.77	5.9	32.7	Rocking
	Pier 2	0.55	5.6	24.5	Rocking
	Pier 3	0.55	5.6	24.5	Rocking
	Pier 4	0.77	6.0	32.6	Rocking
Wall 7	Pier 1	0.88	9.8	32.7	Rocking
	Pier 2	0.56	5.7	24.5	Rocking
	Pier 3	0.88	9.8	32.6	Rocking
Wall 8	Pier 1	Double-clamped	4	32.7	Rocking
	Pier 2	0.94	27.4	24.5	Shear
	Pier 3	Double-clamped	4	32.6	Rocking

Table 8: Results Walls 6-8

Figure 57: Pushover curve SLaMA Wall 6 (upper-left), Wall 7 (upper-right) and Wall 8 (lower-left).

|	Pier no.	Boundary conditions	Shear capacity (kN)	Drift capacity (mm)	Failure mechanism
Wall 9	Pier 1	0.84	7.9	32.7	Rocking
	Pier 2	Double-clamped	3.7	24.5	Rocking
	Pier 3	0.92	14.6	32.6	Rocking
Wall 10	Pier 1	0.62	4.4	32.7	Rocking
	Pier 2	0.72	7.0	24.5	Rocking
	Pier 3	0.93	15.6	32.6	Rocking
Wall 11	Pier 1	Double-clamped	2.8	32.7	Rocking
	Pier 2	0.69	6.5	24.5	Rocking
	Pier 3	0.94	20.4	31.2	Rocking
Wall 12	Pier 1	Double-clamped	0.8	32.7	Rocking
	Pier 2	0.69	6.5	24.5	Rocking
	Pier 3	0.95	25.6	29.4	Rocking

Table 9: Results Walls 9-12

Figure 58: Pushover curve SLaMA Wall 9 (upper-left), Wall 10 (upper-right), Wall 11 (lower-left) and Wall 12 (lower-right)

In this section the results were given of the SLaMA based on linear interpolation of the boundary conditions. In the below figures the results are once again given, but categorized for each variation.
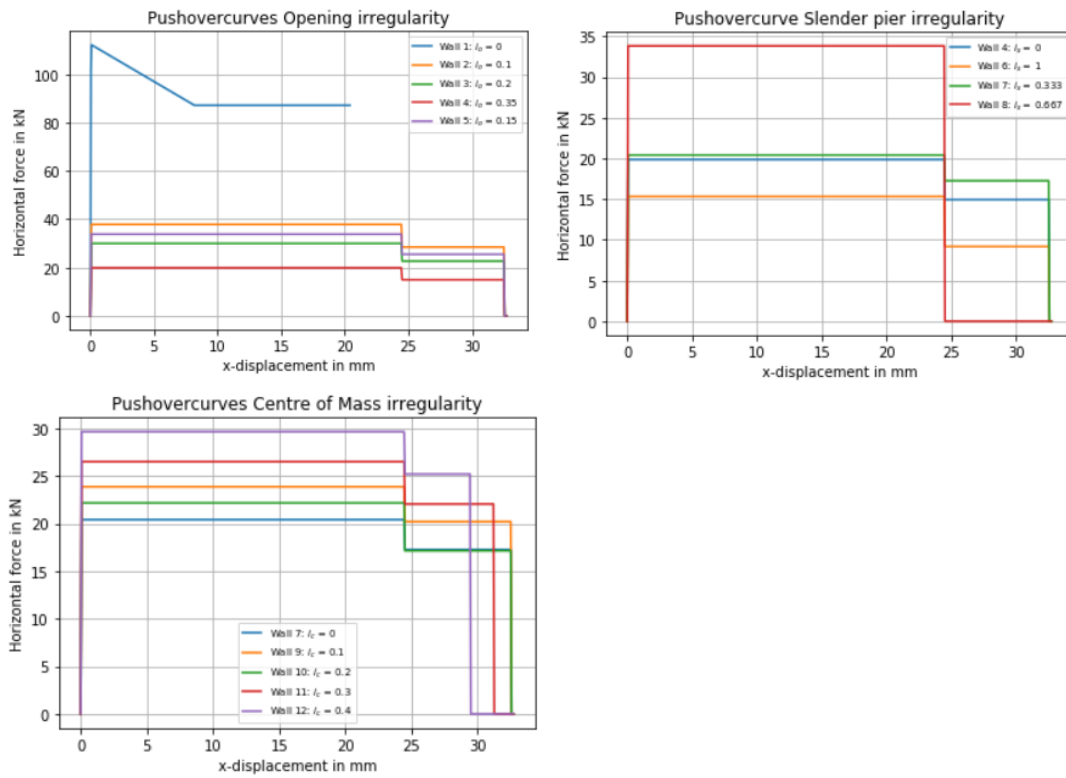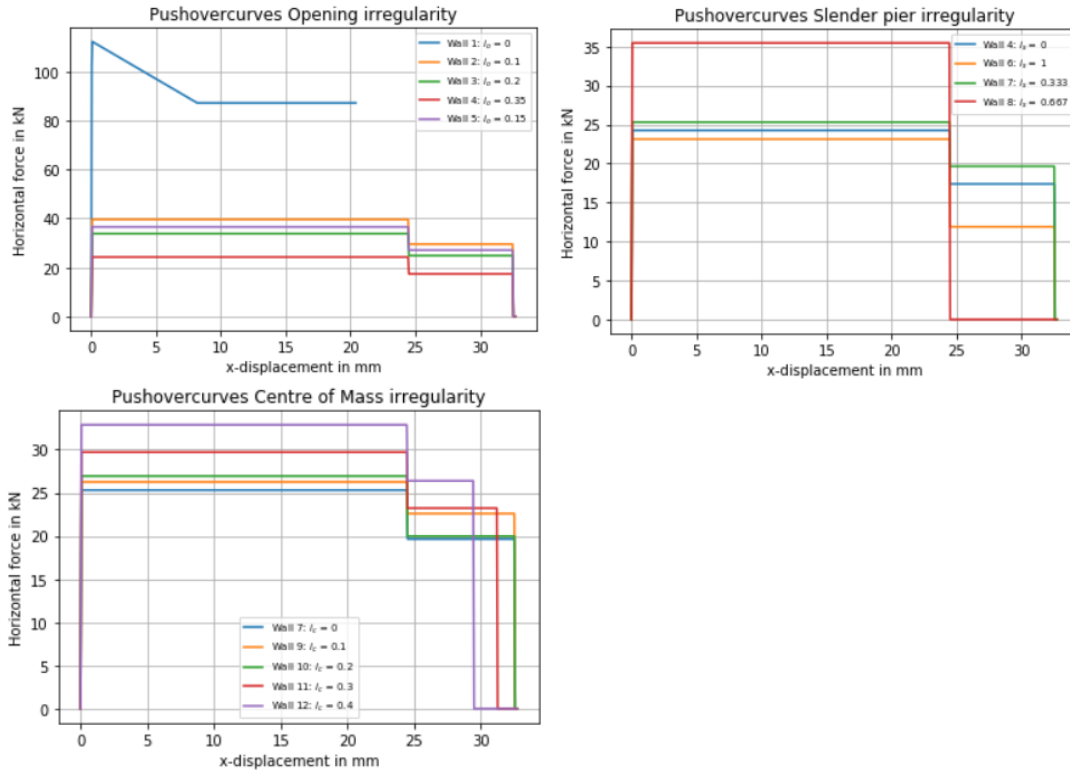

Figure 59: Pushovercurves SLaMA linear interpolation for each variation.

4.3.3 Boundary conditions based on MatrixFrame

4.3.3.1 Wall 1: Regular wall

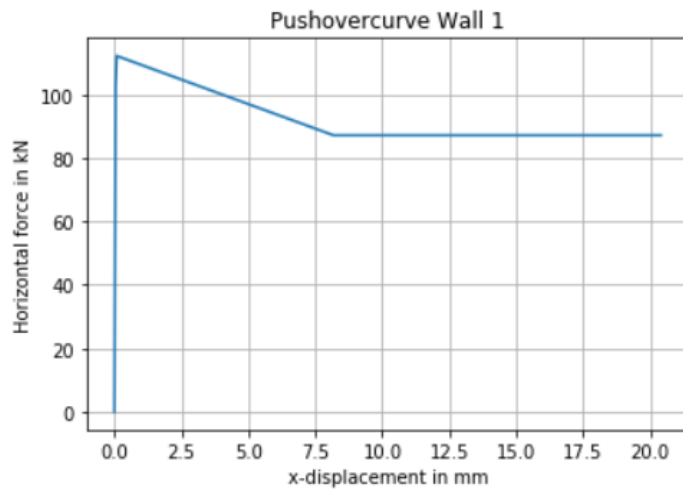|	Shear capacity	Drift capacity	Failure mechanism
Pier 1	112.4 kN	20.4 mm	Shear
(Residual capacity)	87.2 kN		

Table 10: Results Wall 1
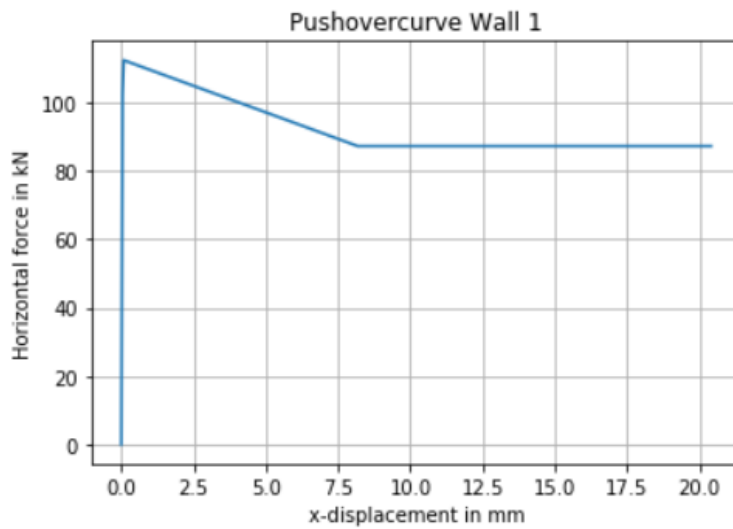
Figure 60: Pushover Curve SLaMA Wall 1

4.3.3.2 Wall 2-5: Opening irregularity

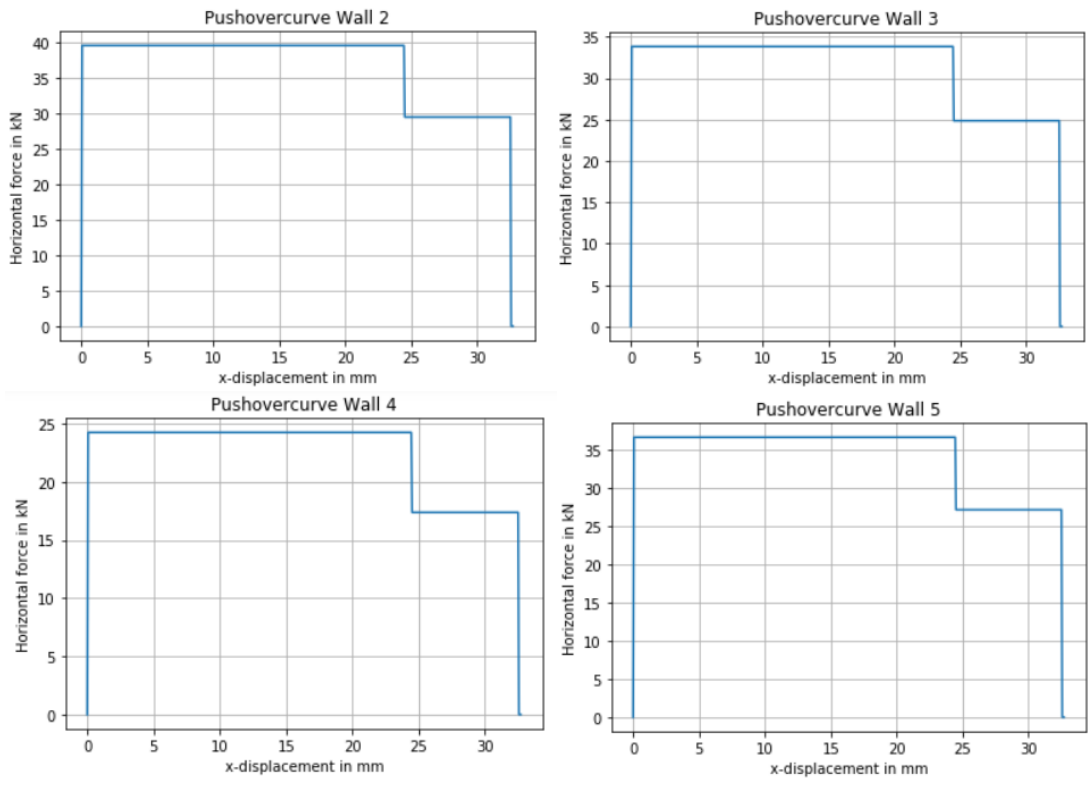|	Pier no.	Boundary conditions	Shear capacity (kN)	Drift capacity (mm)	Failure mechanism
Wall 2	Pier 1	0.98	14.5	32.7	Rocking
	Pier 2	0.98	9.6	24.5	Rocking
	Pier 3	0.99	14.4	32.6	Rocking
Wall 3	Pier 1	0.98	11.6	32.7	Rocking
	Pier 2	Cantilever	7.3	24.5	Rocking
	Pier 3	0.98	11.6	32.6	Rocking
Wall 4	Pier 1	0.97	7.7	32.7	Rocking
	Pier 2	Cantilever	4.9	24.5	Rocking
	Pier 3	0.97	7.7	32.6	Rocking
Wall 5	Pier 1	0.98	12.9	32.7	Rocking
	Pier 2	Cantilever	8.3	24.5	Rocking
	Pier 3	0.98	13.0	32.6	Rocking

Table 11: Results Walls 2-5
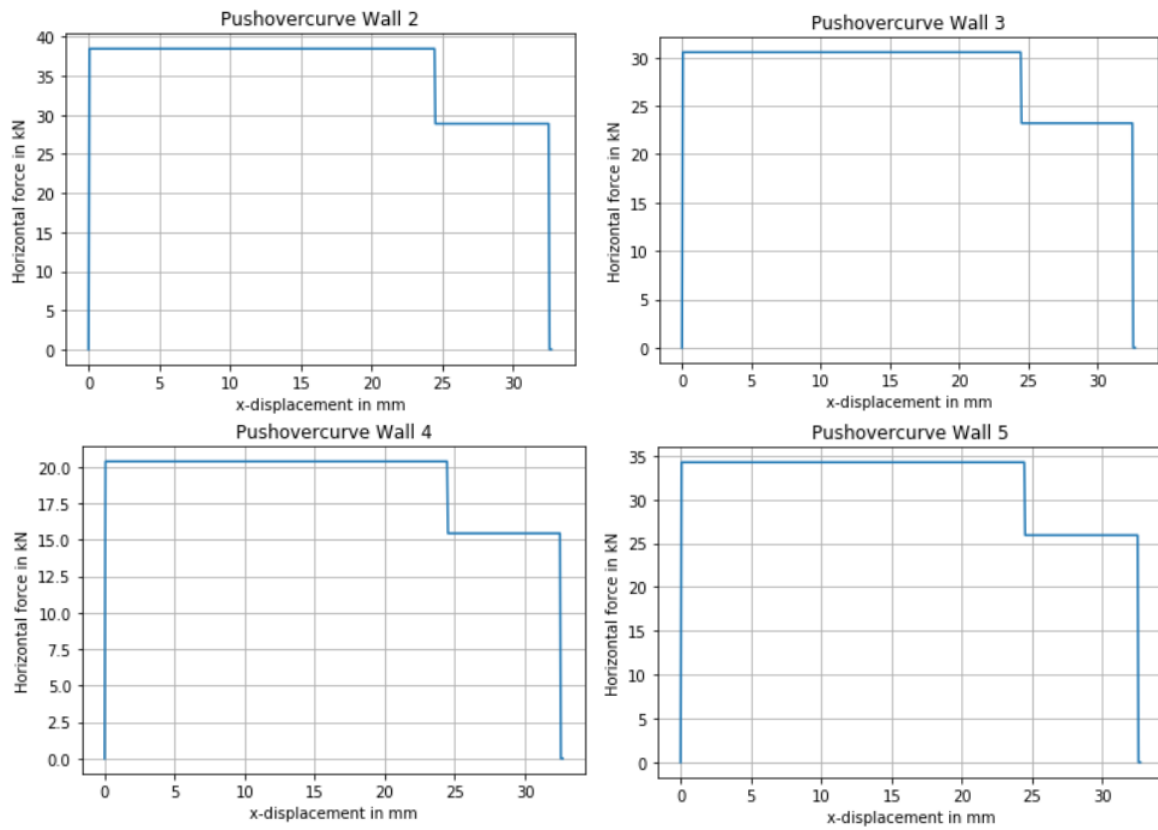
Figure 61: Pushover curve SLaMA Wall 2 (upper-left), Wall 3 (upper-right), Wall 4 (lower-left) and Wall 5 (lower-right)

4.3.3.3   Wall 6-8: Slender pier irregularity

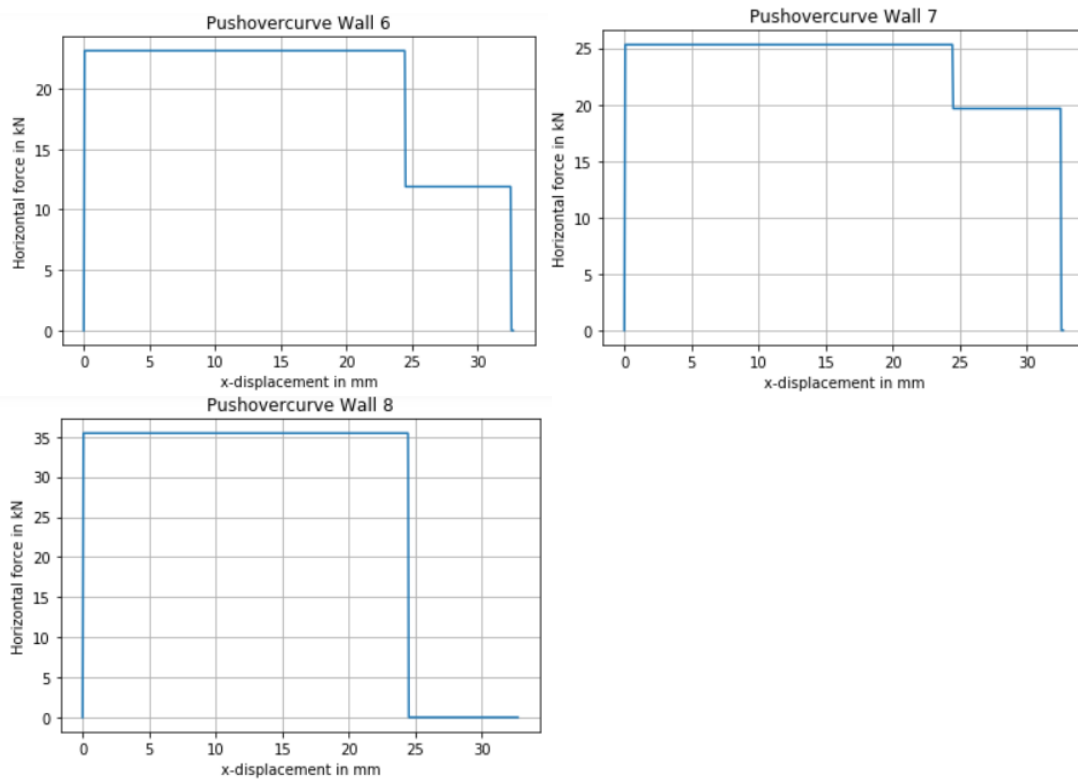|	Pier no.	Boundary conditions	Shear capacity (kN)	Drift capacity (mm)	Failure mechanism
Wall 6	Pier 1	0.93	4.9	32.7	Rocking
	Pier 2	0.95	3.3	24.5	Rocking
	Pier 3	0.95	3.3	24.5	Rocking
	Pier 4	0.93	4.9	32.6	Rocking
Wall 7	Pier 1	0.97	8.9	32.7	Rocking
	Pier 2	Cantilever	3.2	24.5	Rocking
	Pier 3	0.97	8.9	32.6	Rocking
Wall 8	Pier 1	0.93	2.2	32.7	Rocking
	Pier 2	Cantilever	25.8	26.4	Shear
	Pier 3	0.93	2.2	32.6	Rocking

Table 12: Results Walls 6-8
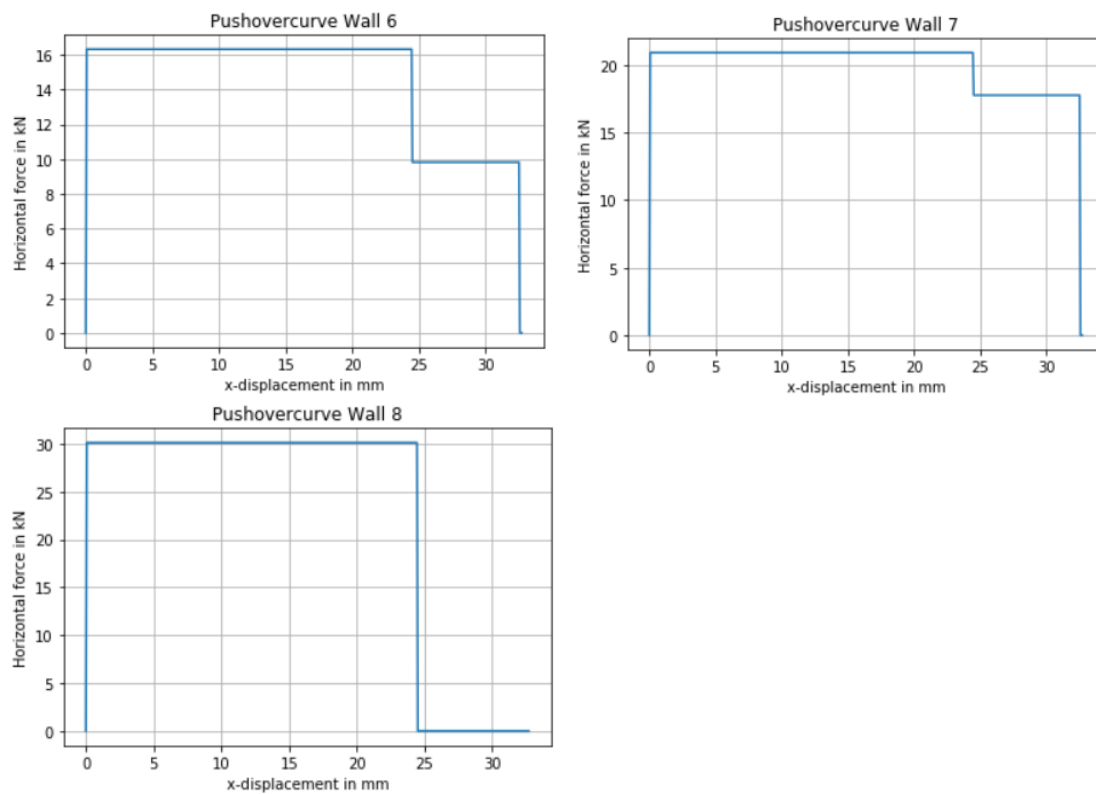
Figure 62: Pushover curve SLaMA Wall 6 (upper-left), Wall 7 (upper-right) and Wall 8 (lower-left).

4.3.3.4 Wall 9-12: Centre of mass irregularity

	Pier no.	Boundary conditions	Shear capacity (kN)	Drift capacity (mm)	Failure mechanism
Wall 9	Pier 1	0.96	7.0	32.7	Rocking
	Pier 2	0.98	1.9	24.5	Rocking
	Pier 3	0.83	16.3	32.6	Rocking
Wall 10	Pier 1	0.92	3.0	32.7	Rocking
	Pier 2	0.99	5.1	24.5	Rocking
	Pier 3	0.99	14.6	32.6	Rocking
Wall 11	Pier 1	0.88	1.6	32.7	Rocking
	Pier 2	0.98	4.6	24.5	Rocking
	Pier 3	Cantilever	19.3	31.2	Rocking
Wall 12	Pier 1	0.90	0.4	32.7	Rocking
	Pier 2	0.96	4.6	24.5	Rocking
	Pier 3	0.99	24.5	29.4	Rocking

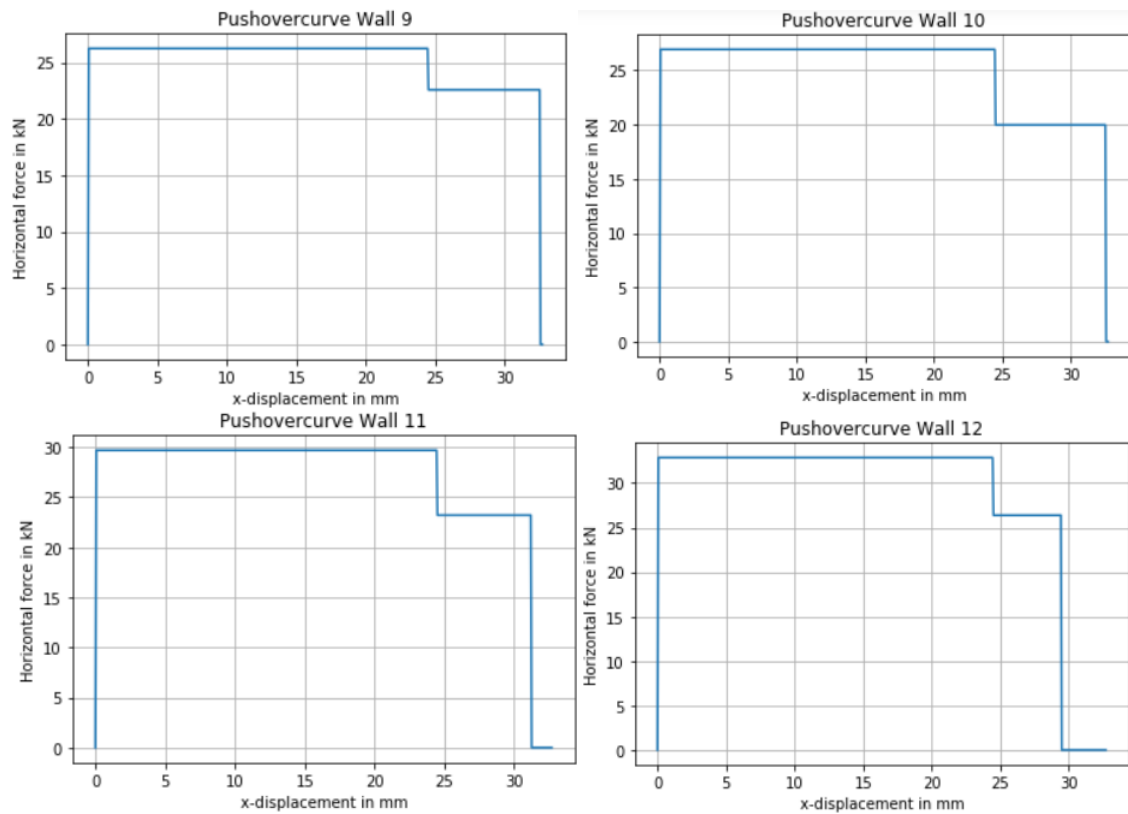Table 13: Results Walls 9-12

Figure 63: Pushover curve SLaMA Wall 9 (upper-left), Wall 10 (upper-right), Wall 11 (lower-left) and Wall 12 (lower-right)

Summary

In this section the results were given of the SLaMA based on MatrixFrame. In the below figures the results are once again given, but categorized for each variation.
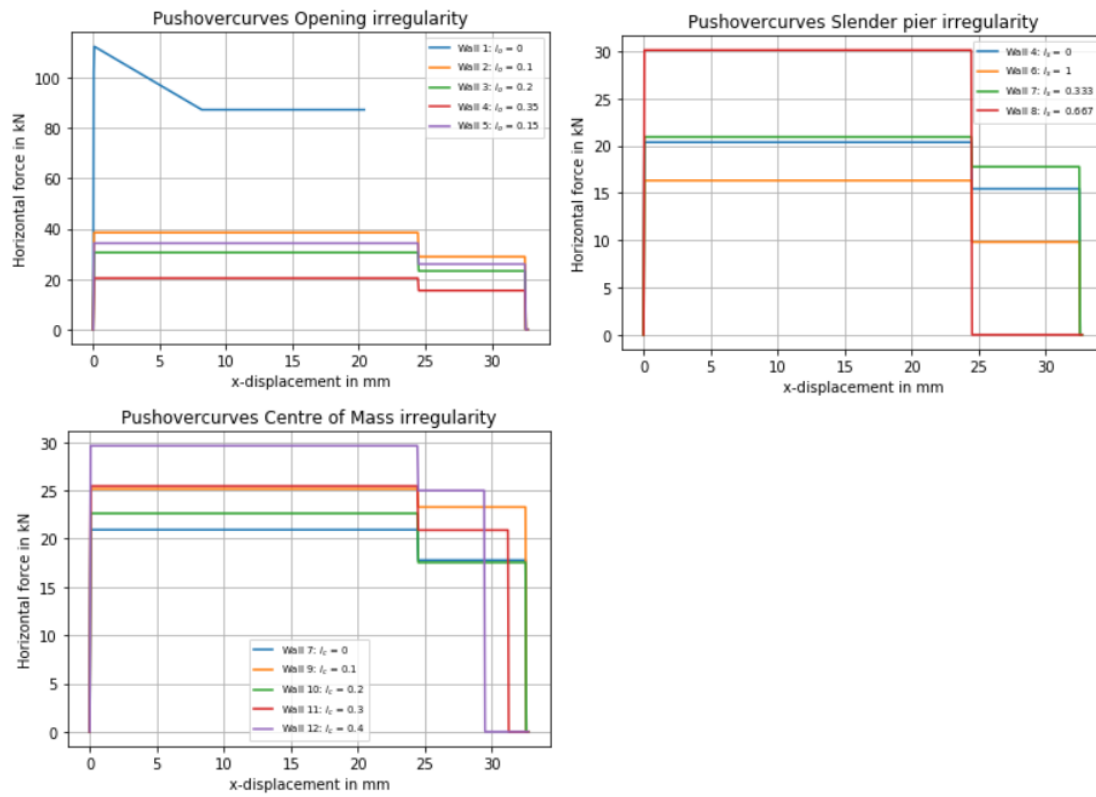
Figure 64: Pushovercurves SLaMA based on MatrixFrame for each variation.

5 Discussion

This chapter covers the comparison of the results acquired in the previous chapter. The comparison is split into several parts. First the formulation of the boundary conditions in 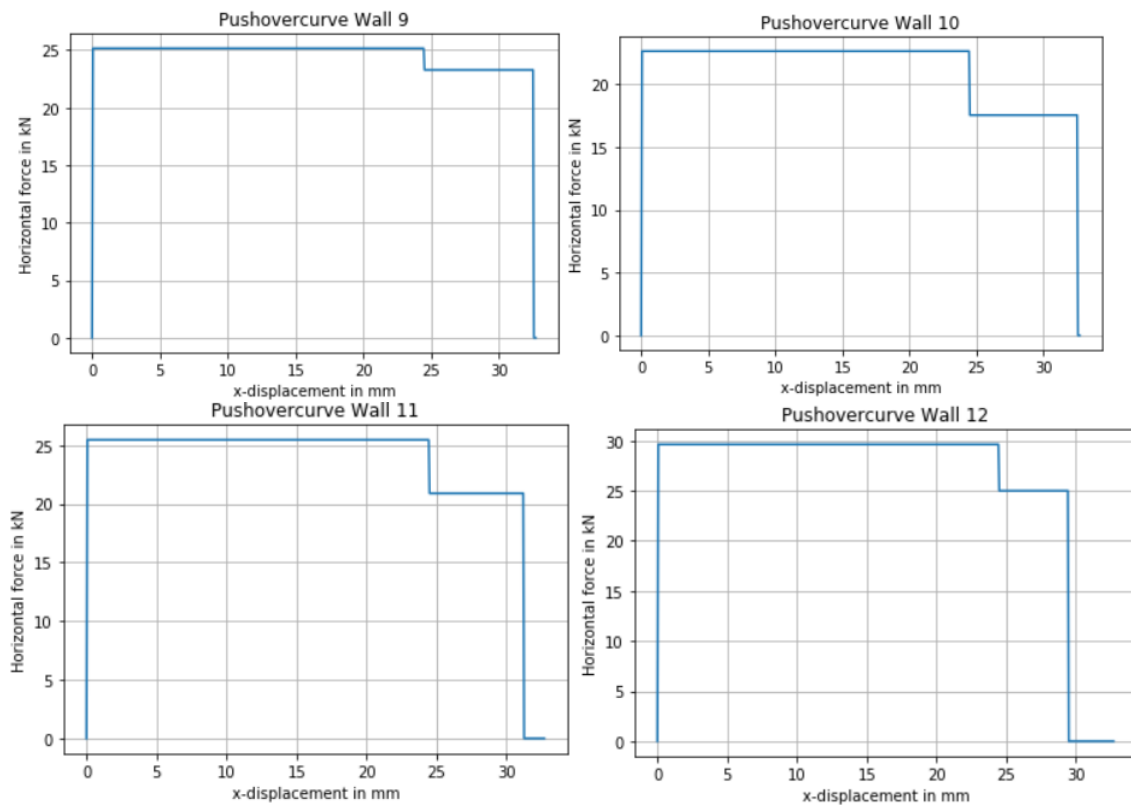SLaMA will be discussed. Then the results will be compared with each other by presenting the difference between the simplified calculation methods (SLaMA and 3MURI EFM) and DIANA FEA. Then the differences will be discussed and elaborated.

5.1 Comparison of the results in terms of base shear

In the below tables the results of the different methods are given for each irregularity index. The SLaMA results with the new formulations of the boundary conditions is also given below.

Model	i_o	DIANA	SLaMA	3MURI	Ratio SLaMA	Ratio SLaMA Linear	Ratio SLaMA Frame	Ratio 3MURI
Wall 1	0	116	87.2	80	0.75	0.75	0.75	0.69
Wall 2	0.1	79.7	37.9	31.5	0.48	0.5	0.48	0.4
Wall 5	0.15	75.7	33.8	30.4	0.45	0.48	0.45	0.4
Wall 3	0.2	73	30	28.4	0.41	0.46	0.42	0.39
Wall 4	0.35	59.9	19.9	22.5	0.33	0.4	0.34	0.38

Table 14: Comparison of the base shear values obtained at varying the opening irregularity

Model	i_o	i_s	DIANA	SLaMA	3MURI	Ratio SLaMA	Ratio SLaMA Linear	Ratio SLaMA Frame	Ratio 3MURI
Wall 4	0.35	0	59.9	19.9	22.5	0.33	0.4	0.34	0.38
Wall 7	0.35	0.333	59.3	20.4	23	0.34	0.43	0.35	0.39
Wall 8	0.35	0.667	70	33.8	31.3	0.48	0.51	0.43	0.45
Wall 6	0.35	1	44.5	15.3	17	0.34	0.52	0.37	0.38

Table 15: Comparison results slender pier irregularity

Model	i_o	i_s	i_c	DIANA	SLaMA	3MURI	Ratio SLaMA	Ratio SLaMA Linear	Ratio SLaMA Frame	Ratio 3MURI
Wall 7	0.35	0.333	0	59.3	20.4	23	0.34	0.43	0.35	0.39
Wall 9	0.35	0.333	0.1	57.5	23.9	22.3	0.41	0.46	0.44	0.39
Wall 10	0.35	0.333	0.2	54.5	22.2	21.1	0.41	0.49	0.42	0.39
Wall 11	0.35	0.333	0.3	56.9	26.5	22.6	0.47	0.52	0.45	0.4
Wall 12	0.35	0.333	0.4	58	29.6	24.6	0.51	0.57	0.51	0.42

Table 16: Comparison results centre of mass irregularity

5.1.1   Opening irregularity

For the first irregularity, the models differed in the sizes of the openings. For all methods it can be noticed in the figure below that the shear capacity undergoes a large drop for even the slightest opening. In FEM the opening causes a disturbance in the stress field, which causes the stresses in plane to increase and in return will cause the wall to fail at an earlier stage. For the simplified methods, the opening influences the definition of the pier and spandrel geometry and in return causes in a simplified way a decrease in the shear capacity. Beyond the first opening irregularity, the lateral capacity decreases further with the increase of the opening irregularity index. However, the shear capacity decreases for each method differently.

For the EFM in 3MURI, the difference with respect to the results obtained with DIANA FEA remains constant for the different values of the index i_0. This can be observed in the figure below. The first drop is due to the disturbance caused by adding an opening in a wall façade. This first decrease is for all simplified methods large and can be related to the transition of the wall configurations from a single pier to three piers. When multiple piers are present in a wall façade, the influence of the force redistribution on the seismic capacity plays a more significant role. EFM makes use of the frame approach to redistribute forces while SLaMA does not take into account the force redistribution of the piers during loading. This can lead to more conservative results than DIANA. The parallel course of the lateral capacities in EFM and FEM is due to the similar assumptions been made. 3MURI takes into account the change of the axial load during lateral loading just like DIANA. However, this research focuses on single floor wall configurations only. If a wall has multiple floors, other irregularities could play a larger role in the difference, like the definition of a pier and a spandrel. As far as the underestimation of 3MURI compared to SLaMA concerned, the model parameters used in 3MURI are based on the Eurocode NL, while the SLaMA calculation is in correspondence with NPR9998:2018. 3MURI has also the option to adjust model parameters in correspondence with the NPR9998. This has been done for two wall configurations in chapter 4.3.6. The results of these models are similar to the SLaMA as to the force and displacement capacity concerned.

For SLaMA, the first result does not differ much from the FEM results. At the first irregularity index of 0.1, the drop is very large and after that the difference only becomes larger between SLaMA and DIANA. The SLaMA results are initially closer to DIANA than 3MURI, but eventually, as the opening size increases, the SLaMA method underestimates the ultimate loading capacity compared to DIANA. This underestimation can be caused by several factors. One of these factors could be the formulation of the boundary conditions in the SLaMA. The SLaMA method takes a psi equal to 0.5 for double-clamped condition and a psi equal to 1 for cantilever boundary conditions. In reality, these boundary conditions do not occur that often, because a pier is always connected to a spandrel and the connection between pier and spandrel is often neither infinitely rigid nor hinged. For the cases studied in the figure below, the SLaMA method gave for all five walls piers with cantilever boundary conditions. This, while the opening irregularity index was increasing. For a larger opening irregularity, the piers increase in slenderness. This means in reality that the connection becomes more rigid between piers and spandrels. So the underestimation is caused because SLaMA assumes cantilever boundary conditions for all the 5 walls, while in reality the piers should behave more rigidly.

As a solution for this underestimation, a new formulation for the boundary conditions is made. These two formulations have been explained in chapter 5.1. In the figure below one can see that the shear capacity differs less from DIANA with implementing the linear interpolation formulation in SLaMA. The method is now also less dependent of the opening irregularity index. The second formulation gives results similar to the initial boundary condition formulation. This means that most piers in the wall configurations act close to cantilever and so the difference with the assessment approach in 3.3.3 is small. This approach can also be verified in 3MURI. In 3MURI it can be observed that the spandrels crack first in a wall, which causes the close to cantilever condition. Overall, the variations of the SLaMA and especially EFM results compared to DIANA are limited with respect to the opening irregularity.
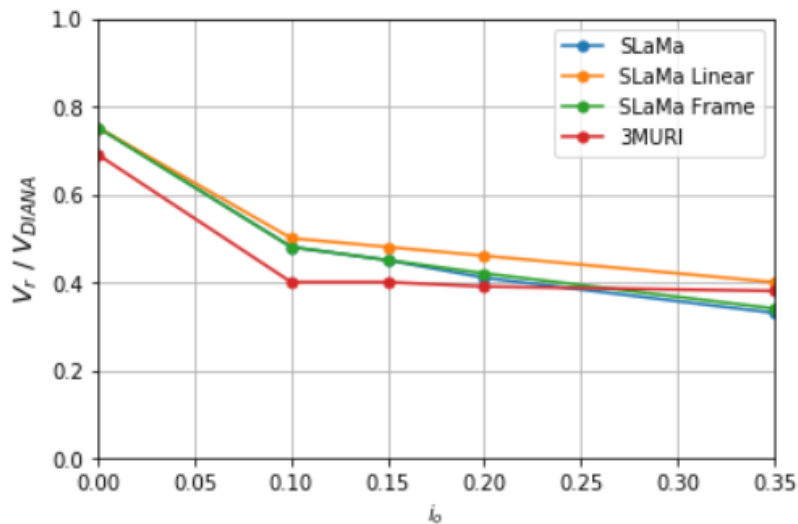

Figure 65: Comparison results opening irregularity

5.1.2   Slender pier irregularity

The second irregularity index is based on the slenderness of the piers. For each wall the number of slender piers has been increased. For the EFM results there is no significant change in the ratio for all the walls except wall 8. This can be caused because of shear failure of the middle pier in the wall façade. The shear failure is based on the Mohr-Coulomb criterion while in case of rocking failure other formulas are used.

The SLaMA results also do not show significant changes except for wall 8. Also, for SLaMA the same applies. Failure due to shear is also based on the Mohr-Coulomb criterion and gives different results than for rocking failure. What also can be noticed is the underestimation of the SLaMA results. It should be noted that opening irregularity index for all the four walls is equal to 0.35. Which is significant for the underestimation of the results as seen in the previous figure. Again implementing the linear interpolation formulation of the boundary conditions gives lower differences with DIANA. For the frame formulation, one can observe that the variation of the results compared to DIANA is smaller. This is due to the boundary conditions in wall 8. With the assessment approach of 3.3.3 the boundary conditions for the two outer piers are double clamped. This causes the large difference in the figure below. The SLaMA Frame formulation shows a smaller variation that corresponds more with EFM. Again it can be observed that the variations of the simplified methods are limited.
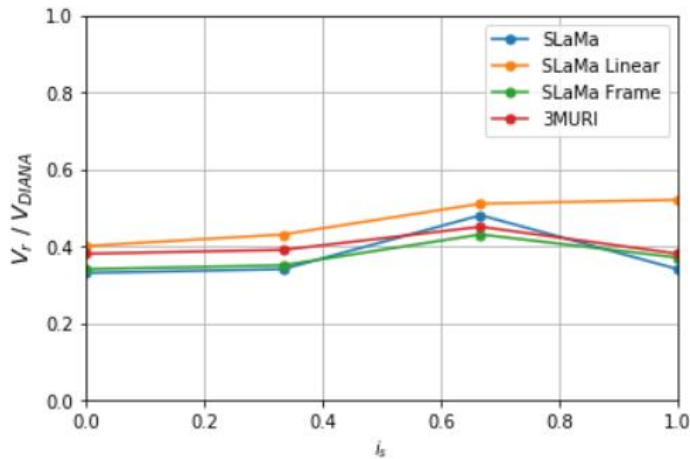
Figure 66: Comparison results slender pier irregularity

The formulation of the slender pier irregularity could be altered. Because a slenderness ratio of 2 is not always the definition of a slender pier in reality when observing the behaviour of a pier. The walls that have been assessed with the slender pier irregularity, may have had a slenderness ratio lower than two but still had rocking behaviour. This behaviour is typical for a slender pier and not for a thick pier. After taking a closer look at which slenderness ratio rocking behaviour will initiate, it can be concluded that it is not possible to determine such a slenderness ratio easily. This is because slender behaviour of a pier also depends on the boundary conditions, axial force and material properties. For Clay-brick pre 1945 an approximation is made of when a pier is slender:

$$\frac{hp}{lp} \geq \frac{0.81}{\psi}$$

This statement is inaccurate for very large axial loads. Applying this condition on the piers in this report gives a definition in correspondence with the behaviour of the pier in SLaMA. Piers with a slenderness lower than the above condition fail due to shear and piers higher than the condition fail due to rocking.

5.1.3 Centre of mass irregularity

The last irregularity index is based on the position of the piers relative to the centre of mass of the wall. This is a straightforward way to define the geometrical irregularity as far as asymmetry is concerned. Again for the EFM results there are no substantial differences relatively.

The SLaMA method shows changes compared to the FEM results from 0.34 to 0.51. By implementing the linear interpolation formulation of the boundary conditions, it can be observed that the results of SLaMA change substantially less than before. It can also be said that the results of SLaMA with the linear interpolation boundary condition formulation come for all indices closer to the FEM results than 3MURI. This is not necessarily because the formulation is better, because the SLaMA Linear formulation still varies depending on the irregularities in the wall. The SLaMA Frame formulation shows for all wall configuration results similar to the initial assessment approach. However, implementing the formulation gives results less dependent on the irregularities in a wall.
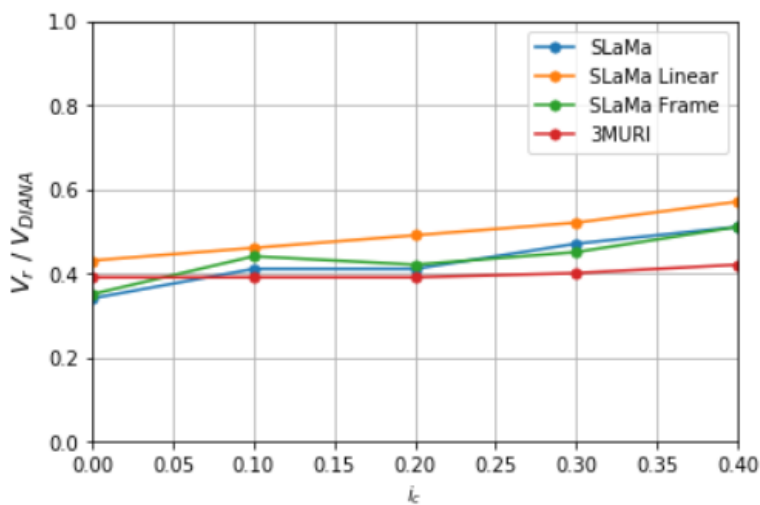

Figure 67: Comparison results centre of mass irregularity

The EFM in 3MURI shows results similar to the SLaMA method, however less dependent on geometrical irregularities for single floor 2D wall configurations. This could be due to the assessment of the boundary conditions, as can be seen in the SLaMA Frame formulation. However, one factor that plays a major role for the independence on geometrical irregularities in 3MURI is taking into account the change of axial load during lateral loading. The SLaMA does not take this change into account and assumes the initial axial load to be the final axial load. Further research about the effect of the varying axial load on the in-plane behaviour can be found in the research of Nidal Ennali. The variations for this irregularity are also very limited for SLaMA and especially EFM.

5.1.4 Influence of the new boundary conditions formulation

Based on the comparison of the results in section 5.1, one can see whether the two proposed assessment methods of the boundary conditions improve the accuracy of SLaMA. The linear interpolation formulation gives results closer to DIANA. An improvement between 0.02 and 0.18 can be seen for all wall configurations. The Matrix Frame approach does not show significant improvement of the results and even presents for some wall configurations results further away from DIANA than the initial method.

5.2   Failure mechanisms

For the different calculation methods the following failure mechanisms were observed:

Model	DIANA	SLaMA	3MURI	Comparison SLaMA-DIANA	Comparison 3MURI-DIANA
Wall 1	Shear failure	Bed joint sliding shear	Shear failure	Good agreement	Good agreement
Wall 2	Shear/rocking failure pier 3	Rocking of all the piers	Shear failure all piers	Reasonable agreement	Poor agreement
Wall 3	Shear/rocking failure pier 3	Rocking of all the piers	Shear failure pier 3	Reasonable agreement	Reasonable agreement
Wall 4	Shear/rocking failure pier 3	Rocking of all the piers	Shear failure pier 3	Reasonable agreement	Reasonable agreement
Wall 5	Shear/rocking failure pier 3	Rocking of all the piers	Shear failure pier 1 and 3	Reasonable agreement	Reasonable agreement
Wall 6	Rocking of all the piers	Rocking of all the piers	Shear failure pier 4	Good agreement	Reasonable agreement
Wall 7	Rocking/shear failure pier 3	Rocking of all the piers	Shear failure pier 3	Reasonable agreement	Reasonable agreement
Wall 8	Shear failure pier 2	Shear failure pier 2	Shear failure pier 2	Good agreement	Good agreement
Wall 9	Rocking/shear failure pier 1	Rocking of all the piers	Shear failure pier 1	Reasonable agreement	Reasonable agreement
Wall 10	Rocking of all the piers	Rocking of all the piers	Rocking of all the piers	Good agreement	Good agreement
Wall 11	Rocking of all the piers	Rocking of all the piers	Shear failure pier 3	Good agreement	Reasonable agreement
Wall 12	Rocking of all the piers	Rocking of all the piers	Shear failure pier 3	Good agreement	Reasonable agreement

Table 17: Failure mechanisms wall configurations

The failure mechanisms described by SLaMA show good correspondence with DIANA. However, SLaMA and EFM cannot define a combined failure mechanism as DIANA does. This makes it more difficult to visualise which failure mechanism is the governing one in DIANA. Another remark, that needs to be made is the use of the failure type 'Tensile strength head-joint defined by bed-joint frictional shear stress'. This failure gives a less accurate representation of the diagonal cracks occurring in a wall. This makes it even more difficult to get an accurate governing failure mechanism. Even though 3MURI shows a less correspondence with DIANA, based on the above argument this does not mean 3MURI is less accurate.

The SLaMA method shows mainly flexural failure mechanisms. This can be caused by not taking into account the varying axial load during loading. Based on the loading direction, the axial load will decrease during loading for the first pier and increase for the last pier. An increase in axial load could cause shear failure as a governing failure mechanism. The below figure shows an example of how the axial load can vary during loading.
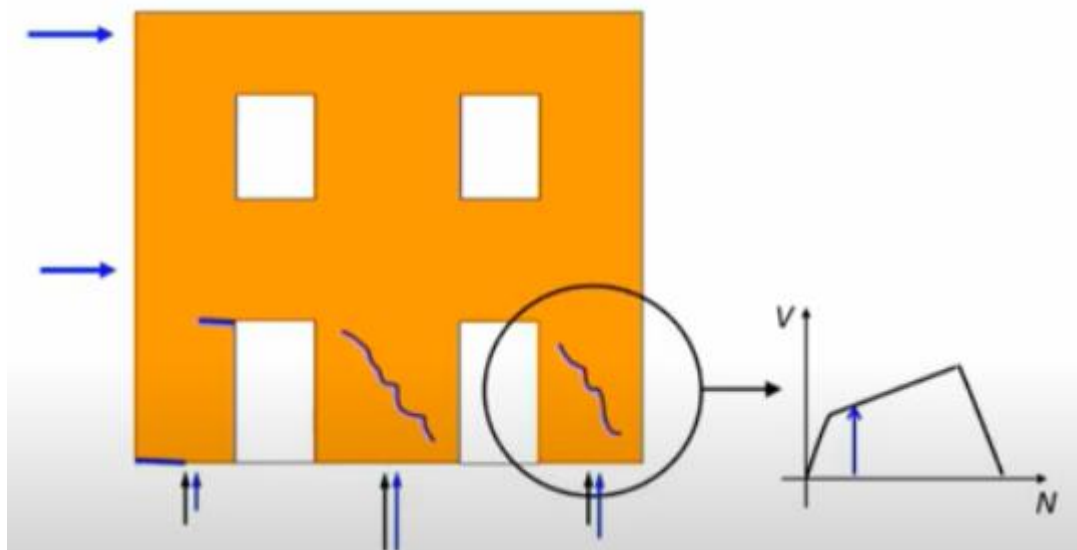

Figure 68: Varying axial load (3MURI, 2019)

5.3 Ultimate displacement capacity

The drift limit results were different for all methods. SLaMA gave drift limits between 24-32 mm, while 3MURI presented drift limits between 12-18 mm. DIANA presented displacement capacities larger than 40 mm. The differences are caused by the different relationships used for the drift limits. The displacement capacity of DIANA is based on the material model, while SLaMA and 3MURI base their results on empirical relationships of respectively the NPR and Eurocode NL. The large difference between SLaMA and 3MURI is mainly caused by the prediction of different failure mechanisms. Shear failure mechanisms cause in general lower displacement capacities than flexural failure mechanisms. In the table below the drift limits are shown:

Model	3MURI drift limit(mm)	SLaMA drift limit(mm)
Wall 1	14.4	20.4
Wall 2	12.9	32.6
Wall 3	13.9	32.6
Wall 4	14.3	32.6
Wall 5	13	32.6
Wall 6	39.8	32.6
Wall 7	14.4	32.6
Wall 8	11.9	24.5
Wall 9	13.6	32.6
Wall 10	39.9	32.6
Wall 11	12.8	31.2
Wall 12	12.7	29.4

Table 18: Drift limits 3MURI and SLaMA

5.4 Influence of the different constitutive models in 3MURI and DIANA

This research focuses on the influence of the geometrical irregularities on the simplified calculation methods as regards the in-plane behaviour of masonry wall façades compared to FEM. For the FEM analysis, DIANA FEA was used. The comparisons have been done with one specific constitutive model in DIANA and 3MURI. For the modelling in DIANA, the Engineering Masonry Model was used. Using other constitutive models in DIANA could of course give different results for the in-plane behaviour and there is not one specific, accurate constitutive model for all cases. It depends on the loading conditions, material behaviour etc. in each specific situation which constitutive model should be chosen. For this reason an additional comparison has been made for a different constitutive model as seen in chapter 4.4. The constitutive model that has been picked, is the Rotating Strain Crack Model. This constitutive model has been used for two wall configurations with squat piers. Below, the results are given for these two constitutive models:

Model	Shear capacity TSC (kN)	Shear capacity EMM (kN)	Failure mechanism TSC	Failure mechanism EMM
Wall 2	81.2	79.7	Rocking/Shear	Rocking
Wall 8	71	70	Rocking	Rocking

Table 19: Results constitutive models DIANA

The results of the two different constitutive models were similar as far as shear and displacement capacity concerned. As to the principal strains, the Rotating Strain Crack model showed better representation of the strains in the piers. This is due to the failure type 'Tensile strength head-joint defined by bed-joint frictional shear stress' as described in the DIANA Verification document.

As far as 3MURI concerned, the shear behaviour in the models were all based on the Mohr-Coulomb criterion which describes bed joint sliding shear. A different approach is describing the shear behaviour with the diagonal cracking formula of Turnsek & Cakovic. This has also been done for Wall 2 and 8 just like DIANA. In the below table a comparison of the results is shown:

Model	Shear capacity T&C (kN)	Shear capacity MC (kN)	Displacement capacity T&C (mm)	Displacement capacity MC (mm)
Wall 2	31.4	31.5	24.2	12.9
Wall 8	30.8	31.3	20.8	11.9

Table 20: Results different shear behaviour 3MURI

The outcome was different from the Mohr-Coulomb criterion. Although the results showed similar shear capacities this was not the case for the displacement capacities in the wall configurations. The models based on Turnsek & Cakovic show twice as large displacement capacities as in the models based on Mohr-Coulomb. This is due to the fact that in the models based on Turnsek & Cakovic no shear failure of a pier is occurring, but only flexural failure. Failure mechanisms like rocking have large displacement capacities compared to shear failure mechanisms. In general it is unnecessary to check the diagonal cracking failure for specific types of masonry as specified in 3.1.1 of the NEN EN 1996-1-1. For this reason the Mohr-Coulomb criterion is the most accurate to describe the shear behaviour of a pier.

5.5 Influence of lintels on the in-plane behaviour in DIANA

A small study has been conducted on the influence of lintels on the in-plane behaviour. In two wall configurations lintels have been modelled in DIANA. The influence of the lintels on the strain plots as seen in section 4.1.6 is minimal. A negligible difference can be seen in the base shear force between the two models in section 4.1.6.

6 Conclusions and recommendations

6.1 Conclusions

The main goal of this research was answering the following research question:

- *How do geometrical irregularities affect the assessment of the in-plane behaviour of single-storey URM wall facades performed with a mechanism based and a frame based analysis when compared to FEM?*

The objective has been studied by looking into single-floor wall façades. The conclusions made in this research can generally be applied to single-floor URM wall façades in Groningen of the masonry material Clay-Brick pre 1945. For other masonry types, differences can be seen for example in the definition of a slender pier. Also, significant changes in geometry outside the scope of this research can also have an influence on the results. For example, wall configurations with different heights of the spandrels can have an influence on the boundary conditions and their different formulations.

6.1.1 Effects of geometrical irregularities on the equivalent frame method

The following conclusions are drawn based on the comparison of the results of the DIANA and 3MURI models:

Based on the findings in this research, it can be concluded that the in-plane behaviour of a URM wall façade with EFM in 3MURI is not affected by the geometrical irregularities defined in this research in comparison with DIANA. This can be observed in the base shear capacities, displacement capacities and failure mechanisms of each model.

3MURI gave in general more conservative results than DIANA for all wall configurations. The models showed conservative results even with the presence of geometrical irregularities.

The base shear capacity in 3MURI is affected by geometrical irregularities in the same way as in DIANA. This is due to implementing the effective height method, the boundary conditions and the varying axial load. These applications assist in the consistency of the base shear capacity compared to DIANA when geometrical irregularities are present.

The ultimate displacement capacity or drift limit is in general lower in 3MURI compared to DIANA. This can be related to the force redistribution in DIANA, which allows gradual softening in contrast to 3MURI. The displacement capacity cannot be compared with DIANA as the material model computed high displacement capacities which did not show failure in the program. It can however be concluded that the displacement capacities were conservative compared to DIANA for all wall configurations. The SLaMA method did show differences with 3MURI. These differences were however caused by the different predictions of the failure mechanisms, which is again related to the varying axial load.

The failure mechanisms described by 3MURI are mostly corresponding to DIANA. However, DIANA shows often a combination of two failure mechanisms, whereas 3MURI only presents one failure mechanism as governing. It also needs to be noted that the failure type chosen in DIANA is more difficult for deducting the governing failure mechanism, because the diagonal cracks are hard to visualise in the strain plots. The geometrical irregularities did not have a large influence on the prediction of the failure mechanism by 3MURI compared to DIANA. By determining the effective height and taking into account the varying axial load, 3MURI could predict the failure mechanisms in correspondence to DIANA.

6.1.2 Effects of geometrical irregularities on the SLaMA method

The following conclusions are drawn based on the comparison of the results of the DIANA models and SLaMA calculations:

SLaMA gave in general more conservative results regarding force and displacement capacity than DIANA for all wall configurations. The models showed conservative results even with the presence of geometrical irregularities.

The SLaMA method showed large influences by the geometrical irregularities with respect to DIANA, but these influences were reduced slightly with a new formulation of the boundary conditions in the SLaMA. This can be observed in the base shear capacities, displacement capacities and failure mechanisms of each model.

The SLaMA method computed base shear capacities dependent on the geometrical irregularities compared to DIANA. The new formulation of the boundary conditions gave a base shear capacity slightly less dependent on the geometrical irregularities. The results show that the irregularities can vary the ratio of the shear capacity with DIANA between 0.34 and 0.75. This is still a large variation of results. The variation could be smaller by taking into account a varying axial load like 3MURI. This effect has been shown in the research of Nidal Ennali.

The ultimate displacement capacity or drift limit is in general lower in SLaMA compared to DIANA. This is due to the fact that the drift limit in SLaMA is determined for single piers. And based on the drift limits of the single piers a global displacement capacity is determined. The effect of the geometrical irregularities on the displacement capacities is only found compared to 3MURI.

SLaMA shows mainly flexural failure, which is caused by neglecting the axial load redistribution between the piers. This effect can be seen in the displacement capacities of SLaMA compared to 3MURI. SLaMA overestimates the drift limit in comparison with 3MURI. The influence of the varying axial load on the prediction of the failure mechanisms depends on the geometrical irregularities in a wall.

6.2   Recommendations

This part describes some recommendations which follows from this study and from the study Nidal Ennali. Both studies have been carried out in parallel and in cooperation with each other. Therefore, the recommendations resulting from these studies are combined in this chapter.

- Further research is required in determining how to include (in a simple way) the effect of the varying axial load at the top of the piers within the SLaMA method. This is relevant for predicting the failure mechanisms, especially when geometrical irregularities are present. Combining a simplified equivalent frame method with the SLaMA method could be a possible solution.
- A new procedure is needed to determine the boundary conditions of the piers in the in-plane loaded walls. Including the boundary conditions that lies between the double clamped boundary condition and the cantilevered boundary condition would result in a less conservative prediction and in a less dependent prediction on the geometrical irregularities in comparison with FEM with the SLaMA method.
- More research is needed to determine at which difference in shear capacities the combined failure type occurs. One specific failure type will happen when the difference in shear capacity is significant. How small needs this difference to be in order to adopt the combined failure mechanism within the SLaMA method?
- Further research is needed for the simplified methods regarding the effect of geometrical irregularities for cases with a higher complexity of geometry like multi-storey URM walls or 3D URM buildings.
- The irregularity indices could be altered or different irregularity indices could be defined. For example the slenderness ratio in the slender pier irregularity index can be replaced by the new slenderness ratio that has been defined in chapter 5.3.2.
- When deducting the failure mechanisms from the DIANA strain plots, it was difficult to observe shear failure mechanisms in the piers. It is possible to consider a different failure type from the Engineering Masonry Model which gives a more accurate representation of the strain plot, like the failure type 'Diagonal Staircase-cracks'.
- The different constitutive models in DIANA did not show large differences in results, however the walls that were modelled were sensitive to rocking. More research is needed on whether walls with shear failure could give different results for the two constitutive models.
- Different model parameters could be used in 3MURI and researched. For example, the model parameters based on the NPR9998:2018 could be implemented instead of the Eurocode NL parameters.

7 References

3MURI. (2019). *3MURI Manual version 12.2.0.* S.T.A. Data.

Beyer, K. (2011). *Peak and residual strengths of brick masonry spandrels.* Switzerland: ELSEVIER.

F. Messali, J. R. (2017). *In-plane drift capacity at near collapse of rocking unreinforced calcium silicate and clay masonry piers.* Delft.

Franklin L. Moon, T. Y. (2006). *Recommendations for Seismic Evaluation and Retrofit of Low-Rise URM Structures.* JOURNAL OF STRUCTURAL ENGINEERING.

GUIDO MAGENES, G. M. (1997). *IN-PLANE SEISMIC RESPONSE OF BRICK MASONRY WALLS.* Pavia.

Knox, C. (2012). Non-linear equivalent frame modelling: Assessment of a two-storey perforated unreinforced masonry wall.

Lagomarsino, S., Penna, A., Galasco, A., & Cattari, S. (2013). *TREMURI program: An equivalent frame model for the nonlinear sesimic analysis of masonry buildings.* Elsevier.

Messali, F., & Rots, J. (2018). *In-plane drift capacity at near collapse of rocking unreinforced calcium silicate and clay masonry piers.*

MIHA TOMAZEVIC, I. K. (1997). *SEISMIC BEHAVIOUR OF CONFINED MASONRY WALLS.* Slovenia.

Moon, F. (2004). *Seismic strengthening of low-rise unreinforced masonry buildings.* Atlanta: Georgia Institute of Technology.

Moon, F. L. (2004). *Seismic Strengthening of Low-Rise Unreinforced Masonry Structues with Flexible Diaphragms.*

NEN. (2018). *NPR9998.*

NZSEE. (2017). *Unreinforced Masonry Buildings C8.*

Parisi, F., & Augenti, N. (2012). *Seismic capacity of irregular unreinforced masonry walls with openings.*

Quagliarini, E., Maracchini, G., & Clementi, F. (2017). *Uses and limits of the Equivalent Frame Model on existing unreinforcedmasonry buildings for assessing their seismic risk: A review.*

Schreppers, G., Garofano, A., Messali, F., & Rots, J. (2017). *DIANA Validation report for Masonry modelling.*

Siano, R., Camata, G., Sepe, V., Spacone, E., Roca, P., & Pela, L. (2017). Finite Elements vs. Equivalent-Frame Models for URM walls' in-plane behaviour.

Smily, T. J., Deepa, M. V., & Sivan, P. P. (2018). Study of seismic effect in unreinforced masonry structures with openings.

Tianyi Yi, F. L. (2006). *Lateral Load Tests on a Two-Story Unreinforced Masonry Building.*

Vecchio, F., & Collins, M. (1986). *The modified compression field theory for reinforced concrete elements subjected to shear.* ACI Journal.

A. Appendix A: SLaMA calculation

Below the full SLaMA calculation is described. This procedure was used for all wall configuration in this report.

1. **Define geometry of the wall configurations:**

```
# Define geometry piers and spandrels here as an array:
lpiers = np.array([np.array([5.66,0.01]),np.array([1.85, 1.38, 1.85]),np.array([1.65, 1.22, 1.65]), np.array([1.34,1,1.34]),
                np.array([1.75, 1.3, 1.75]),np.array([1.05,0.79,0.79,1.05]),np.array([1.44,0.8,1.44]) ,
                np.array([0.695,2.29,0.695]),np.array([1.27,0.61,1.8]), np.array([0.81,1.01,1.86]),
                np.array([0.58,0.95,2.15]), np.array([0.31,0.95,2.42])])

hpp = np.array([2.18, 1.63,2.17])
#hpp = np.array([2.17, 1.63,2.18]) negative direction
hpiers = np.array([np.array([2.72,0.1]),hpp,hpp,hpp,hpp,np.array([2.18, 1.63,1.63,2.17]),hpp,hpp,hpp,hpp,hpp,hpp])
lspandrels = np.array([np.array([0.01]),np.array([0.29,0.29]),np.array([0.57,0.57]),np.array([0.99,0.99])
                ,np.array([0.43,0.43]),np.array([0.66,0.66,0.66]),np.array([0.99,0.99]),np.array([0.99,0.99]),
                 np.array([0.99,0.99]),np.array([0.99,0.99]),np.array([0.99,0.99]),np.array([0.99,0.99])])

hspandrels = np.array([np.array([0.01]),np.array([0.55,0.55]),np.array([0.55,0.55]),np.array([0.55,0.55]),
                np.array([0.55,0.55]),np.array([0.55,0.55,0.55]),np.array([0.55,0.55]),np.array([0.55,0.55]),
                np.array([0.55,0.55]),np.array([0.55,0.55]),np.array([0.55,0.55]),np.array([0.55,0.55])])
i = np.array([[len(lpiers[0]),len(lpiers[1]),len(lpiers[2]),len(lpiers[3]),
            len(lpiers[4]),len(lpiers[5]),len(lpiers[6]),len(lpiers[7]),
            len(lpiers[8]),len(lpiers[9]),len(lpiers[10]),len(lpiers[11])]]) # i is number of piers
#lspandrels[1] = np.array([0.99,0.99])
print(1.85/2+1.38/2+0.29)
```

2. **Calculation of the shear capacities of the spandrels:**

```
def V(lp,hp,i,lsp,hsp,psi):
    W = lp * hp * tp * vg
    P = q*lp
    F = P+W
    sigmay = F/(lp * tp)
    sigma = np.zeros(i-1)
    for l in range(i-1):
        sigma[l] = (sigmay[l]+sigmay[l+1])/2
    # # Spandrels: Flexural strength
    fteff= 1.3*((c+(0.5*mu*sigma)))+(c/(2*mu))
    betas=lsp/hsp
    fa=vg*lsp*tp*hsp/2
    fdt=0.5*c+(fa*mu)
    psp=(1+betas)*fdt*(lsp/np.sqrt(lsp**2+hsp**2))
    Vfl=(fteff)*(hsp**2)*tp/(3*lsp)
    fhm=0.5*fma
    Vflr= ((psp*(hsp**2)*tp)/(lsp))*(1-(psp/(0.85*fhm)))

    # # Spandrels: Probable shear strength
    Vs1=(2/3)*(c)*hsp*tp
    b = np.zeros(i-1)
    for j in range(i-1):
        if lsp[j]/hsp[j] > 1.5:
            b[j] = 0.67
        elif lsp[j]/hsp[j] <= 1.5 and lsp[j]/hsp[j] >=1:
            b[j] = 1+(((lsp[j]/hsp[j])-1)* (0.67-1)/(1.5-1))

        elif lsp[j]/hsp[j] < 1:
            b[j]=1.0
    #print(b) ##beta spandrels
    Vs2=(fdt*b*np.sqrt(1+(psp/fdt))*hsp*tp)
    VS = np.zeros(i-1)
    VR = np.zeros(i-1)
    for j in range(i-1):
        VS[j] = min(Vs1[j], Vfl[j])
        if VS[j] == Vs1[j]:
            VR[j] = Vs2[j]
        else:
            VR[j] = Vflr[j]
        if VR[j] >= VS[j]:
            VR[j] = VS[j]
    #print(Vflr,Vfl,Vs1,Vs2) ## check spandrel capacities
```

3. Calculation of the shear capacities of the piers and assigning respectively the failure mechanisms to each pier:

```python
#Failure mechanism 1: Toe crushing capacity:
Vr = F*lp/(2*psi*hp)*(1-1.15*sigmay/fma)
#Failure mechanism 2: Sliding shear capacity:
alpha = psi*hp/lp
Vra1 = (2*mu*F**2 + 3*F*fmav*tp*lp)/(6*alpha*fmav*tp*lp + 2*F)#Diagonal cracking
Vrar = (2*mu*F**2)/(2*F)
Vrb1 = (3*fb*lp*tp*F)/(6*fb*alpha*lp*tp+20*F) # Sliding shear capacity
theta = 0.0135 * ( 1 - 2.6 * sigmay/fma) * (href/hp) * np.sqrt(hp/lp)
#Failure mechanism 3: Diagonal Tensile strength:
bp = np.zeros(i)
for j in range(i):
    if hp[j]/lp[j] > 1.5:
        bp[j]=0.67
    else:
        bp[j]=1.0

fa= (W/2 +P)/(tp*lp)
fdt=0.5*c+fa*mu
An=lp*tp

Vdt=fdt*An*bp*np.sqrt(1+(fa/fdt))
#print(Vra1, Vrb1, Vr, Vdt) ## Check Pier capacities
Vr2 = np.zeros(i)
mechanism = ['Rocking','Sliding shear a','Sliding shear b', 'Diagonal Tensile Failure']
failure = []

for k in range(i):
    Vr2[k] = np.min([Vra1[k],Vrb1[k],Vr[k], Vdt[k]])
    if Vr2[k] == Vra1[k]:
        failure.append(mechanism[1])
    elif Vr2[k] == Vrb1[k]:
        failure.append(mechanism[2])
    elif Vr2[k] == Vr[k]:
        failure.append(mechanism[0])
    elif Vr2[k] == Vdt[k]:
        failure.append(mechanism[3])
```

4. Calculation of the drift capacities of the piers:

```python
thetaNC = np.zeros(i)
thetaSD = np.zeros(i)
for k in range(i):
    if Vr2[k] == Vra1[k]:
        thetaNC[k] = 0.0075
        thetaSD[k] = 0.003
    else:
        thetaNC[k] = theta[k]
        thetaSD[k] = theta[k]
uNC1 = thetaNC*hp
uSD1 = thetaSD*hp
ugrens = 1.5/100*hp
uNC = np.zeros(i)
uSD = np.zeros(i)
for k in range(i):
    uNC[k] = np.min([uNC1[k],ugrens[k]])
    uSD[k] = np.min([uSD1[k],ugrens[k]])
#print(Vra1, Vrb1, Vr)
return Vr2, VR, failure, Vrar, uNC, uSD, VS, Vra1, Vrb1, Vr
```

B. Appendix B: DIANA Results

In the following figures the DIANA strain plots are given for each wall configuration at five different stages.

Wall 1
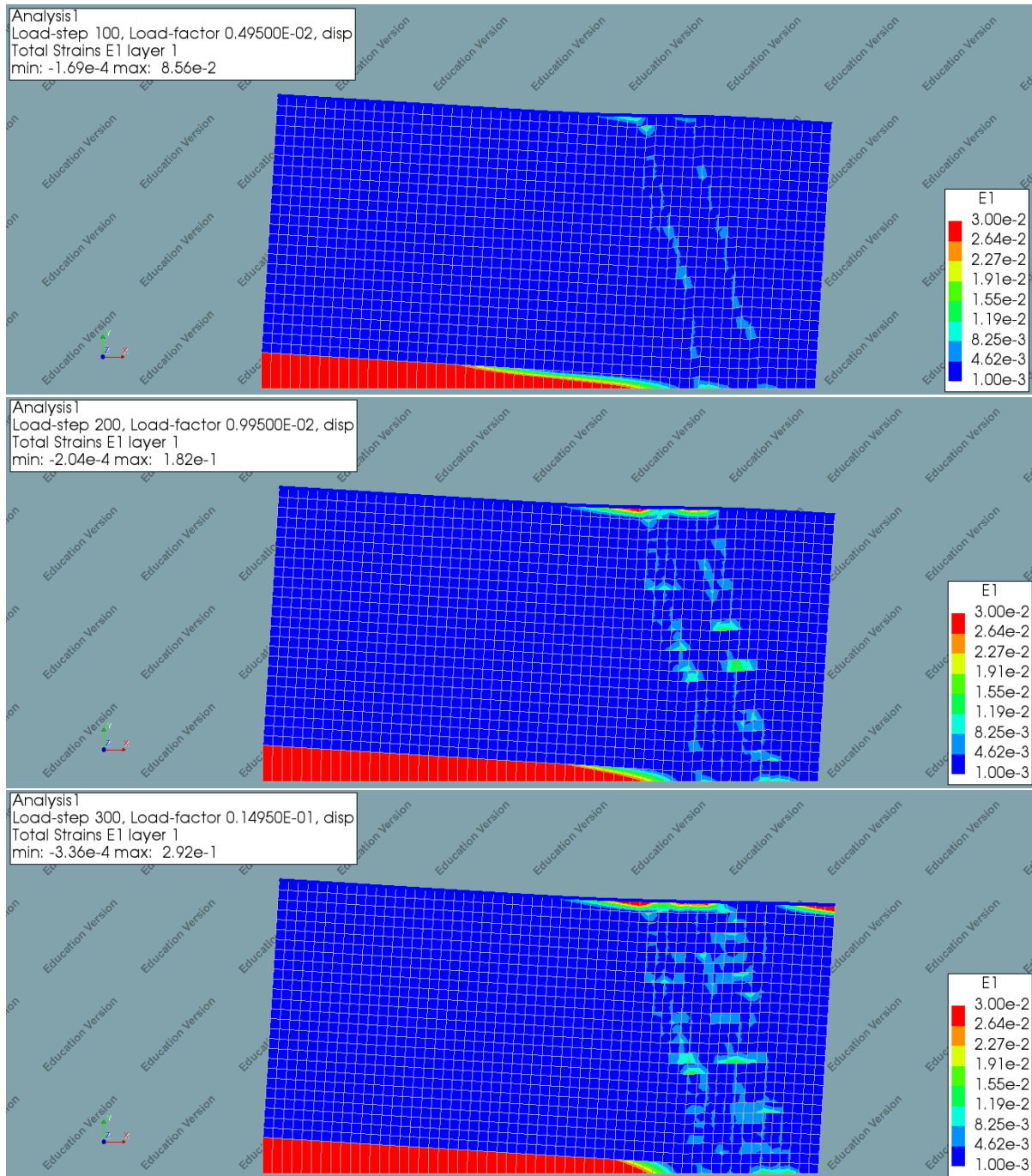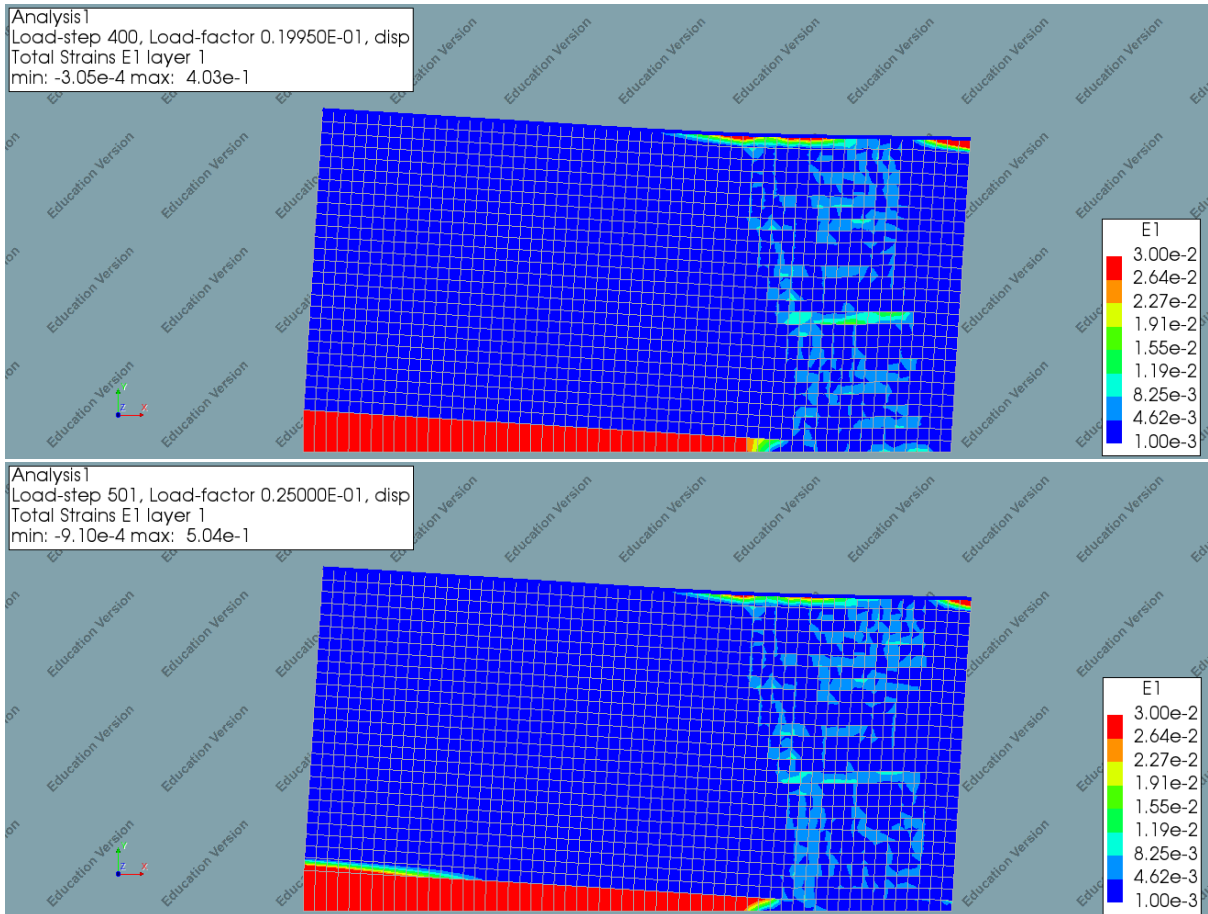
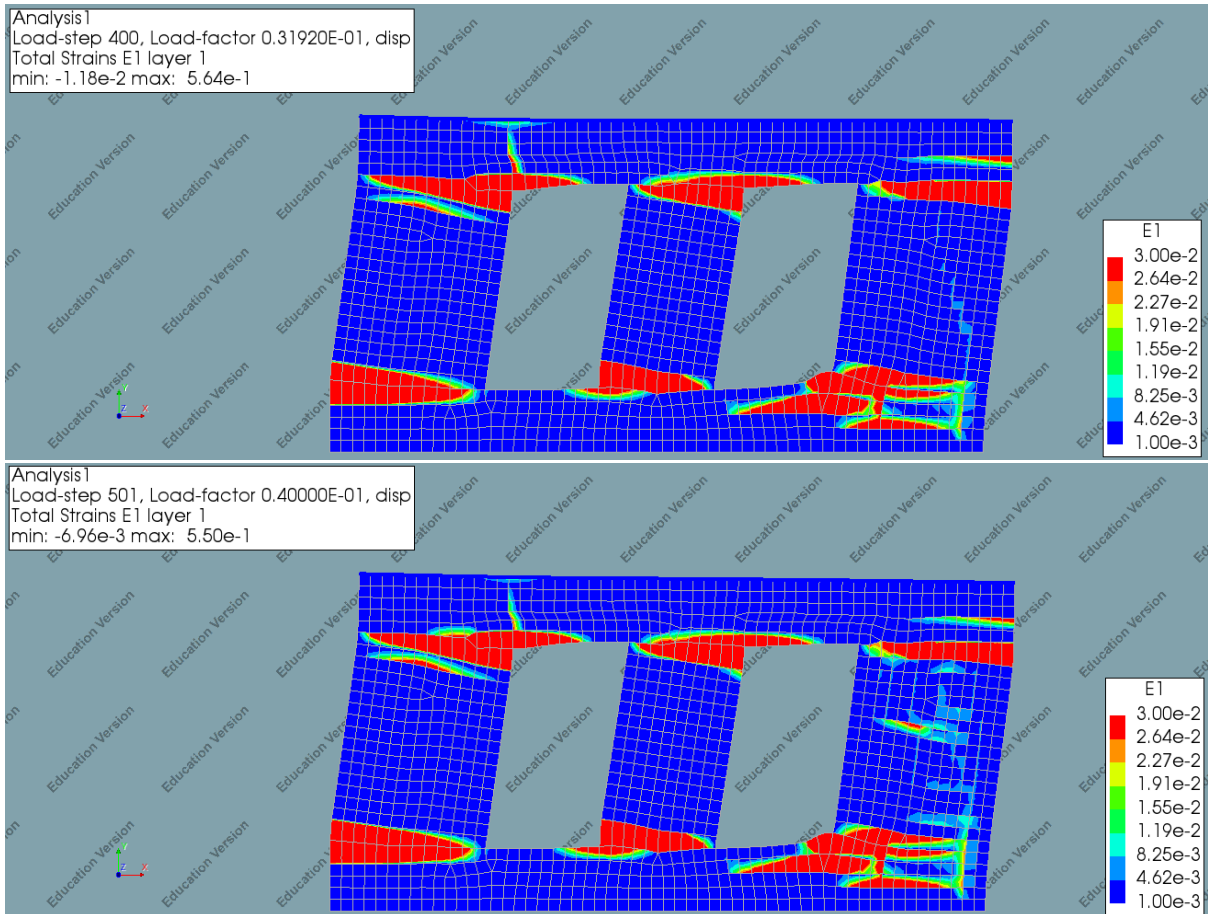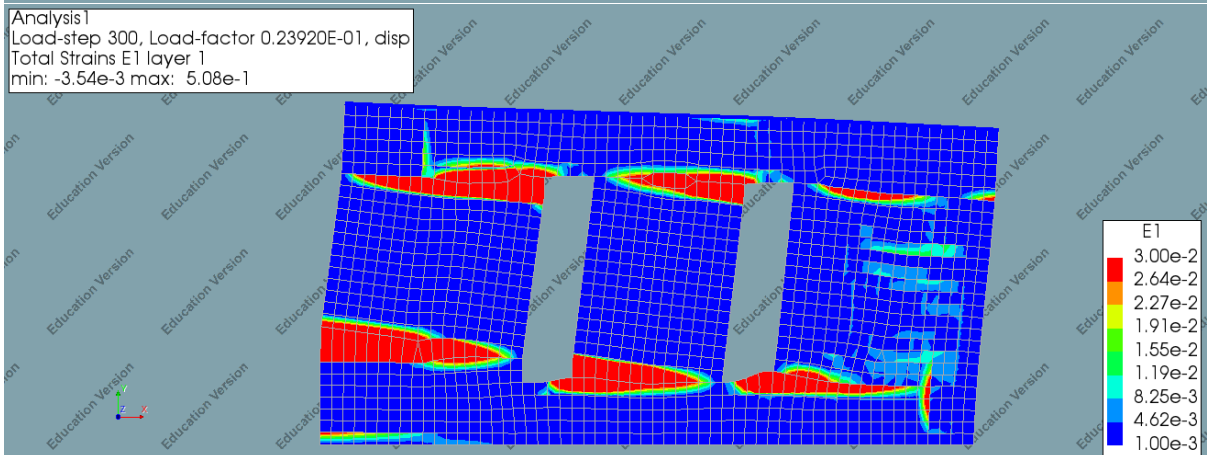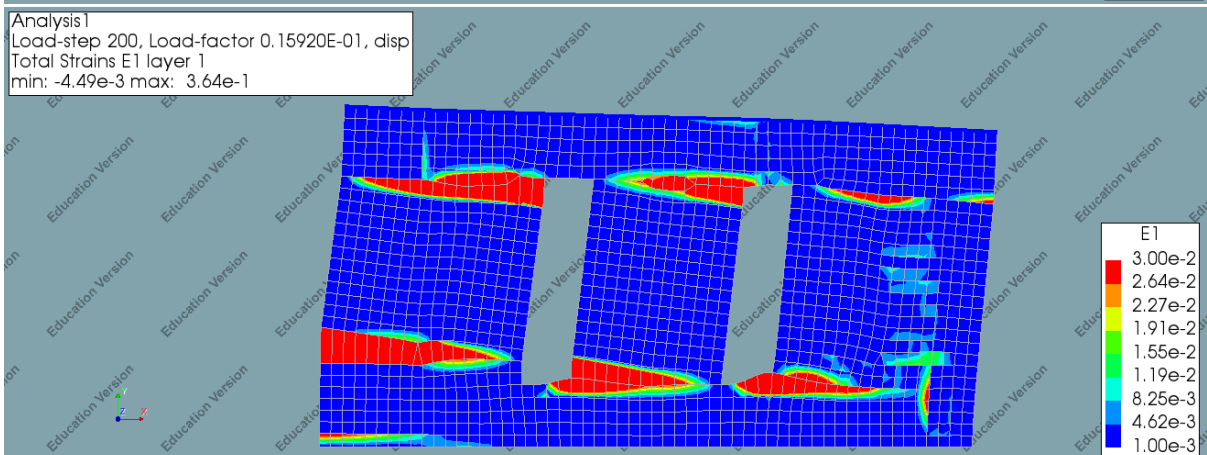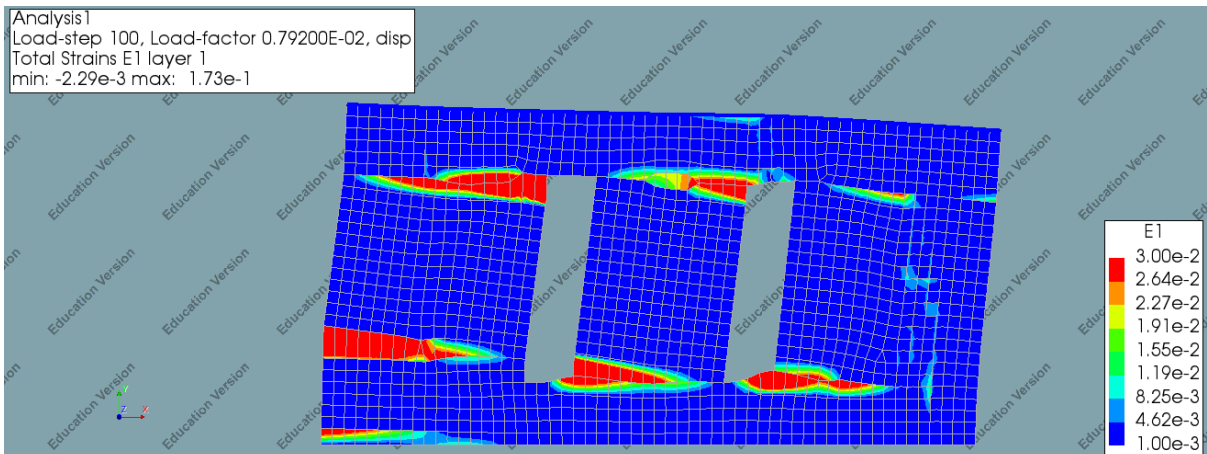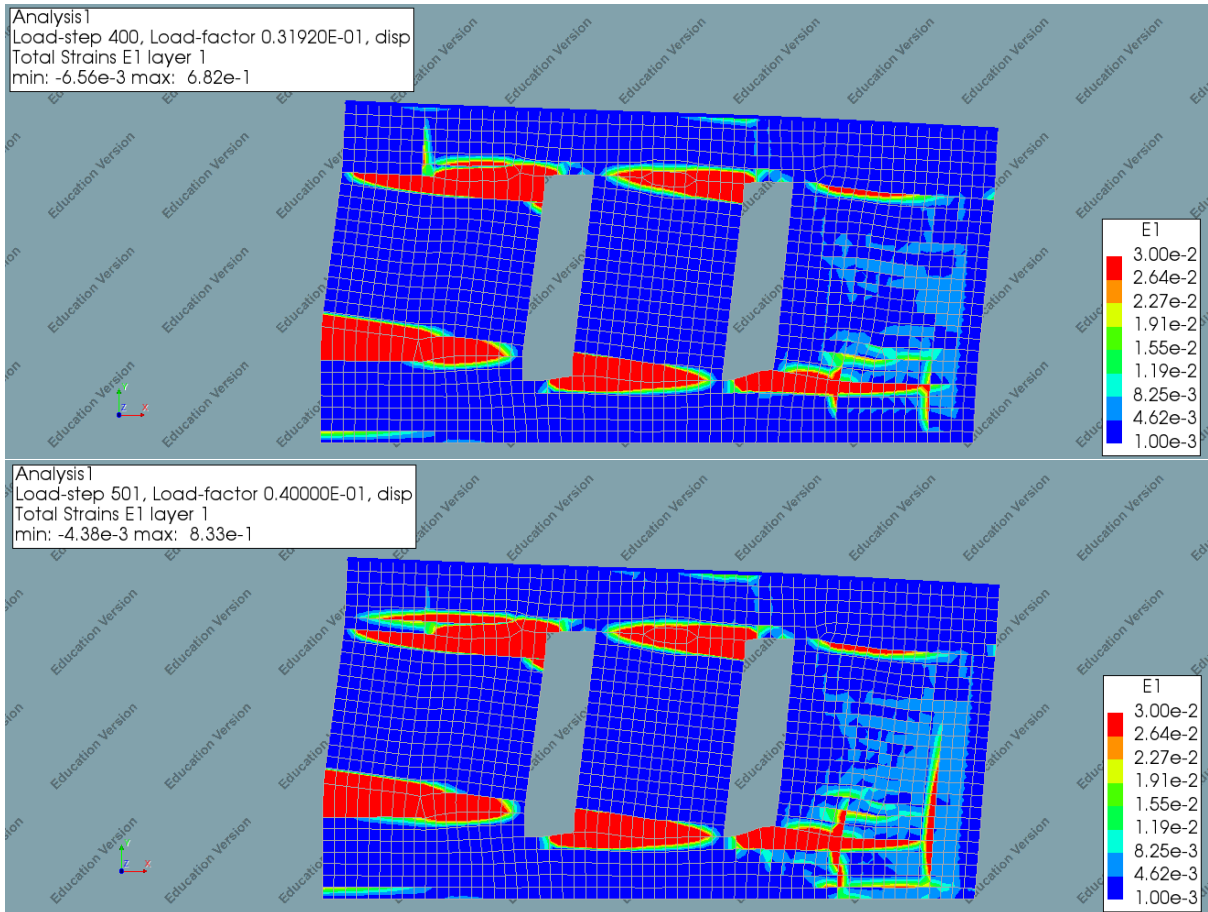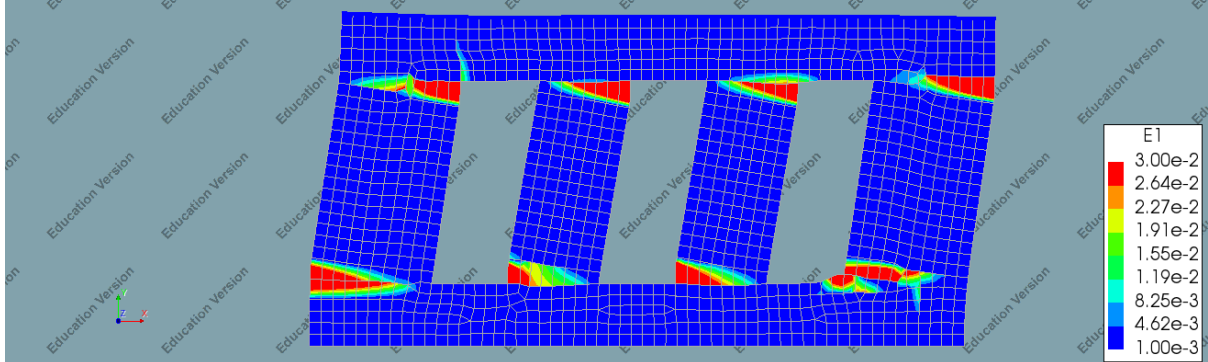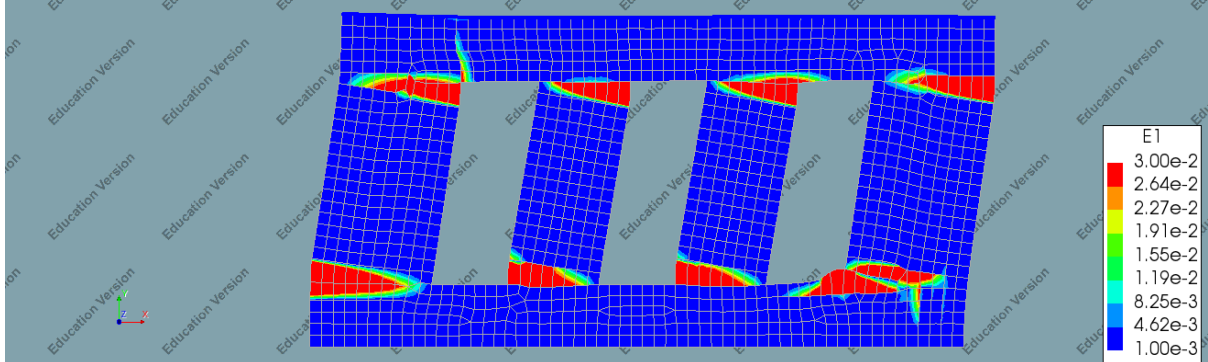*Figure 69: Principal strain plot Wall 1 for steps 100, 200, 300, 400 and 501*

Wall 2
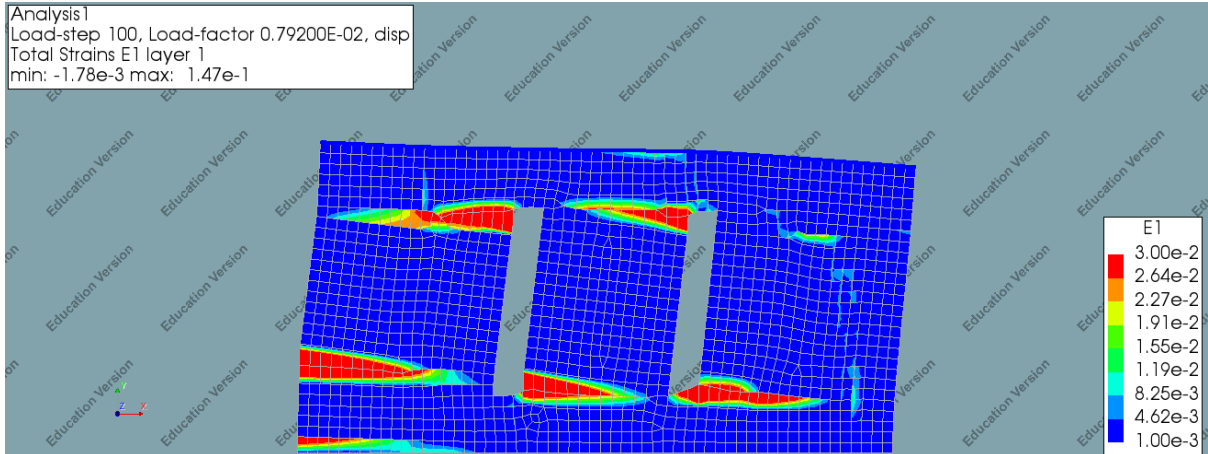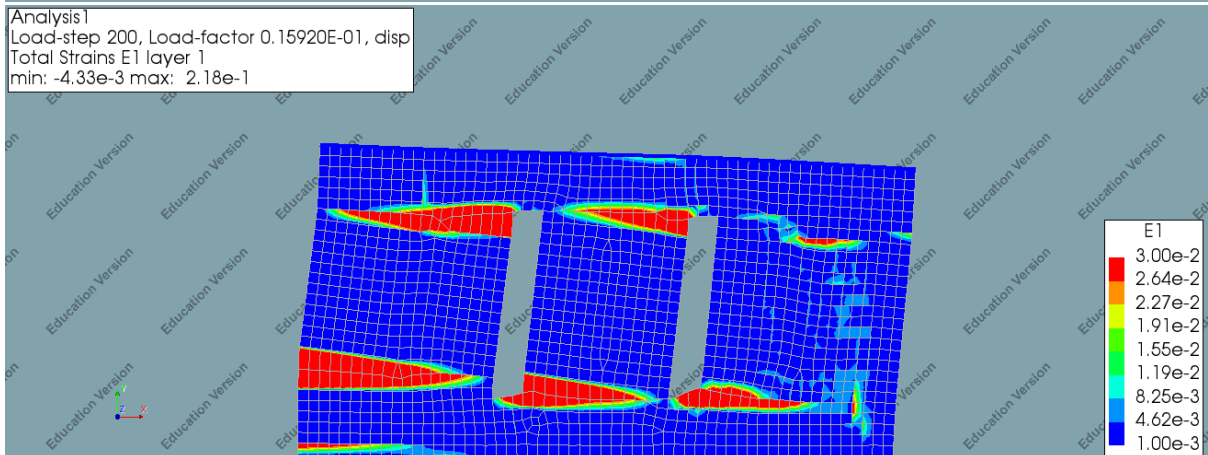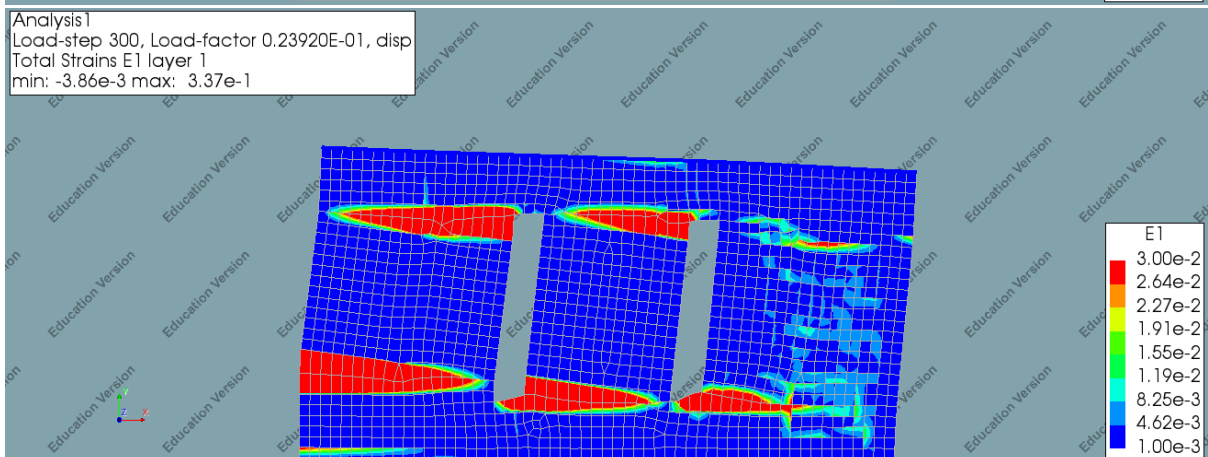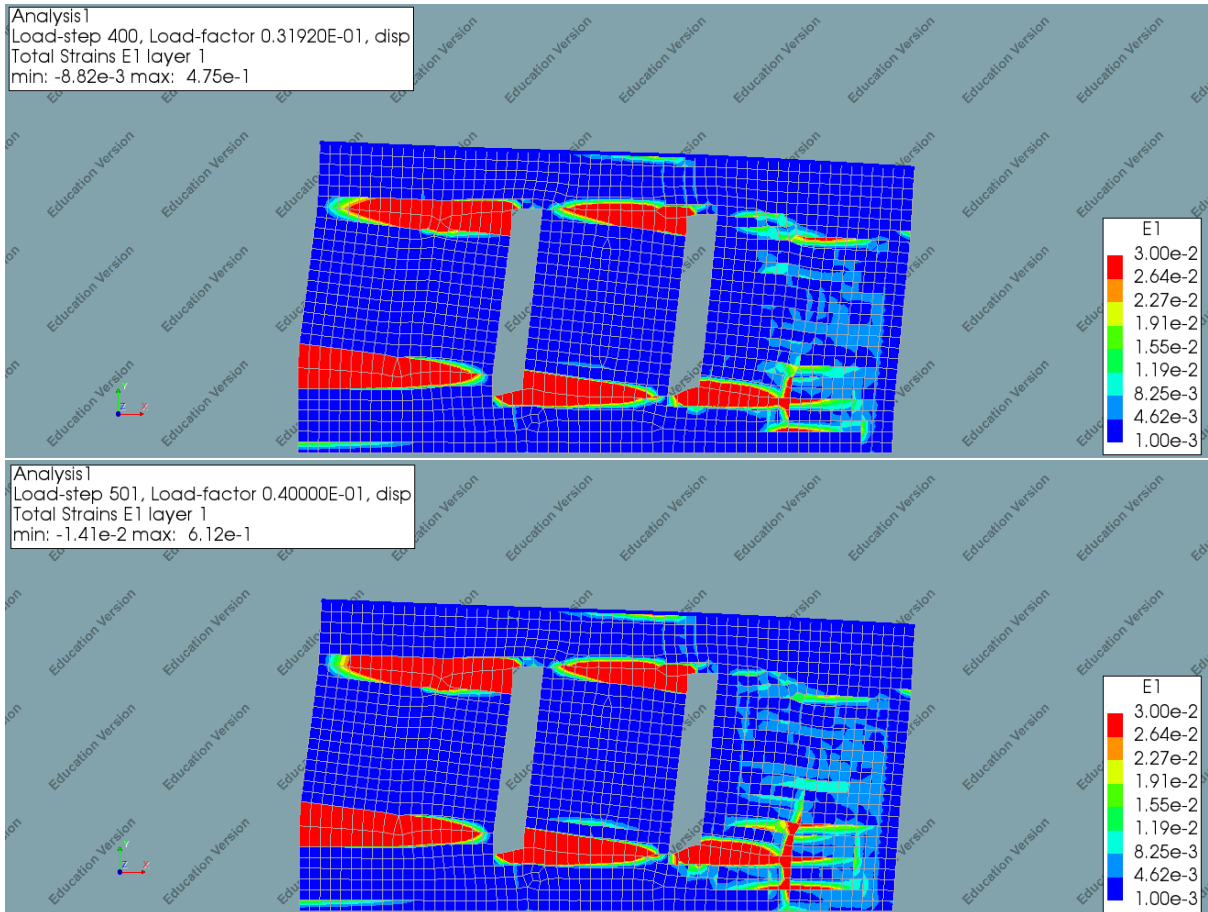
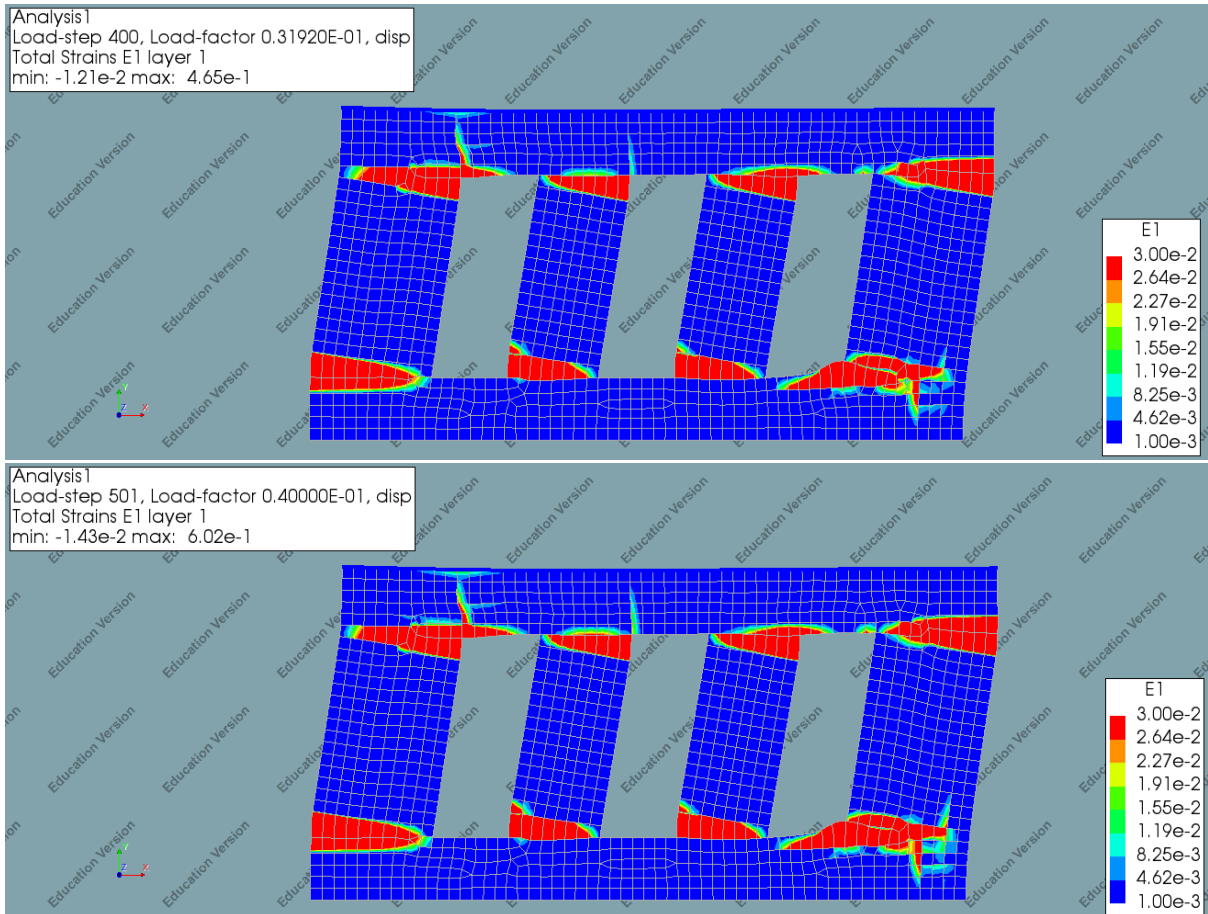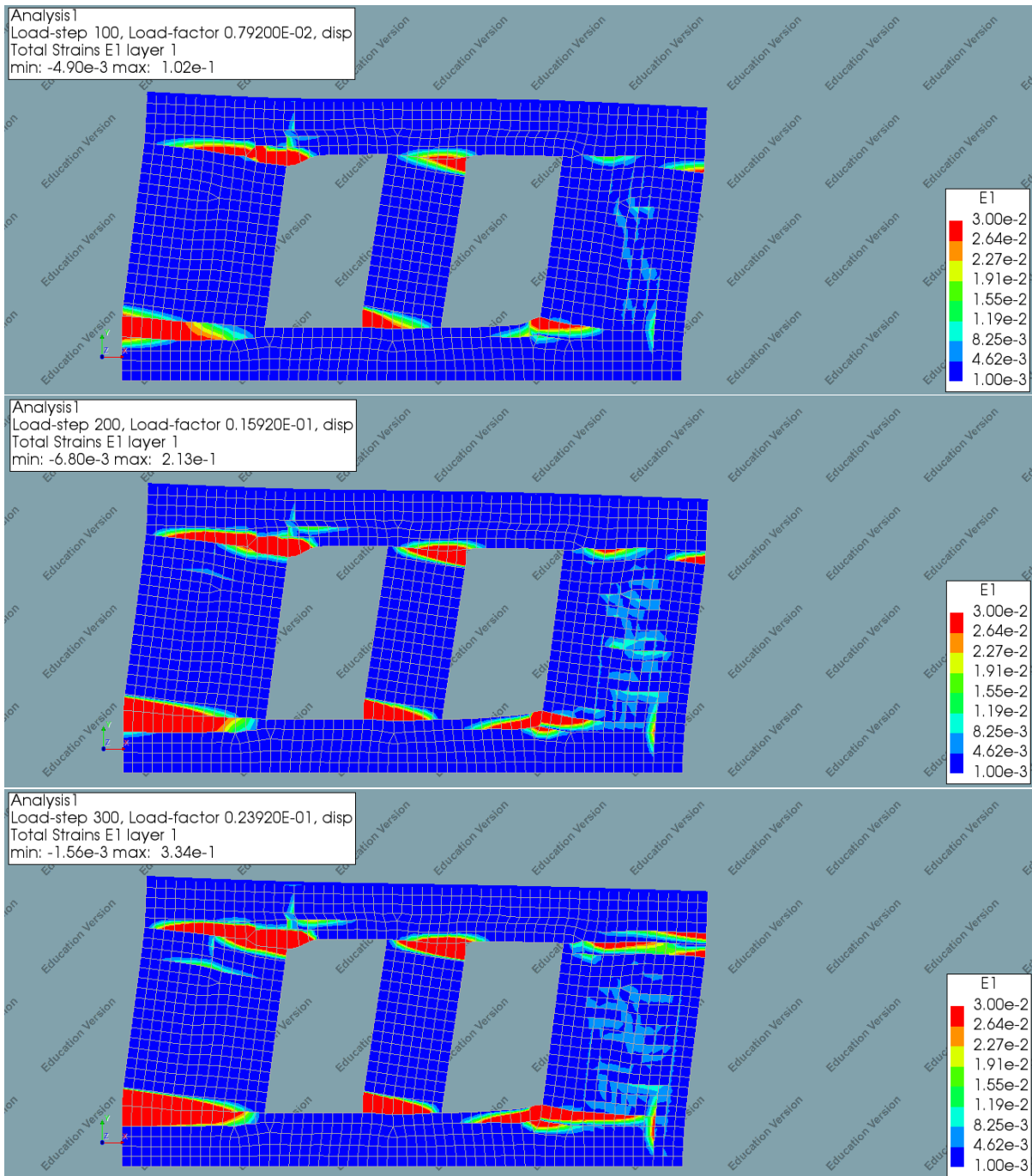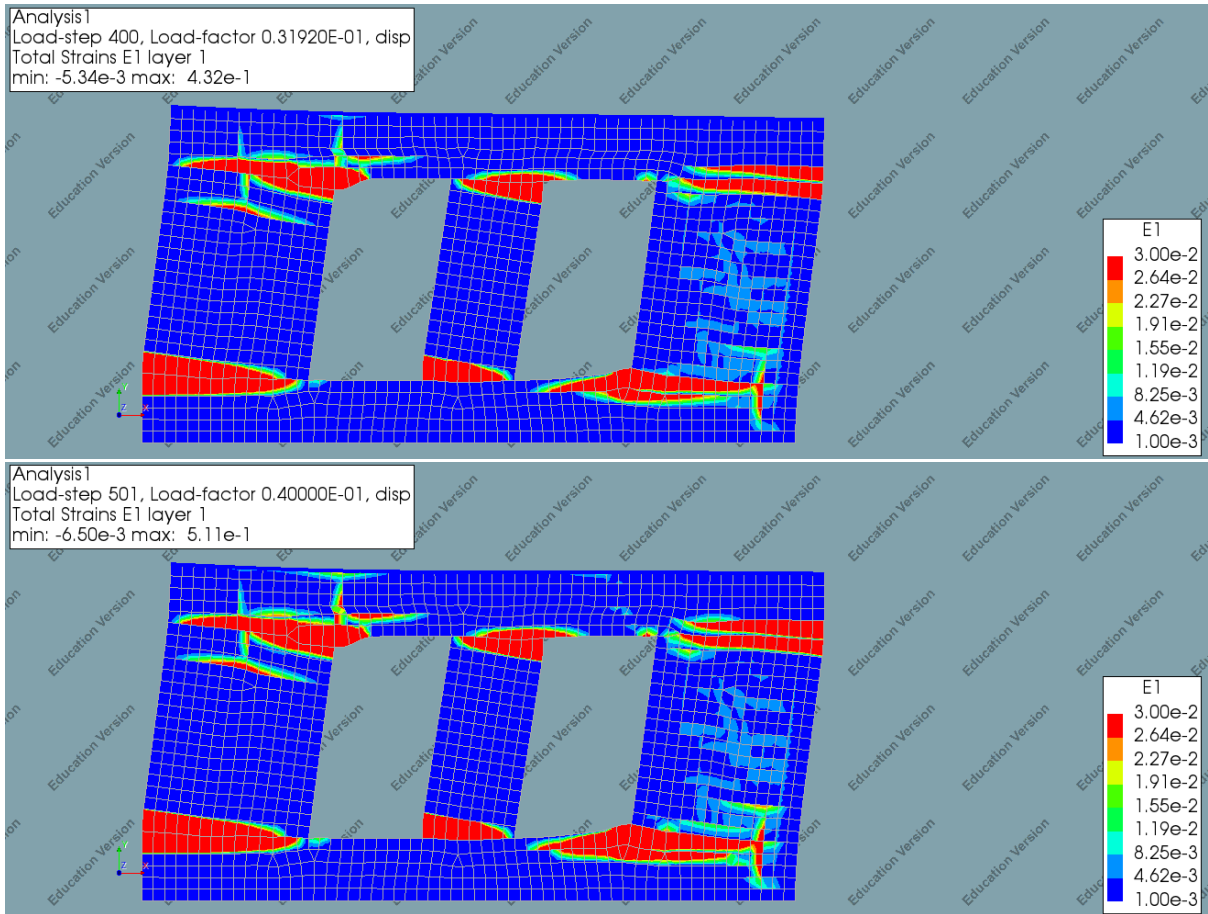*Figure 70: Principal strain plot Wall 2 for steps 100, 200, 300, 400 and 501*

Wall 3

Analysis1
Load-step 100, Load-factor 0.79200E-02, disp
Total Strains E1 layer 1
min: -3.28e-3 max: 1.48e-1

E1
3.00e-2
2.64e-2
2.27e-2
1.91e-2
1.55e-2
1.19e-2
8.25e-3
4.62e-3
1.00e-3

Analysis1
Load-step 200, Load-factor 0.15920E-01, disp
Total Strains E1 layer 1
min: -4.75e-3 max: 3.17e-1

E1
3.00e-2
2.64e-2
2.27e-2
1.91e-2
1.55e-2
1.19e-2
8.25e-3
4.62e-3
1.00e-3

Analysis1
Load-step 300, Load-factor 0.23920E-01, disp
Total Strains E1 layer 1
min: -5.38e-3 max: 4.40e-1

E1
3.00e-2
2.64e-2
2.27e-2
1.91e-2
1.55e-2
1.19e-2
8.25e-3
4.62e-3
1.00e-3

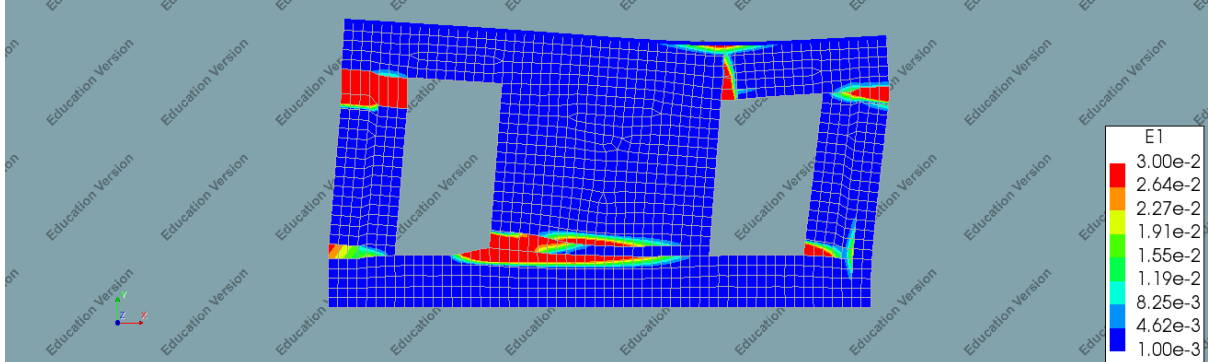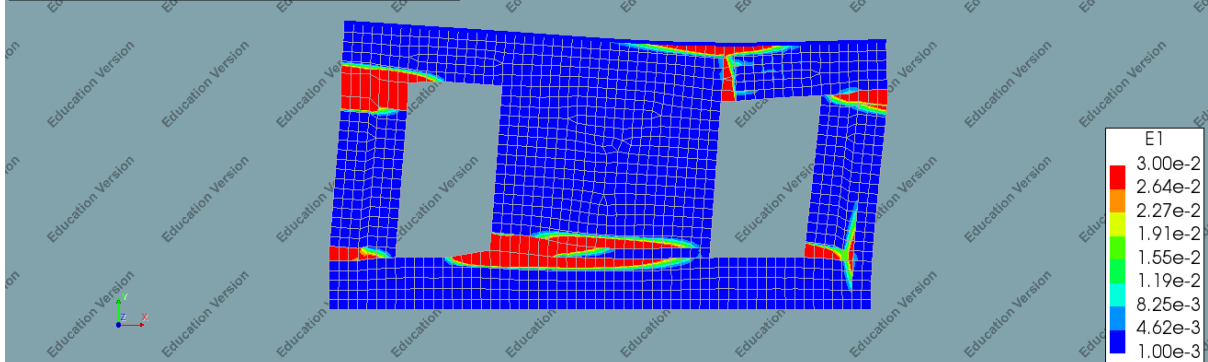*Figure 71: Principal strain plot Wall 3 for steps 100, 200, 300, 400 and 501*

Wall 4
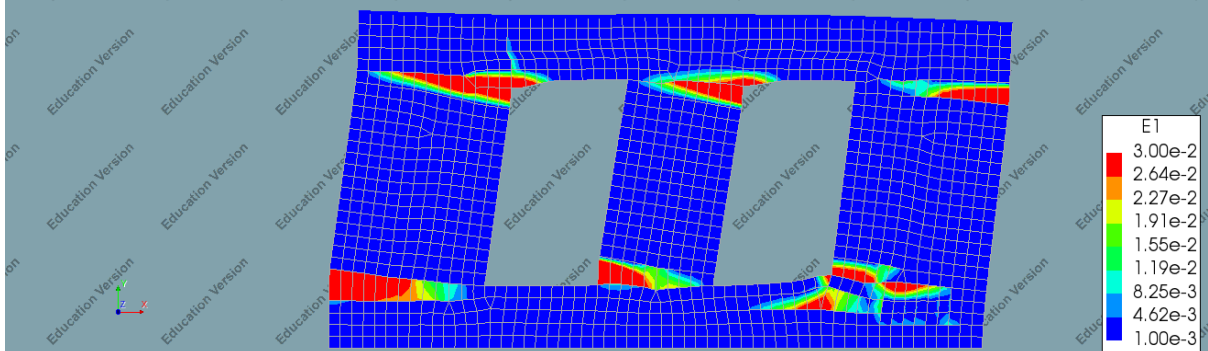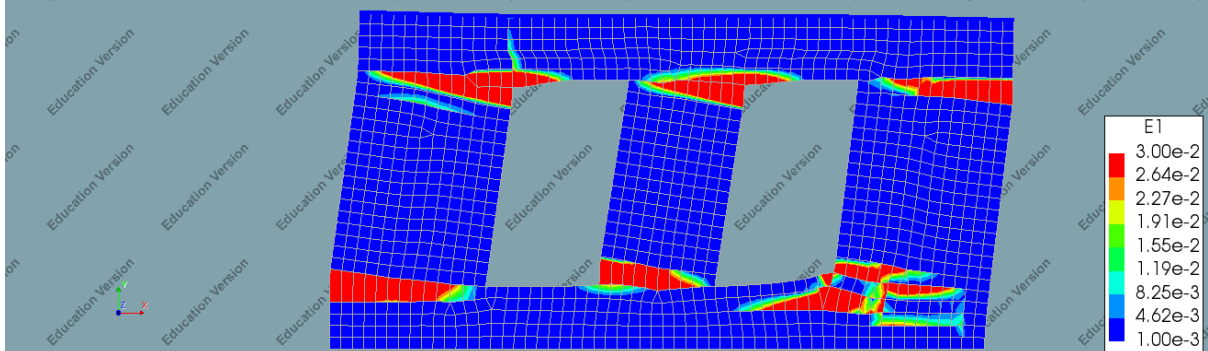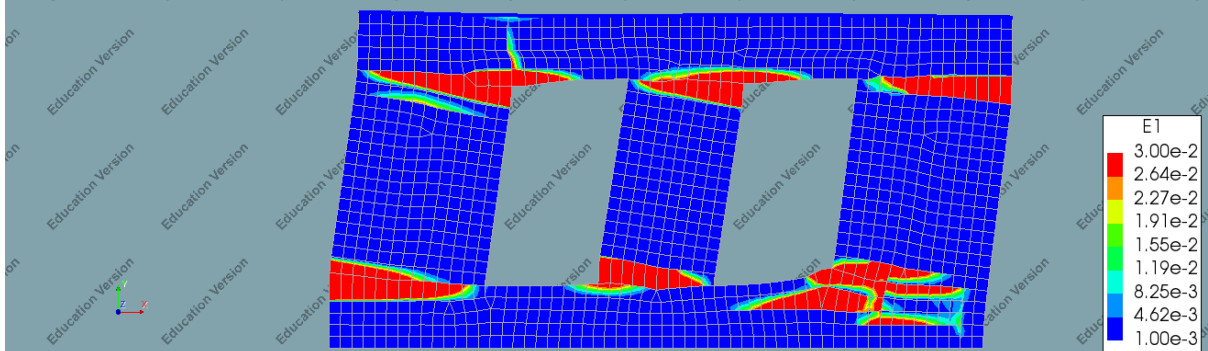
Figure 72: Principal strain plot Wall 4 for steps 100, 200, 300, 400 and 501

Wall 5

Analysis1
Load-step 100, Load-factor 0.79200E-02, disp
Total Strains E1 layer 1
min: -2.29e-3 max: 1.73e-1

E1
3.00e-2
2.64e-2
2.27e-2
1.91e-2
1.55e-2
1.19e-2
8.25e-3
4.62e-3
1.00e-3

Analysis1
Load-step 200, Load-factor 0.15920E-01, disp
Total Strains E1 layer 1
min: -4.49e-3 max: 3.64e-1

E1
3.00e-2
2.64e-2
2.27e-2
1.91e-2
1.55e-2
1.19e-2
8.25e-3
4.62e-3
1.00e-3

Analysis1
Load-step 300, Load-factor 0.23920E-01, disp
Total Strains E1 layer 1
min: -3.54e-3 max: 5.08e-1

E1
3.00e-2
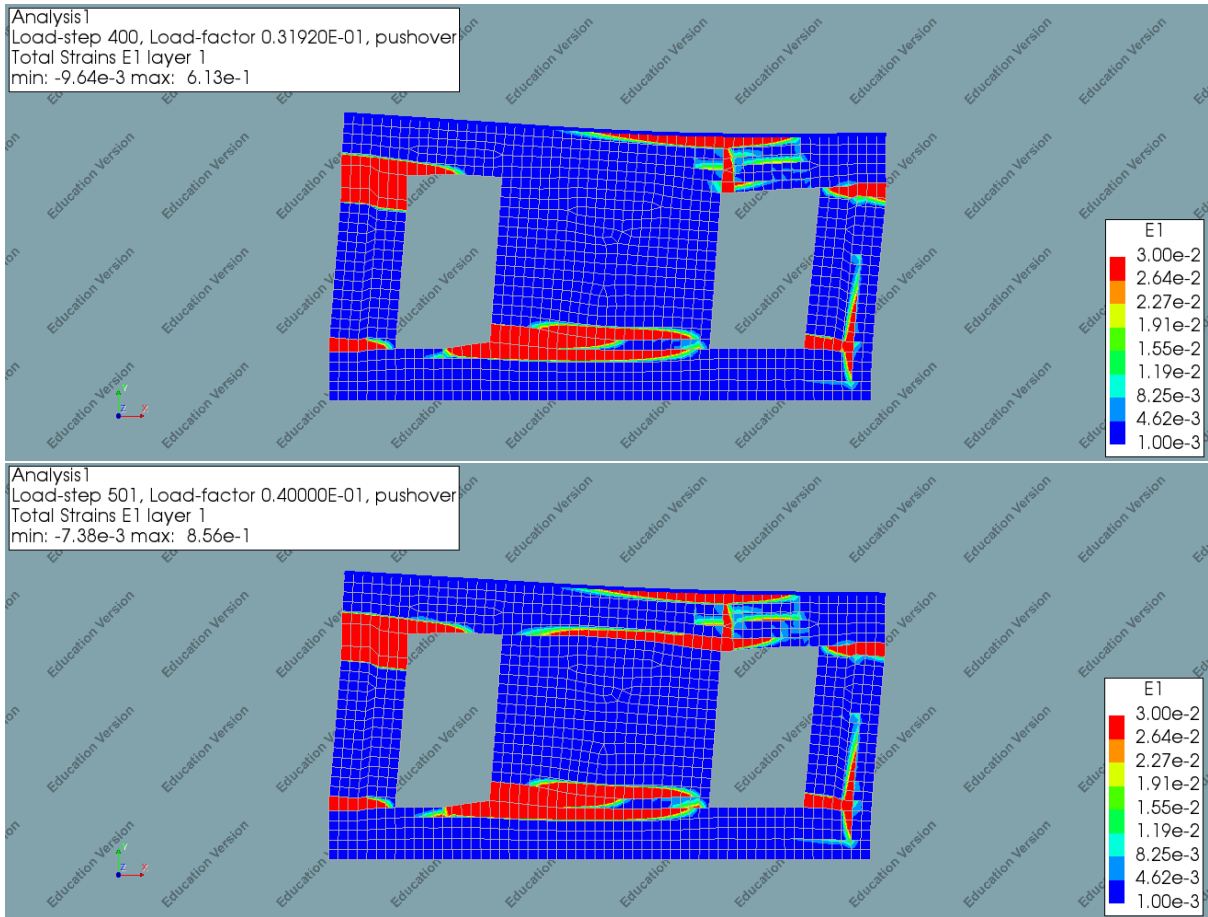2.64e-2
2.27e-2
1.91e-2
1.55e-2
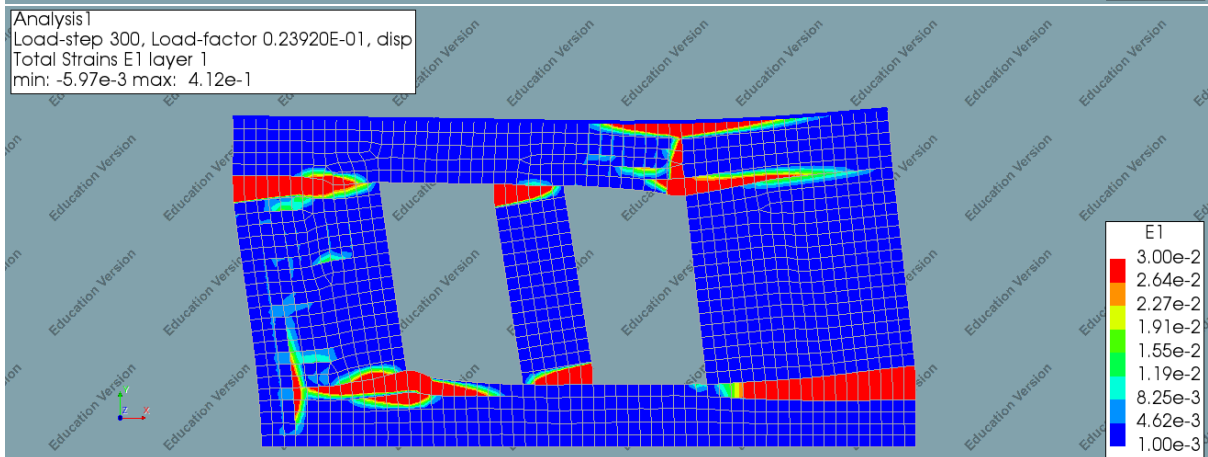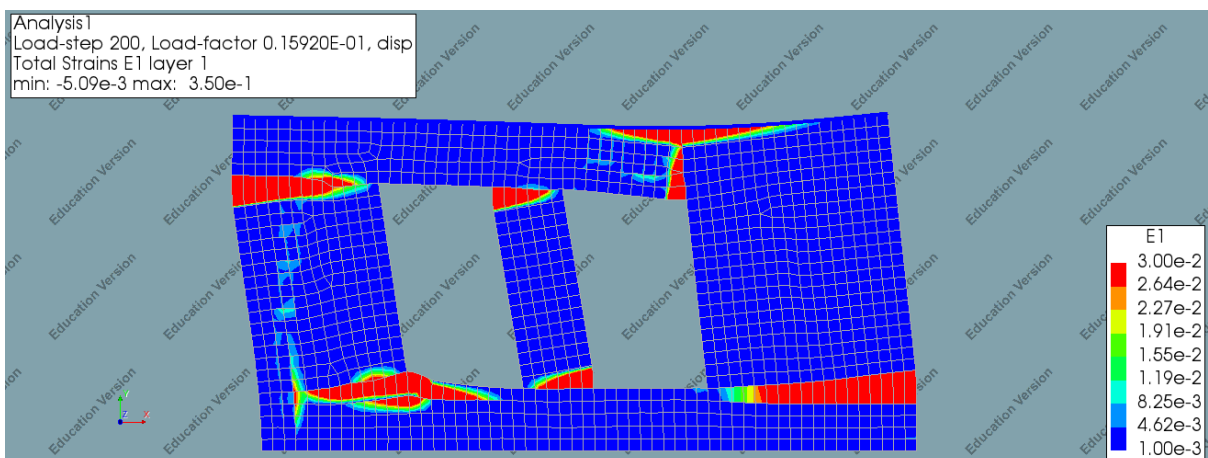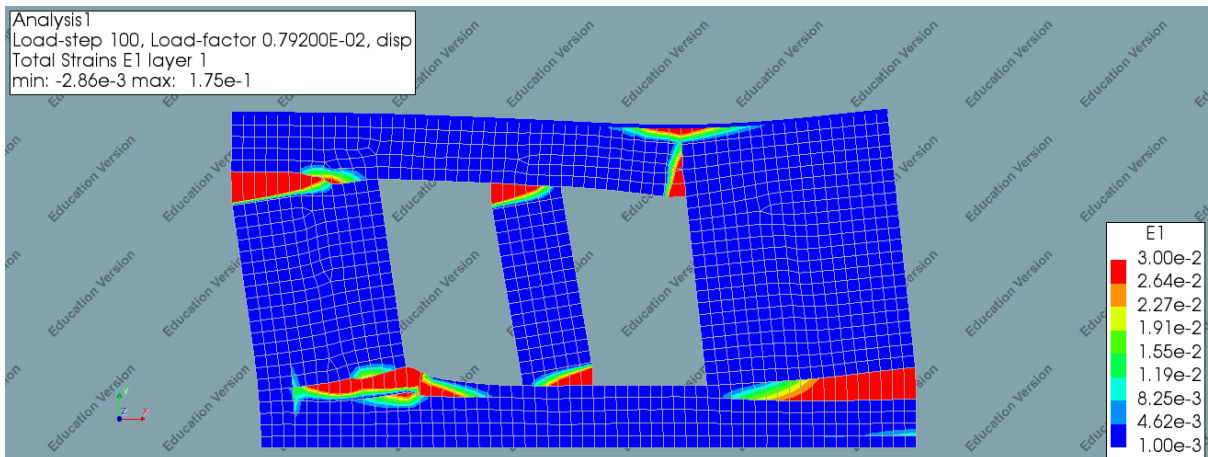1.19e-2
8.25e-3
4.62e-3
1.00e-3

Figure 73: Principal strain plot Wall 5 for steps 100, 200, 300, 400 and 501

Wall 6

Analysis1
Load-step 100, Load-factor 0.79200E-02, disp
Total Strains E1 layer 1
min: -3.83e-3 max: 1.05e-1

E1

3.00e-2
2.64e-2
2.27e-2
1.91e-2
1.55e-2
1.19e-2
8.25e-3
4.62e-3
1.00e-3

Analysis1
Load-step 200, Load-factor 0.15920E-01, disp
Total Strains E1 layer 1
min: -7.07e-3 max: 2.47e-1

E1

3.00e-2
2.64e-2
2.27e-2
1.91e-2
1.55e-2
1.19e-2
8.25e-3
4.62e-3
1.00e-3

Analysis1
Load-step 300, Load-factor 0.23920E-01, disp
Total Strains E1 layer 1
min: -1.08e-2 max: 3.46e-1

E1

3.00e-2
2.64e-2
2.27e-2
1.91e-2
1.55e-2
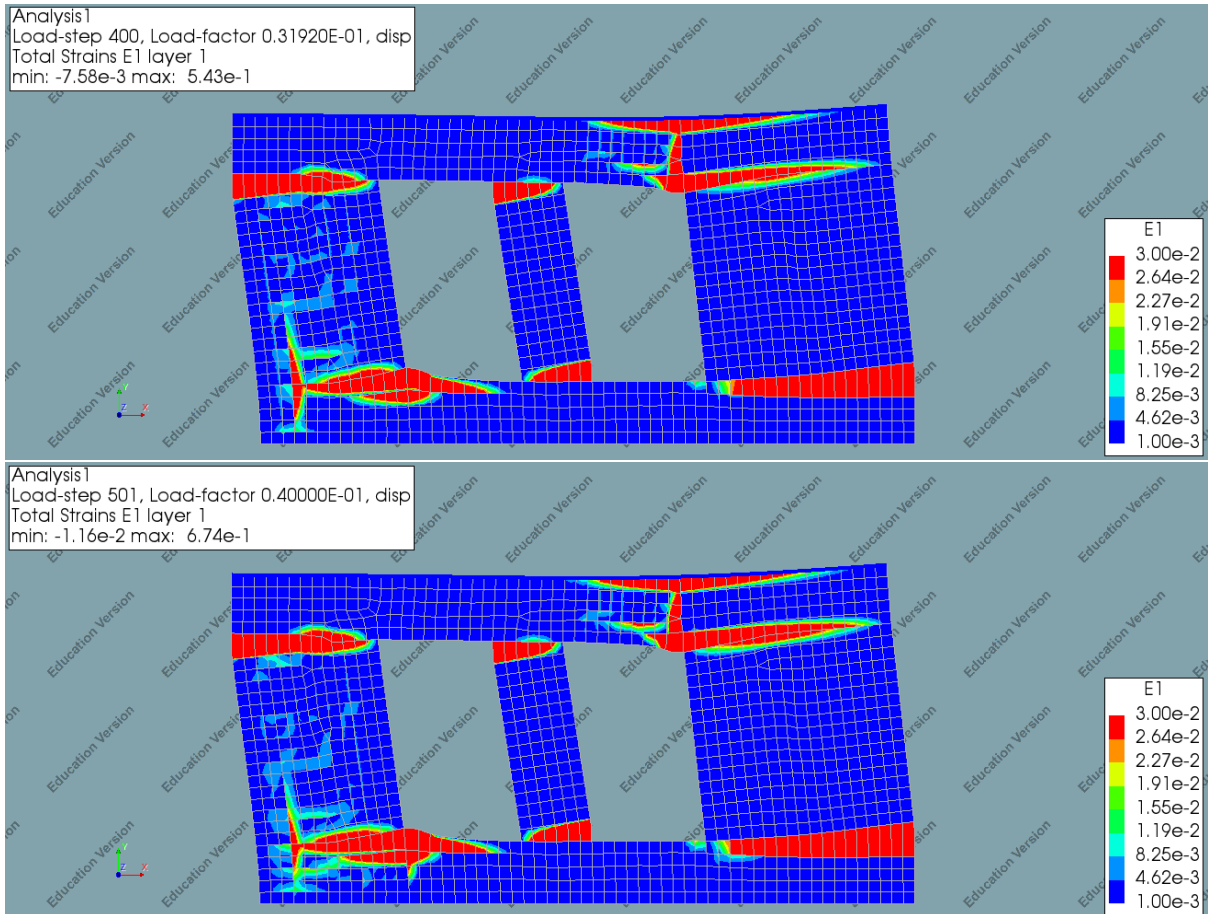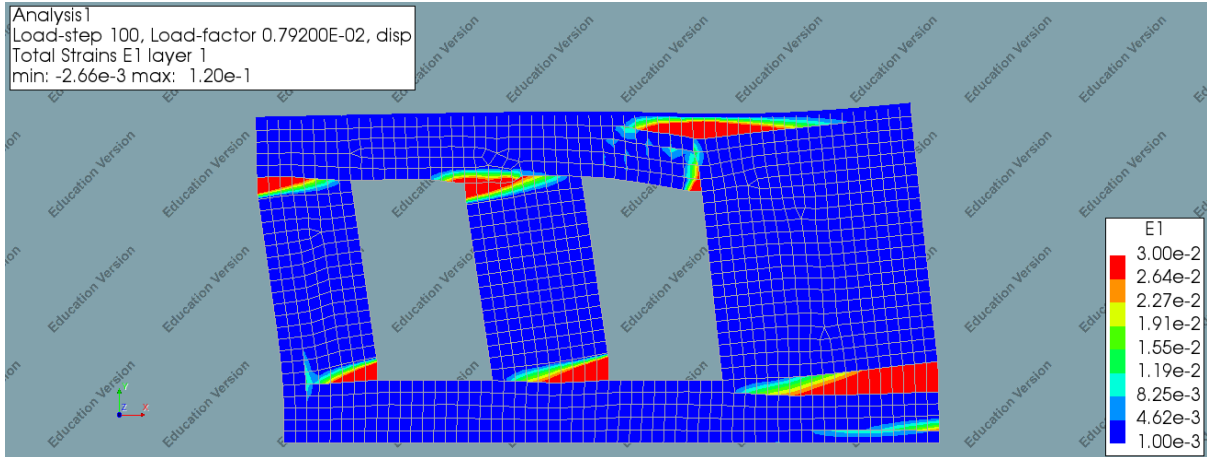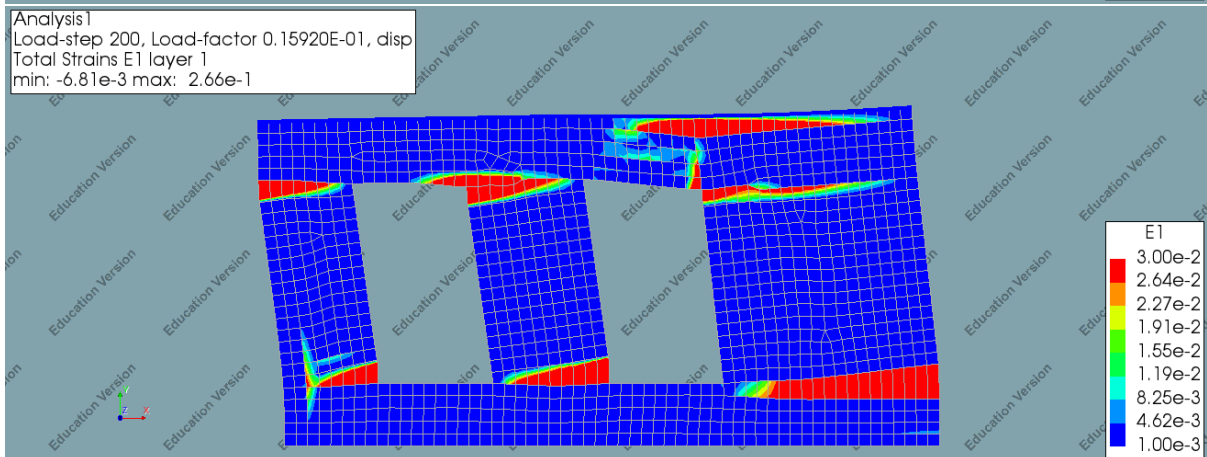1.19e-2
8.25e-3
4.62e-3
1.00e-3
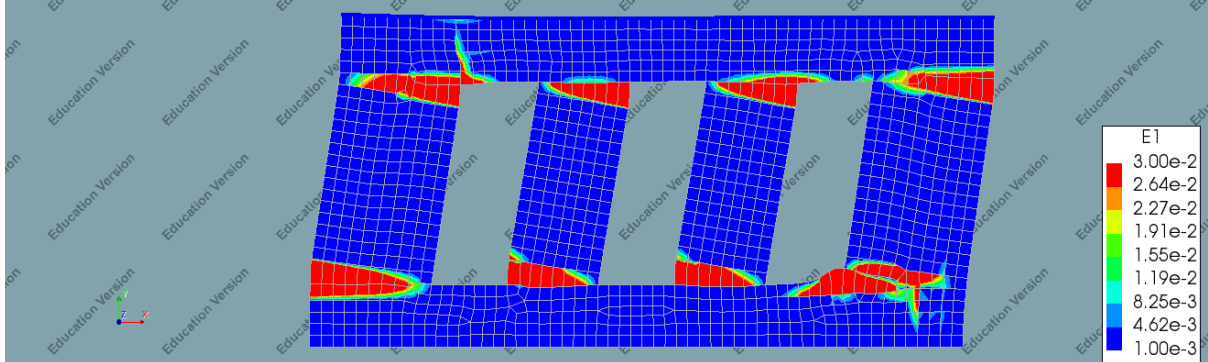
Figure 74: Principal strain plot Wall 6 for steps 100, 200, 300, 400 and 501

Wall 7

Analysis1
Load-step 100, Load-factor 0.79200E-02, disp
Total Strains E1 layer 1
min: -4.90e-3 max: 1.02e-1

E1

3.00e-2
2.64e-2
2.27e-2
1.91e-2
1.55e-2
1.19e-2
8.25e-3
4.62e-3
1.00e-3

Analysis1
Load-step 200, Load-factor 0.15920E-01, disp
Total Strains E1 layer 1
min: -6.80e-3 max: 2.13e-1

E1

3.00e-2
2.64e-2
2.27e-2
1.91e-2
1.55e-2
1.19e-2
8.25e-3
4.62e-3
1.00e-3

Analysis1
Load-step 300, Load-factor 0.23920E-01, disp
Total Strains E1 layer 1
min: -1.56e-3 max: 3.34e-1

E1

3.00e-2
2.64e-2
2.27e-2
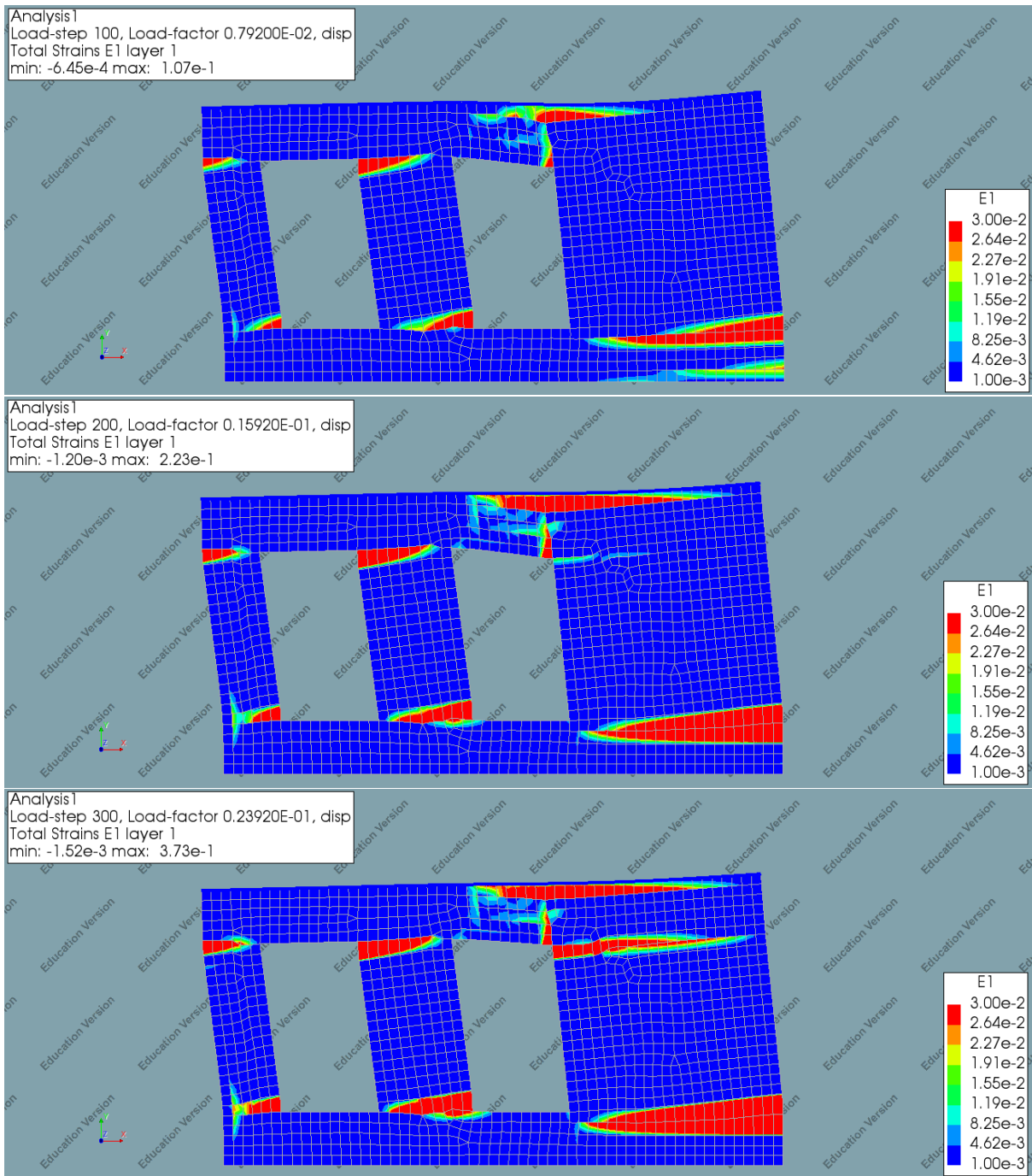1.91e-2
1.55e-2
1.19e-2
8.25e-3
4.62e-3
1.00e-3

Figure 75: Principal strain plot Wall 7 for steps 100, 200, 300, 400 and 501

Wall 8
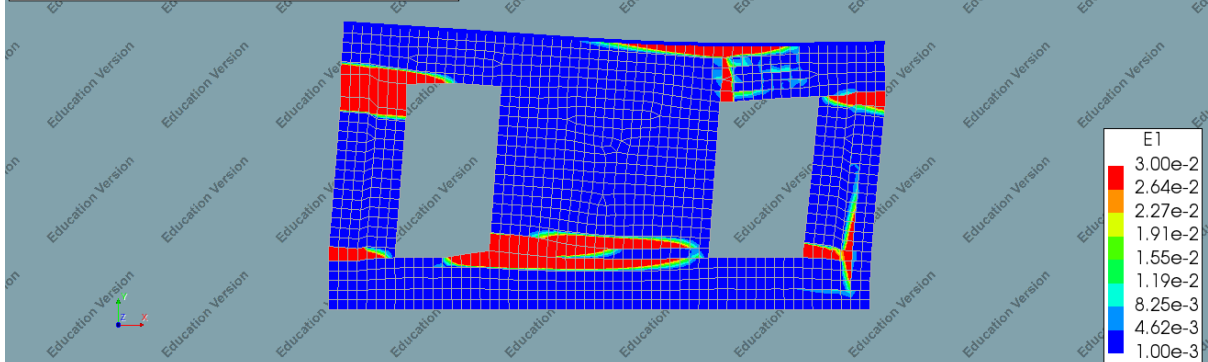
Figure 76: Principal strain plot Wall 8 for steps 100, 200, 300, 400 and 501

Wall 9

Analysis1
Load-step 100, Load-factor 0.79200E-02, disp
Total Strains E1 layer 1
min: -2.86e-3 max: 1.75e-1

E1
3.00e-2
2.64e-2
2.27e-2
1.91e-2
1.55e-2
1.19e-2
8.25e-3
4.62e-3
1.00e-3

Analysis1
Load-step 200, Load-factor 0.15920E-01, disp
Total Strains E1 layer 1
min: -5.09e-3 max: 3.50e-1

E1
3.00e-2
2.64e-2
2.27e-2
1.91e-2
1.55e-2
1.19e-2
8.25e-3
4.62e-3
1.00e-3

Analysis1
Load-step 300, Load-factor 0.23920E-01, disp
Total Strains E1 layer 1
min: -5.97e-3 max: 4.12e-1

E1
3.00e-2
2.64e-2
2.27e-2
1.91e-2
1.55e-2
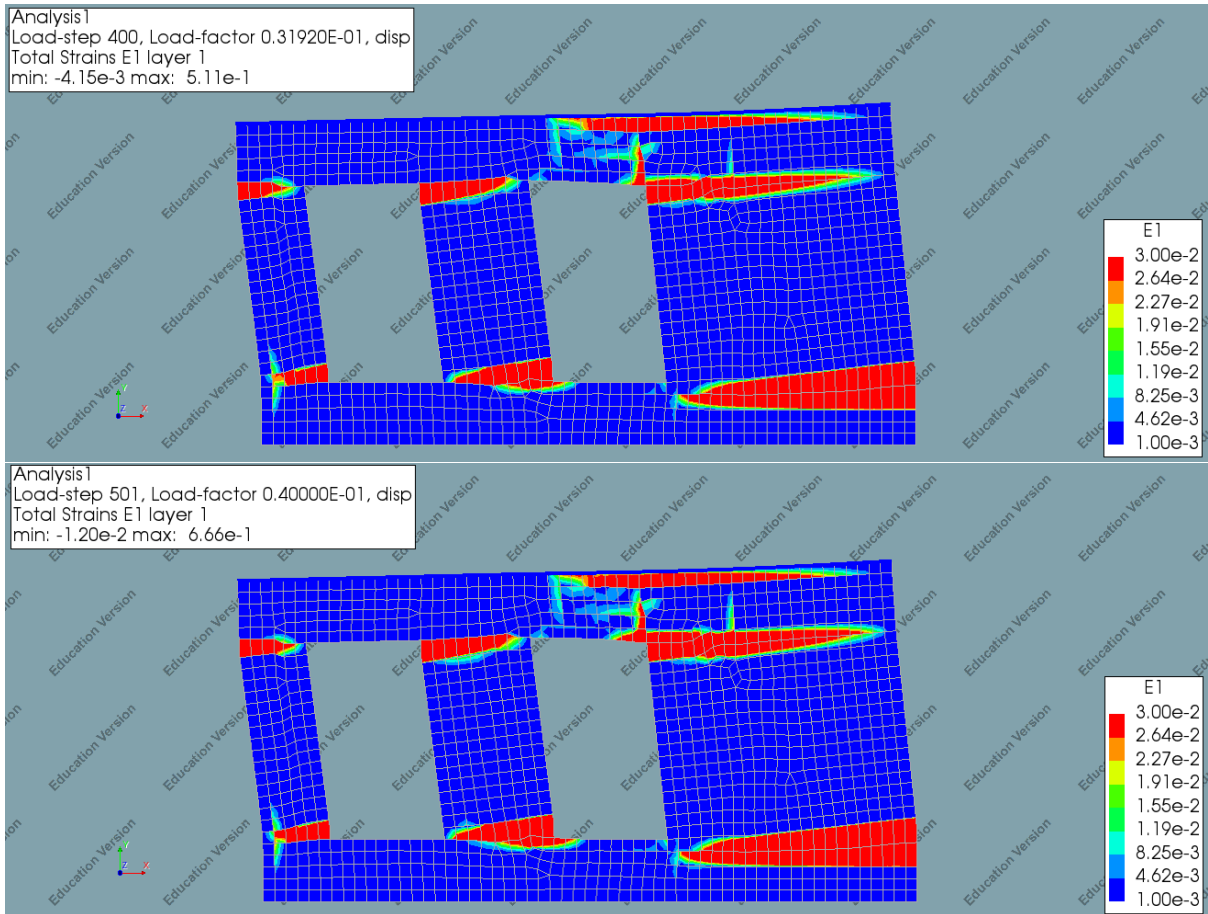1.19e-2
8.25e-3
4.62e-3
1.00e-3

Figure 77: Principal strain plot Wall 9 for steps 100, 200, 300, 400 and 501

Wall 10

Analysis1
Load-step 100, Load-factor 0.79200E-02, disp
Total Strains E1 layer 1
min: -2.66e-3 max: 1.20e-1

E1
3.00e-2
2.64e-2
2.27e-2
1.91e-2
1.55e-2
1.19e-2
8.25e-3
4.62e-3
1.00e-3

Analysis1
Load-step 200, Load-factor 0.15920E-01, disp
Total Strains E1 layer 1
min: -6.81e-3 max: 2.66e-1

E1
3.00e-2
2.64e-2
2.27e-2
1.91e-2
1.55e-2
1.19e-2
8.25e-3
4.62e-3
1.00e-3

Analysis1
Load-step 300, Load-factor 0.23920E-01, disp
Total Strains E1 layer 1
min: -1.07e-2 max: 4.24e-1

E1
3.00e-2
2.64e-2
2.27e-2
1.91e-2
1.55e-2
1.19e-2
8.25e-3
4.62e-3
1.00e-3
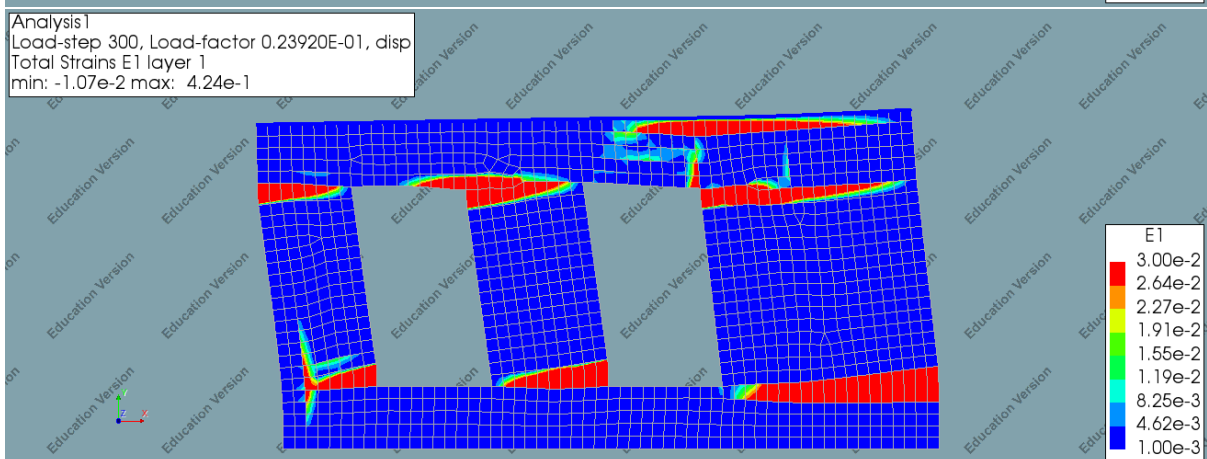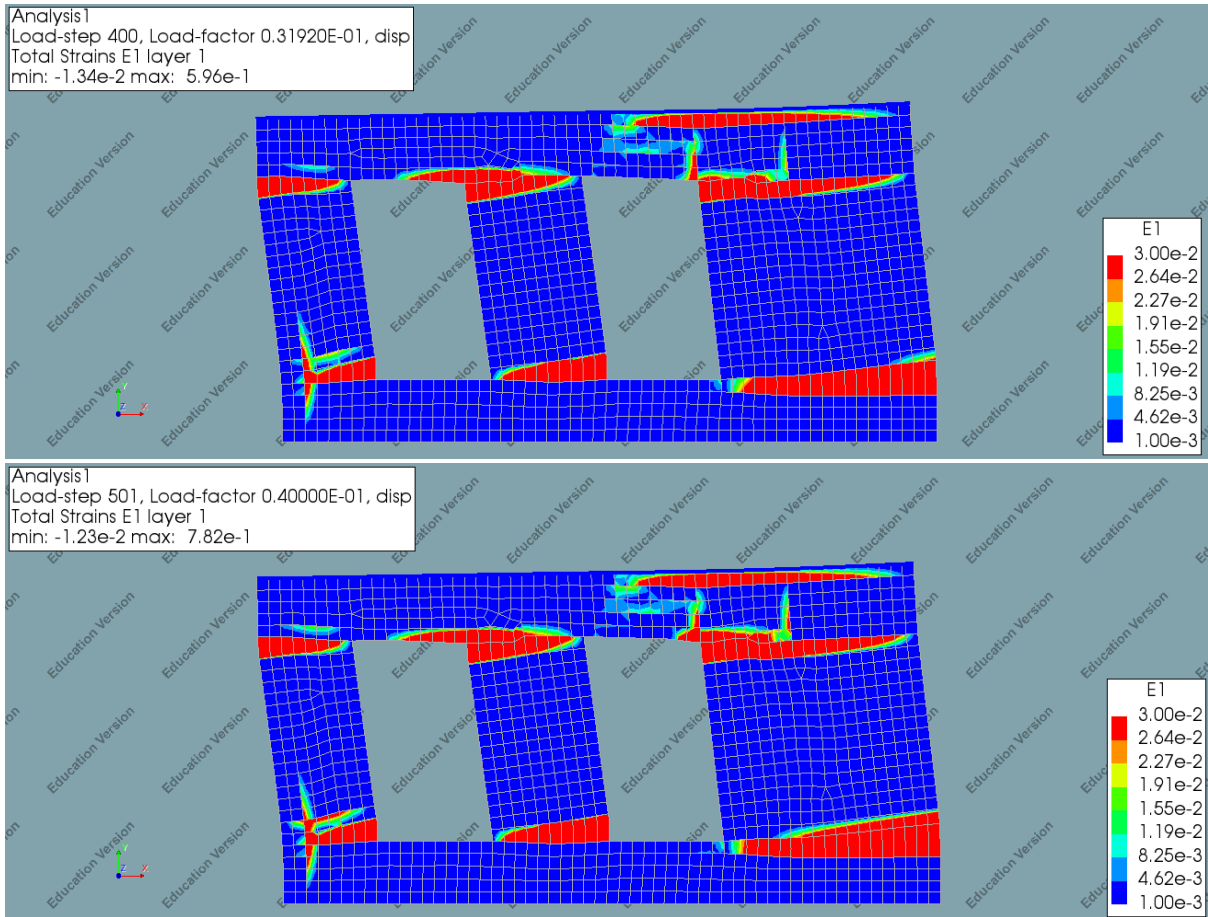
Figure 78: Principal strain plot Wall 10 for steps 100, 200, 300, 400 and 501

Wall 11

Analysis1
Load-step 100, Load-factor 0.79200E-02, disp
Total Strains E1 layer 1
min: -6.45e-4 max: 1.07e-1

E1
3.00e-2
2.64e-2
2.27e-2
1.91e-2
1.55e-2
1.19e-2
8.25e-3
4.62e-3
1.00e-3

Analysis1
Load-step 200, Load-factor 0.15920E-01, disp
Total Strains E1 layer 1
min: -1.20e-3 max: 2.23e-1

E1
3.00e-2
2.64e-2
2.27e-2
1.91e-2
1.55e-2
1.19e-2
8.25e-3
4.62e-3
1.00e-3

Analysis1
Load-step 300, Load-factor 0.23920E-01, disp
Total Strains E1 layer 1
min: -1.52e-3 max: 3.73e-1

E1
3.00e-2
2.64e-2
2.27e-2
1.91e-2
1.55e-2
1.19e-2
8.25e-3
4.62e-3
1.00e-3

Figure 79: Principal strain plot Wall 11 for steps 100, 200, 300, 400 and 501

Wall 12

Analysis1
Load-step 100, Load-factor 0.79200E-02, disp
Total Strains E1 layer 1
min: -2.38e-3 max: 1.01e-1

E1
3.00e-2
2.64e-2
2.27e-2
1.91e-2
1.55e-2
1.19e-2
8.25e-3
4.62e-3
1.00e-3
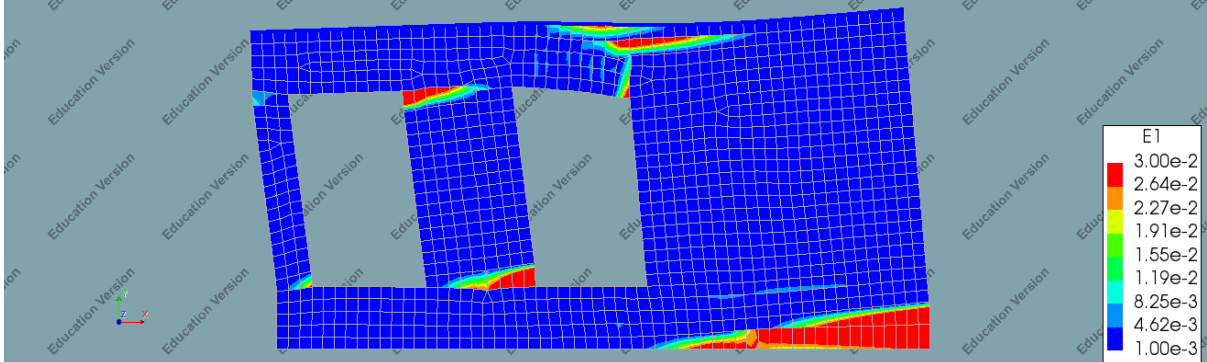
Analysis1
Load-step 200, Load-factor 0.15920E-01, disp
Total Strains E1 layer 1
min: -2.79e-3 max: 2.21e-1

E1
3.00e-2
2.64e-2
2.27e-2
1.91e-2
1.55e-2
1.19e-2
8.25e-3
4.62e-3
1.00e-3
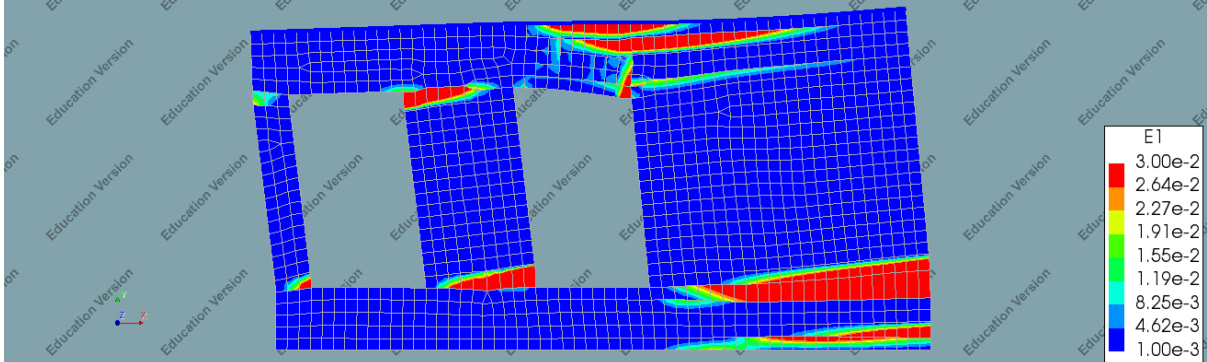
Analysis1
Load-step 300, Load-factor 0.23920E-01, disp
Total Strains E1 layer 1
min: -5.70e-3 max: 3.48e-1

E1
3.00e-2
2.64e-2
2.27e-2
1.91e-2
1.55e-2
1.19e-2
8.25e-3
4.62e-3
1.00e-3
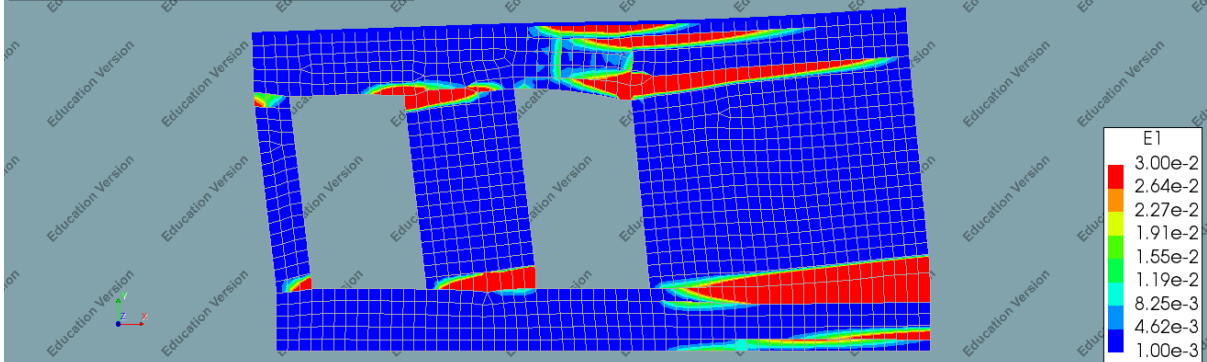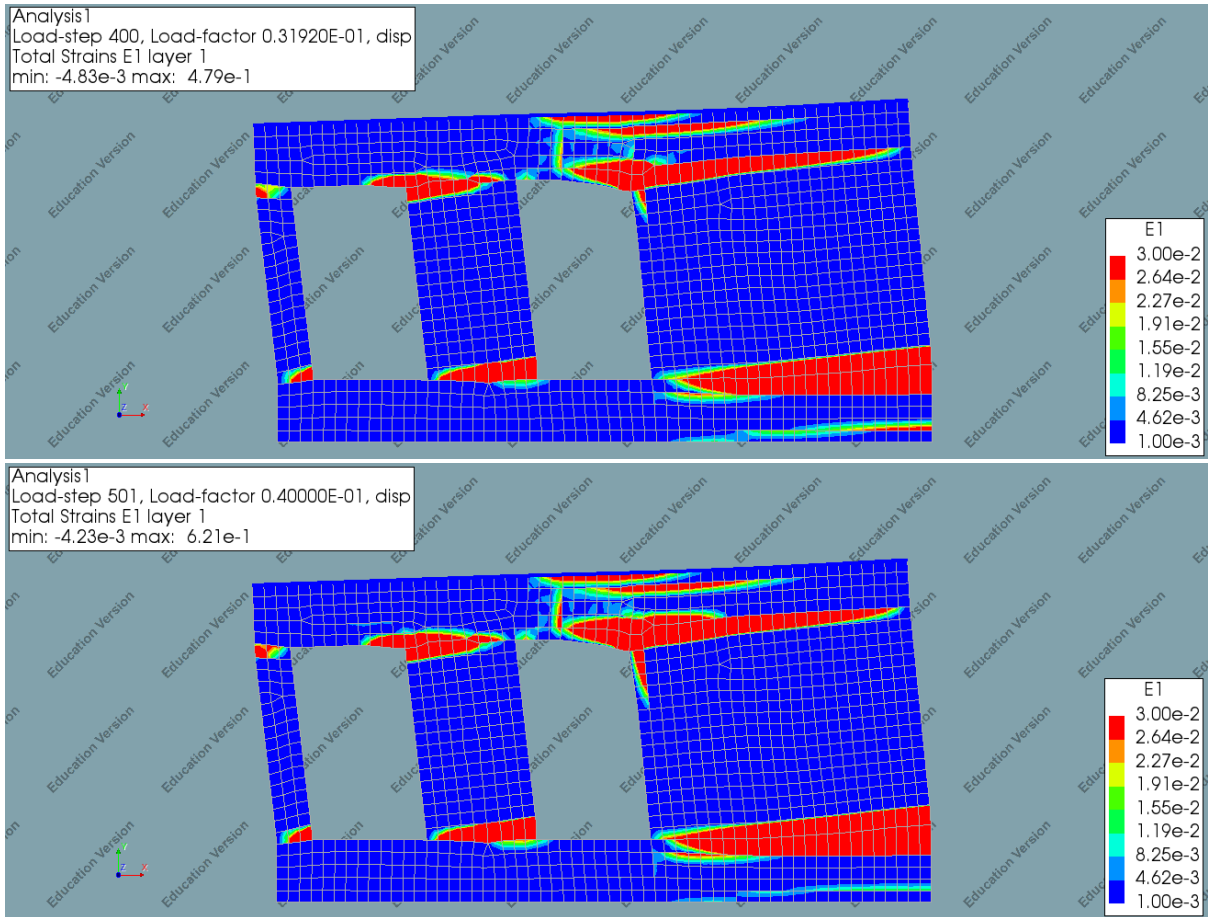
Figure 80: Principal strain plot Wall 12 for steps 100, 200, 300, 400 and 501

C. Appendix C: Total Strain Crack model results

In the figures below the principal strain plots are shown at 4 different stages during loading for the Total Strain Crack model results of wall 2 and 8.
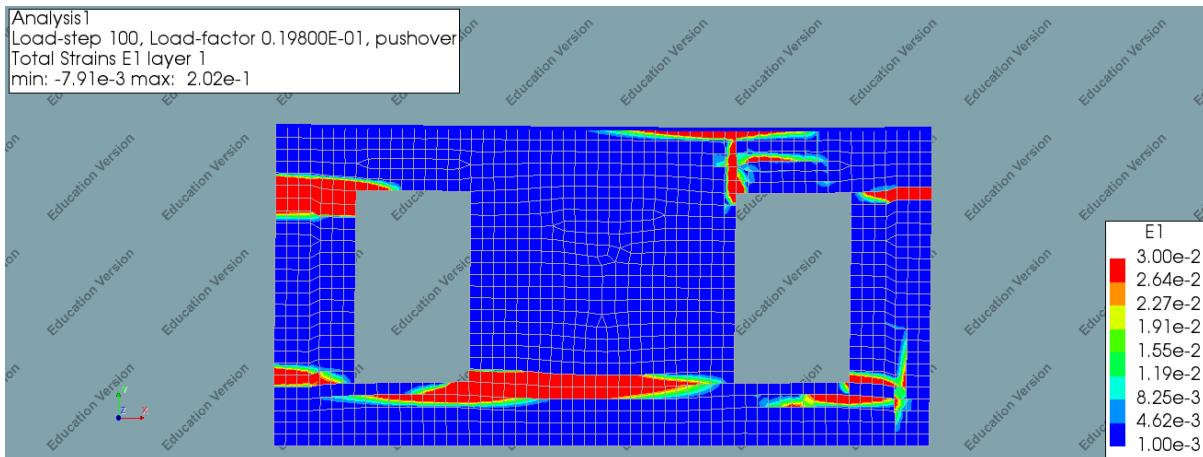
Wall 2
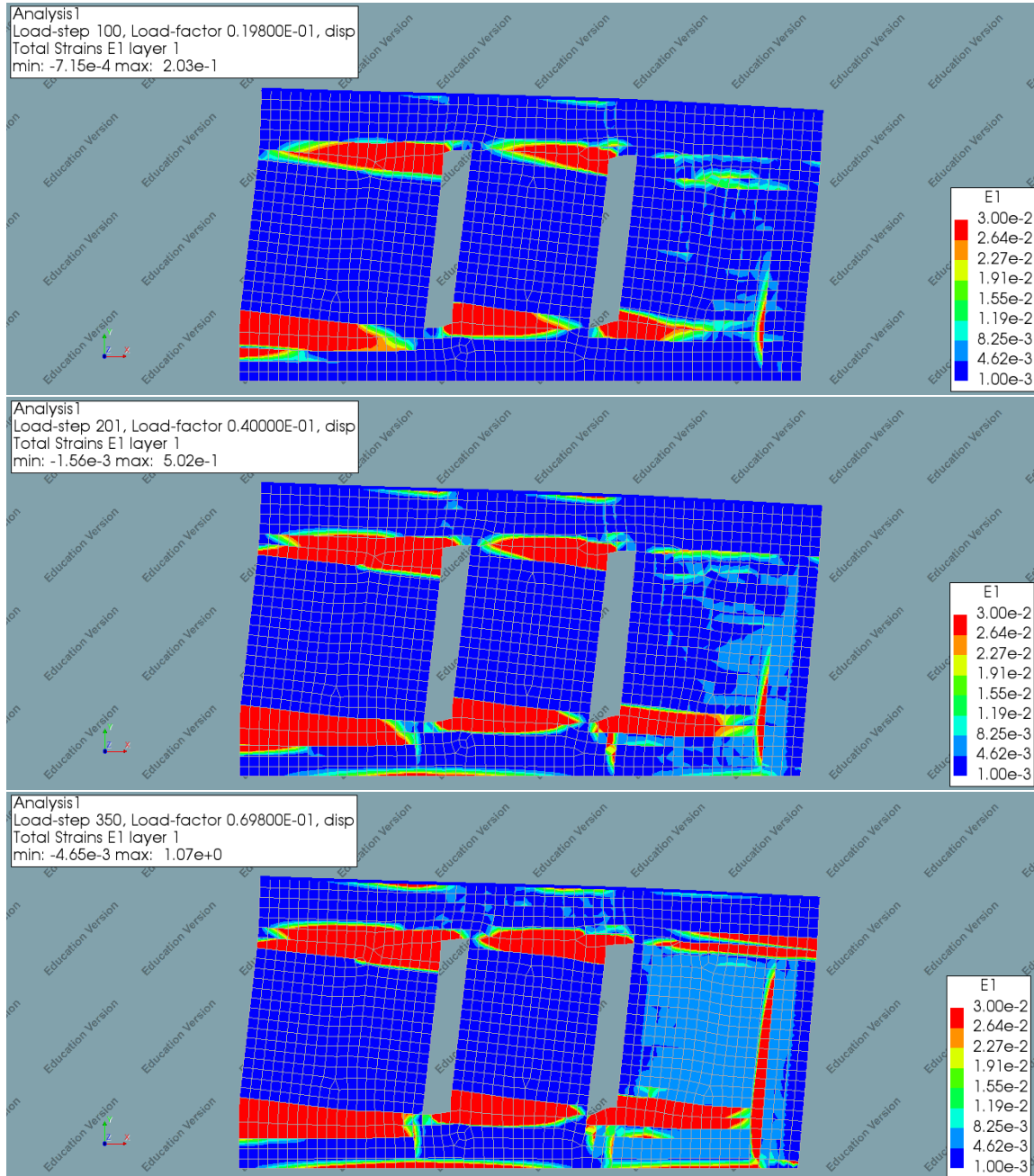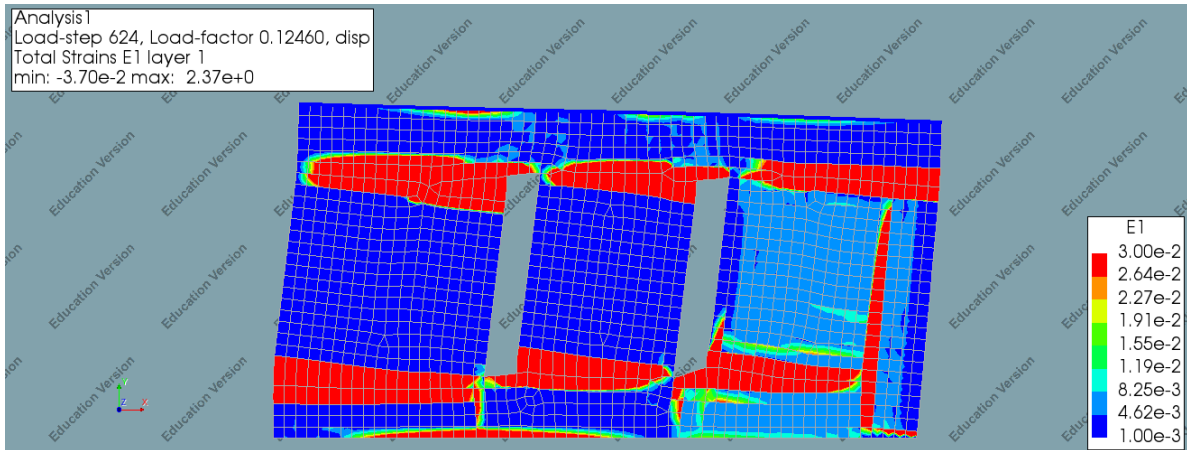
Figure 81: Principal strain plot Wall 2 for steps 100, 201, 350 and 624
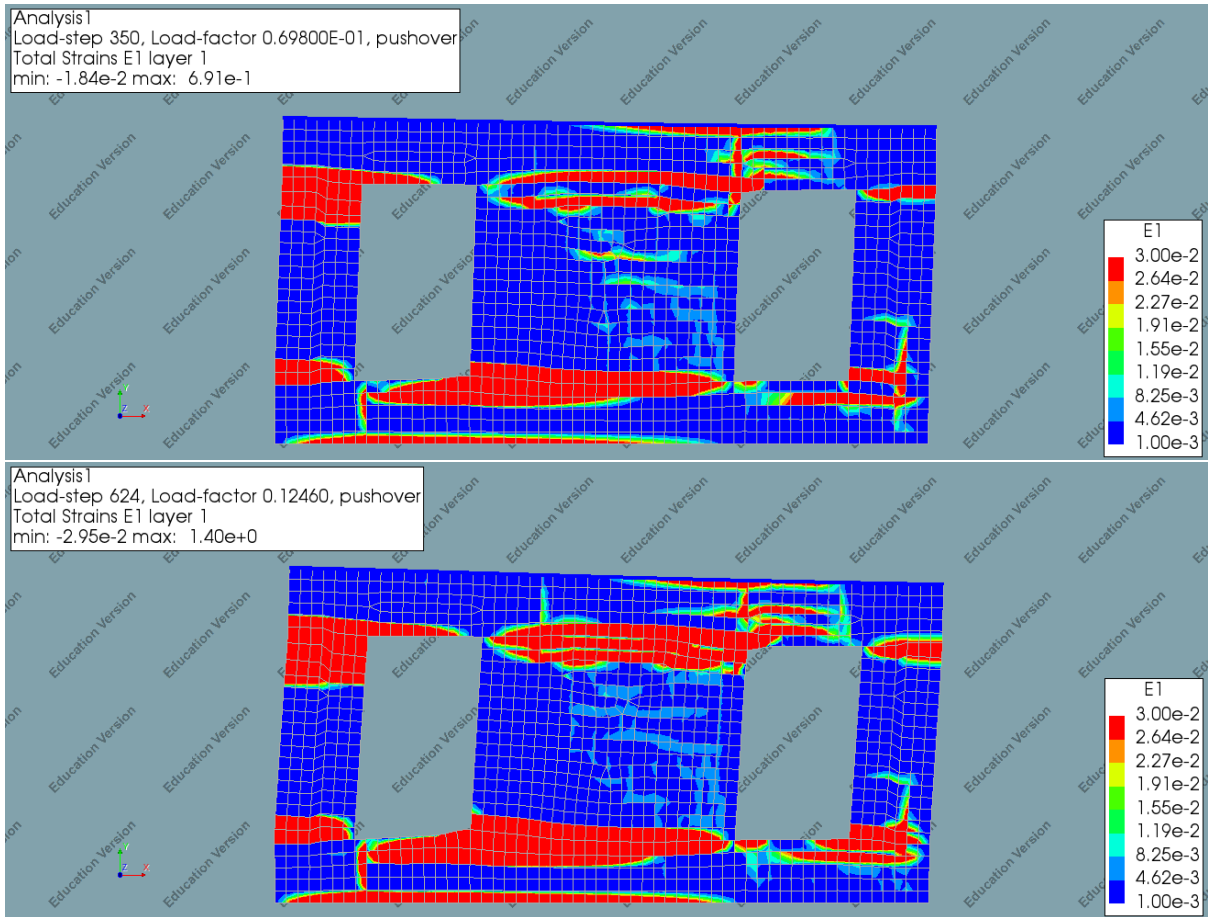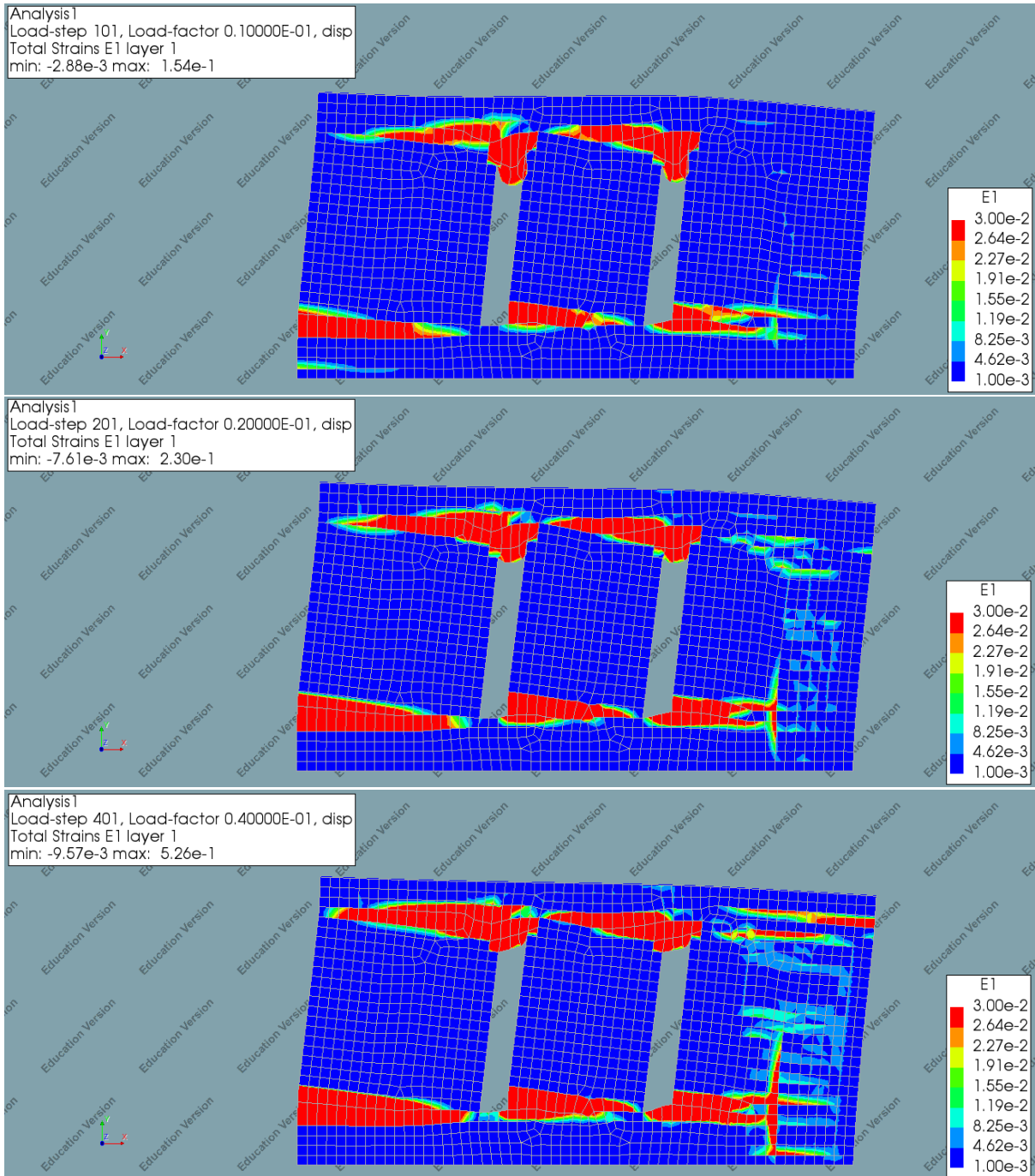
Wall 8
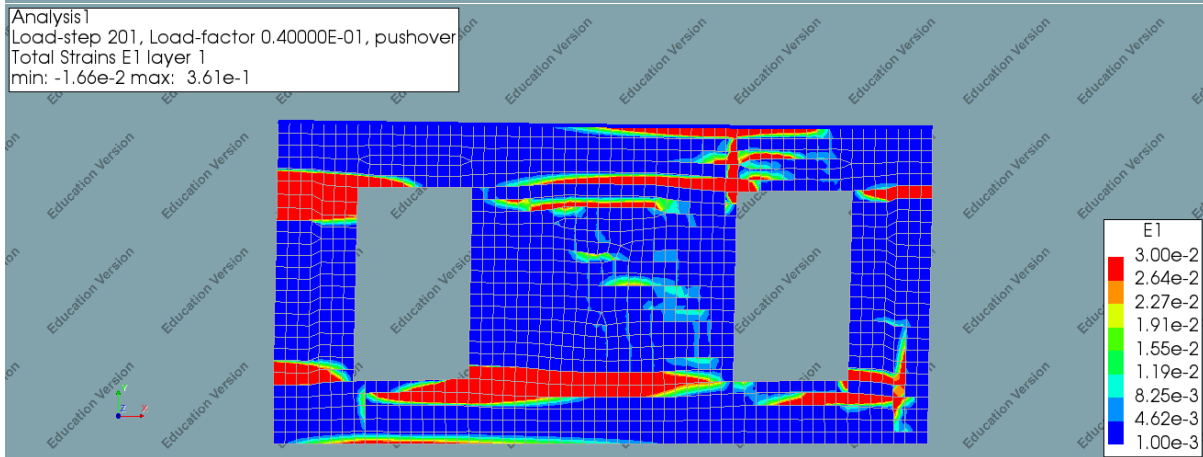
Figure 82: Principal strain plot Wall 8 for steps 100, 201, 350 and 624

D. Appendix D: Results walls with lintels

In the figures below, the strain plots are shown for the wall configurations modelled with lintels for wall 2 and 8 at five different stages.
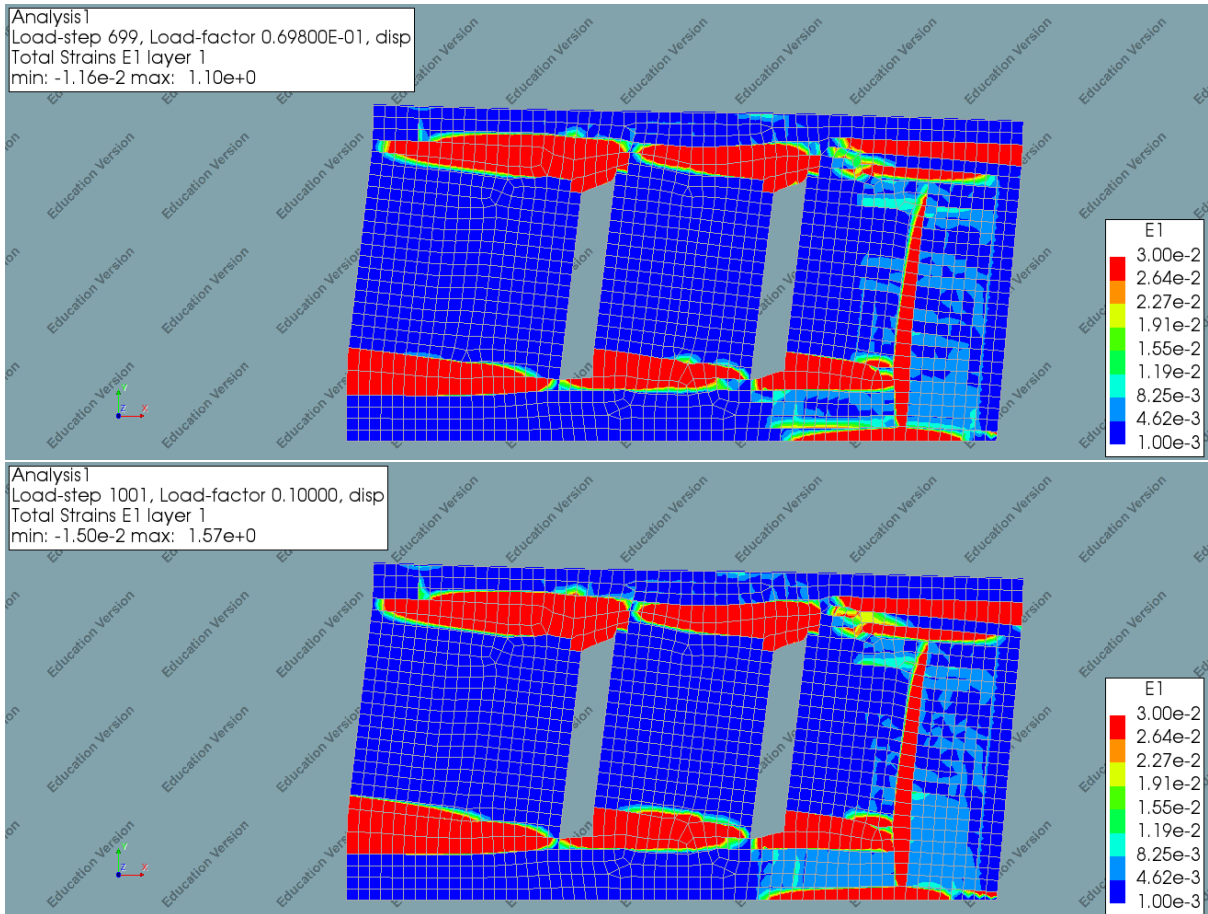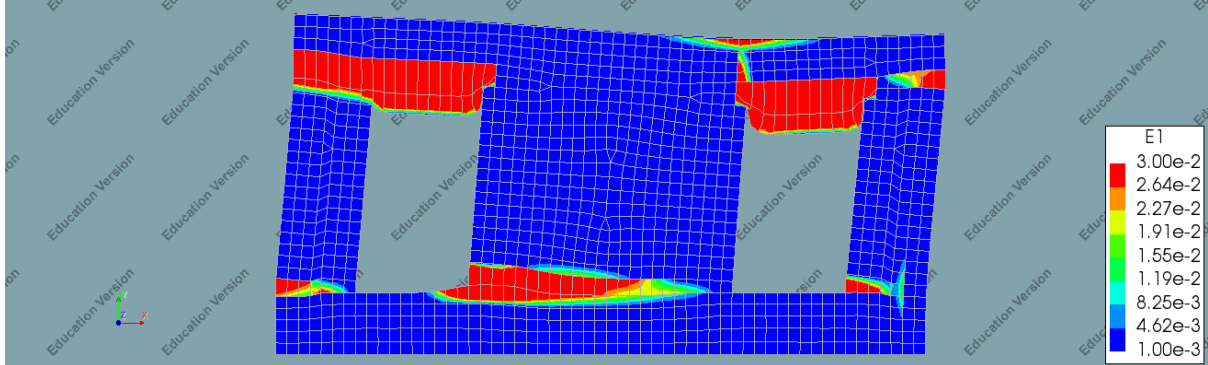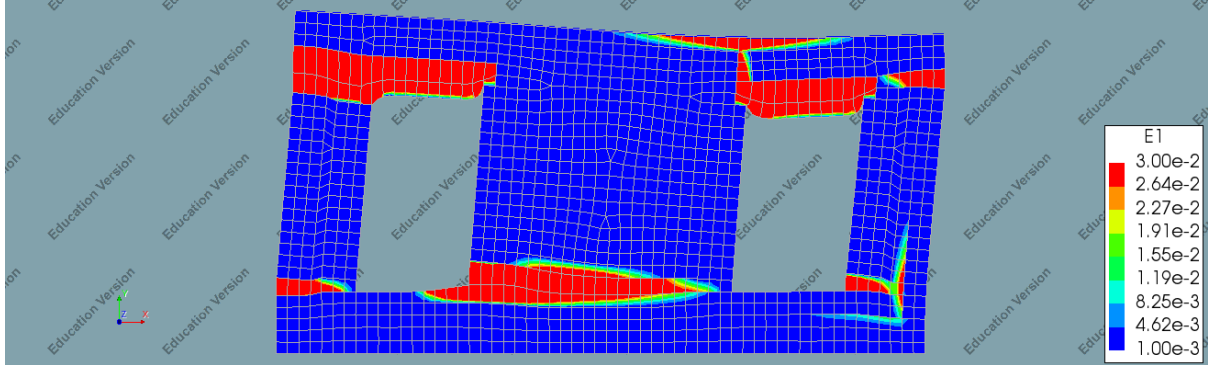
Wall 2

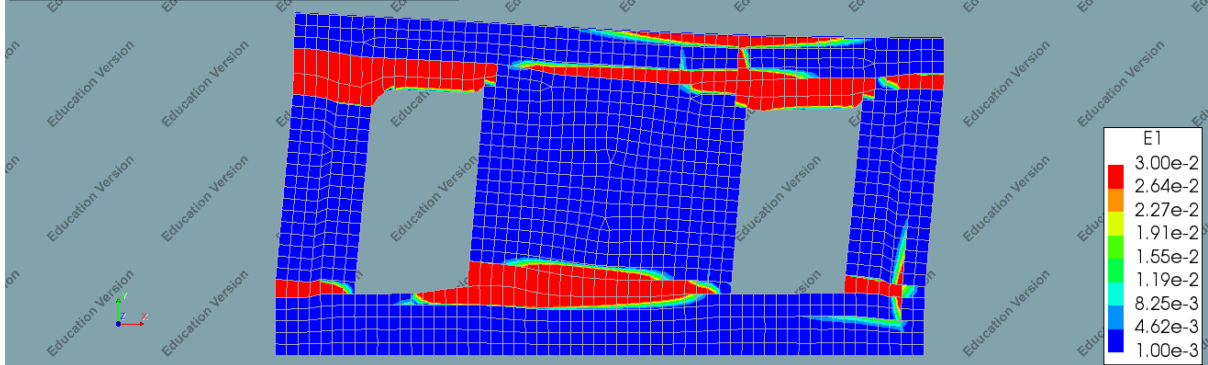*Figure 83: Principal strain plot Wall 2 for steps 101, 201, 401, 699 and 1001*

Wall 8

Analysis1
Load-step 101, Load-factor 0.10000E-01, pushover
Total Strains E1 layer 1
min: -3.69e-3 max: 2.08e-1

E1
3.00e-2
2.64e-2
2.27e-2
1.91e-2
1.55e-2
1.19e-2
8.25e-3
4.62e-3
1.00e-3

Analysis1
Load-step 201, Load-factor 0.20000E-01, pushover
Total Strains E1 layer 1
min: -7.40e-3 max: 3.93e-1

E1
3.00e-2
2.64e-2
2.27e-2
1.91e-2
1.55e-2
1.19e-2
8.25e-3
4.62e-3
1.00e-3

Analysis1
Load-step 401, Load-factor 0.40000E-01, pushover
Total Strains E1 layer 1
min: -2.48e-2 max: 9.43e-1

E1
3.00e-2
2.64e-2
2.27e-2
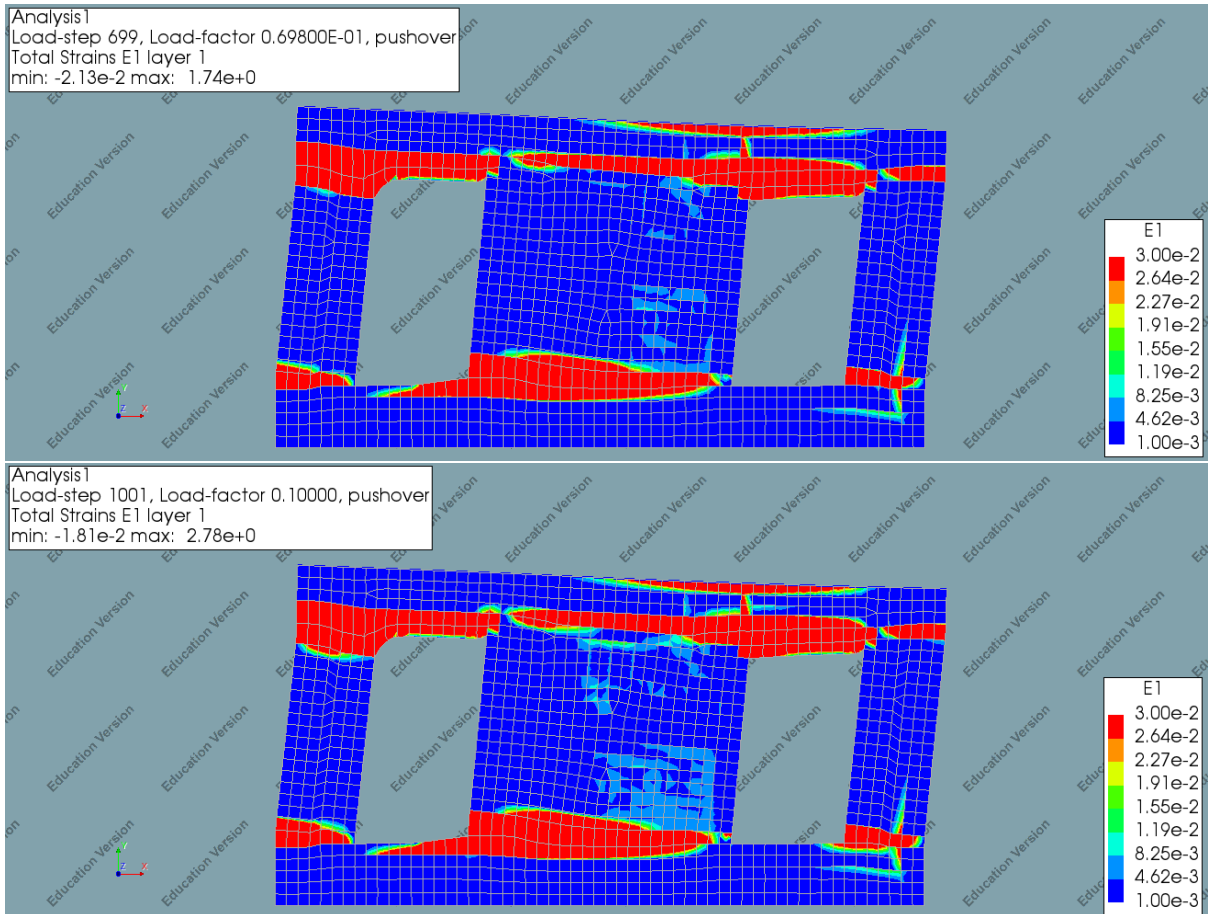1.91e-2
1.55e-2
1.19e-2
8.25e-3
4.62e-3
1.00e-3

Figure 84: Principal strain plot Wall 8 for steps 101, 201, 401, 699 and 1001